AN OPEN SOURCE SOFTWARE FOR PROTON TREATMENT PLANNING

POLITECNICO DI MILANO

PhD Program in Bioengineering

This dissertation is submitted for the degree of Doctor of Philosophy

December 2015

Tutor: Prof. Maria Laura COSTANTINO
Supervisors: Prof. Guido BARONI, Prof. Gregory C. SHARP
Coordinator: Prof. Andrea ALIVERTI

PhD Thesis by:
Maxime DESPLANQUES
10429341
XXVIII cycle

To my parents,

without whom none of this would be possible.

ABSTRACT

INTRODUCTION: This report describes in three sections the complete method for the creation of an open-source, multi-platform Treatment Planning System (TPS) dedicated to proton beam lines.

The first part outlines the implementation of a proton Dose Calculation Engine (DCE) based on pencil beam algorithms in Plastimatch, an open-source software for medical image computation. The DCE was decomposed into two types of algorithms: the model of the beam line elements and the dose summation algorithms in the input CT-images. An accurate analysis of the proton pencil beam deformation due to beam line elements was performed. Three pencil beam dose summation algorithms were developed, in addition to the reference well-known Hong's algorithm, and compared with dose distributions computed by Monte Carlo simulations.

The second part illustrates how the proton pencil beam model was upgraded with respect to Hong's reference algorithms, providing a better description of the lateral scattering of protons in both the range compensator and in the patient heterogeneities.

The last part describes the creation of a user-friendly interface, implemented in the open-source software for medical image computation and visualization 3D Slicer. The interface, connected to the dose DCE developed in Plastimatch, simulates a commercial TPS: it allows the setting of the parameters required for both the beam line characterization and the definition of a specific treatment plan. Moreover, the interface also provides a visualization of the output dose volume, associated to the treatment plan, overlapped on the input CT-images.

METHODS: The entire beam line model implemented in Plastimatch was based on the Hong's method, known as the reference method for proton pencil beam dose calculations and dedicated to passively scattered beam line. The approach was validated by Monte Carlo simulations and compared to the three alternative dose summation models developed in this project: the Ray Tracer (RT), the Cartesian Geometry dose Summation algorithm (CGS) and the Divergent Geometry dose Summation algorithm (DGS).

In particular conditions, such as heterogeneous media, the reference algorithm is known to compute inaccurately the proton beamlet spread. We proposed to upgrade it in two ways: at first, by building a new model that described the lateral scattering of proton pencil beamlets in range compensators. The study evaluated multiple analytical models of beamlet spreads that are customized for a PMMA range compensator. Four different models were chosen and their accuracies were tested by Monte Carlo measurements in the particle therapy energy range. At a later stage, a differential method accounting for the patient heterogeneities was developed with the help of the proton scattering power theory and implemented as an alternative algorithm in Plastimatch. The algorithm was built in order to consider both the composition and the position of any scattering material crossed by the pencil beam axis, while the Hong's reference algorithm is based only on a water pencil beam scaled by the water equivalent depth in the medium.

Finally, the TPS developed in this project proposed to automatically conform the dose distribution around a target volume. To reach this objective, three algorithms were achieved: a collimator shaper based on the projection of the target volume in the beam frame, a range compensator creator considering the lack of material upward the target volume, and a Spread Out Bragg Peak (SOBP) designer.

RESULTS AND DISCUSSION: The four dose summation algorithms were tested in broad beam conditions. The CGS, DGS and HGS were in good agreement with Monte Carlo simulations (2.5%-2.5 mm gamma-index scores > 95%). Instead, the RT algorithm, not considering any lateral scattering, was clearly refuted.

The Hong's algorithm describing the beamlet spread in the patient was assessed to be accurate only in homogeneous water equivalent media. In heterogeneous phantoms involving air gaps, the Hong's model led to 60% errors on the Full Width at Half Maximum (FWHM) of the beamlet lateral spread when compared to Monte Carlo simulations. Once the differential method based on the scattering power theory was applied in the same conditions, this error was reduced to 6%. Improvements were also found in cortical bone-water heterogeneities, reducing the error on the FWHM from 30% with the Hong's approach to 2.5% with the differential approach.

Regarding the PMMA-range compensator analytical models, the most significant input parameters proved to be the distance from the effective origin of the scattering inside the range compensator, the particle energy and the range compensator thickness. The study showed that two models considering the effective origin of scattering were more accurate than simpler models that did not contemplate such factor, and they provided estimations of beamlet spread induced by PMMA range compensators in the order of 0.2 % ± 3.1 % (mean ± standard deviation, compared to MC simulations) when the reference Hong's model provided discrepancies in the order of -6.7% ± 7.7%.

Ultimately, the report proposes an overview of the complete interface including the presentation of the modules for the beam line characterization and the treatment plan definition. Two different treatment plans are presented as examples, which have been successfully created from the SlicerRt interface connected to the Plastimatch DCE. These two examples were computed on real patient images (pelvis and brain localizations) and validated the whole beam line model (including the collimator shaper, the range compensator creator and the SOBP designer) as the dose distribution associated to these treatment plans conformed accurately and homogeneously the target whole volume.

CONCLUSION: The study showed that a basic TPS dedicated to passively scattered proton beam line could be contrived with accuracy. The dosimetric study validated two new dose summations algorithms (CGS and DGS) in addition to the reference HGS algorithm, the CGS being slightly faster than the HGS. We also proposed a differential

approach describing the pencil beamlet spread with a higher accuracy than the reference method, especially in heterogeneous media. The Plastimatch DCE achieved acceptable accuracy (2.5%-2.5 mm gamma-index scores > 95%) in both homogeneous and heterogeneous phantoms in a satisfying computation time (<5 min) on a common laptop or computer.

A precise analytic model for computing the beamlet spread induced by a common PMMA range compensator was developed and implemented in the Plastimatch DCE. These different improvements in the pencil beam definition allowed to create a complete basic TPS, calling the Plastimatch DCE, which was demonstrated to be more accurate than the reference Hong's method.

We hope that the open-source TPS developed during this PhD project will contribute to a better understanding and estimation of the delivered dose in particle therapy, especially for pencil beam dose calculation methods, and will help the research groups that couldn't afford a commercial TPS.

ACKNOWLEDGEMENTS

I want to sincerely thank Guido Baroni for giving to me the opportunity to dedicate an entire PhD project on a topic that corresponded to my background. I will always be grateful to him for this PhD experience. He always provided everything to make me work in the best conditions during this project and also during the previous year.

For the physics part, I definitely owe everything to Greg(ory) Sharp. I couldn't explain how much I have learned during this PhD and during our regular conference calls. He has always been kind to me and each time I was down because I had not reached the expected results, his constant good mood and new ideas let me twice as motivated as I was before the meeting. He is the perfect example of a person that "irradiates" a positive energy to his collaborators.

Thanks to my more-than-perfect parents *Joël & Claudie*, which always encourage me from France, even if they don't understand anything about my work. I consider it as the most sincere support it could exist. It is thanks to them that I will be a doctor tomorrow, and I couldn't dedicate this PhD thesis to anybody else than them.

Thanks to my brother and his family.

Thanks to my Italian family that did everything to make me feel as well as possible here. And thanks to who encourages me from heaven.

Thanks to Barbara, Andrea, Giulia and Marco for their help.

Thanks to MGH people, Jan, George, Justin, Yang-Kyun, Cindy and Paolo. You did everything to make me feel at home in Boston.

Thanks to Beppe and Andrea for their help with Monte Carlo simulations.

Thanks for who supported me during the thesis writing.

Thanks to all my friends.

CONTENTS

LIST OF TABLES

LIST OF FIGURES

LIST OF APPENDICES

LIST OF ABBREVIATIONS AND ACRONYMS

BEV: Beam Eye View
CGS: Cartesian Geometry dose Summation
CT: Computed Tomography
DCE: Dose Computation Engine
DSPA: Differential Scattering Approach
DNA: DeoxyriboNucleic Acid
DRR: Digital Reconstructed Radiography
DGS: Divergent Geometry dose Summation
FWHM: Full Width at Half Maximum
HCL: Harvard Cyclotron Laboratory
HGS: Hong Geometry dose Summation
HHA: Highland/Hong Approximation
HU: Hounsfield Unit
LED: Lucite Equivalent Depth
LNT: Linear No Threshold model
MC: Monte Carlo
MCNPx: Monte Carlo N-Particle extended
MCS: Multiple Coulomb Scattering
NIST: National Institute of Standards and Technology
OAR: Organ At Risk
ODV: Output Dose Volume
$pSTPR_m$: proton STopping Power Ratio (of material m)
PBA: Pencil Beam Algorithm
PMMA: PolyMethyl MethAchrylate, Lucite
RBE: Relative Biologic Effectiveness
RC: Range Compensator
RDP: Reference Dose Point
RT: Ray Tracer
SDPBP: Standard Deviation of the Pencil Beam Profile
SOBP: Spread Out Bragg Peak
STP: Stopping Power
TPS: Treatment Planning System
WED: Water Equivalent Depth

1. INTRODUCTION

1.1. Background and significance

1.1.1. Cancer statistics and Oncology

In 2014, an analysis from the World Health organization [1] stated that every year cancer is responsible for the death of 8.2 million people and 14 million new cases are declared, representing the second leading cause of mortality after cardiovascular diseases. The number of new cases is expected to increase by 70% by 2035 [1], mainly due to environmental facts, consumption habits and early detection diagnosis.

A cancer, or tumor, is an abnormal growth or a proliferation of normal tissues that doesn’t provide any physiological function. This general definition is not exhaustive and includes special cases such as metastasis or leukemia. To date, mainly 4 methods are used, concomitantly or not, to treat cancers or to control their proliferation:

- Surgery removal of the tumor mass and ablation
- Radiotherapy
- Chemotherapy
- Immunotherapy

Unfortunately, even with these four different techniques, only half of all cancers are cured, surgery having the higher cure rate. About 45-50% of the cancer diseases are curatively or palliatively treated with radiations, especially by photons (>90%) and electrons (≈10-15%, sometimes concomitantly with photons) [2].

1.1.2. Radiotherapy

Radiotherapy covers different treatment strategies, each one taking advantage of one or more physical properties according to the therapeutic aim. The most widespread techniques are treatment strategies involving photon beams and electron beams, chosen for their relatively low cost and curative success, but others particles such as ions or neutrons are also available. All these techniques have the same aim: using the ionizing properties of radiation to locally damage and kill the tumor. For this reason, radiotherapy is often considered as a "surgery at depth" and used for deeply tumor locations unreachable by the scalpel of surgeons.

Any kind of tumor can be completely destroyed by radiotherapy, but unfortunately this also applies to the healthy cells contained in the surrounding tissues. This undesirable issue represents to date the limit of the radiotherapy techniques. For most of the radiotherapy treatments, the ideal extermination of the tumor is not practicable due to irreparable, collateral damages to the healthy surrounding tissues, and tumor control is in most of the cases a satisfying trade-off. In other words, the aim of radiotherapy is to take advantage of the dose range allowing the tumor control and avoiding at the same time the physiological complications on the healthy tissues (Figure 1-1). In 2002, Kraft stipulated that with a sufficient accuracy in the patient set up and the radiation delivery, and considering the actual techniques, most of the radiotherapy treatments can lead to at least control of the tumor site [3].

Figure 1-1

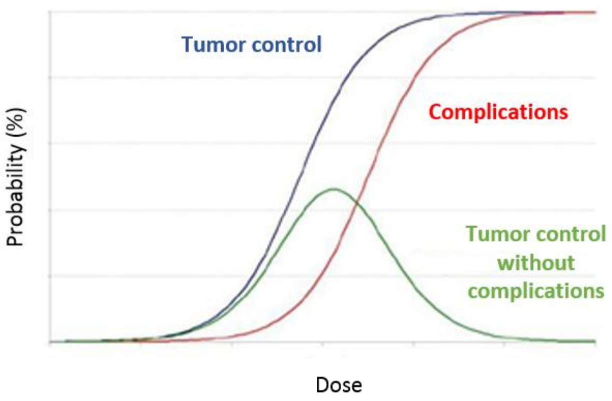

Representation of the tumor control (blue), the complication rate (red) and the tumor control without complication rates (green) according to the delivered dose to the target volume.

The main advantages of the radiotherapy, with respect to the other techniques, can be listed as follows:

- A low global cost
- No need for hospitalization or convalescence
- No pain during the treatment sessions, non-invasive technique

Most of radiotherapy treatments are delivered with photons. During the last two decades, the X-ray radiotherapy approach changed radically mainly due important improvements in two different fields:

- Imaging:
    - Computed Tomography (CT), Positron Emission Tomography (PET), Single Photon Emission Computed Tomography (SPECT) and Magnetic Resonance Imaging (MRI) allow henceforth a morphological and/or functional 3D reconstruction of the anatomic volumes. The breathing cycle can also be considered for 4D reconstructions.

  - In-room imaging during radiotherapy treatments (Cone Beam CT (CBCT), fluoroscopy…) improve the patient positioning for every treatment (Image Guided RadioTherapy (IGRT)).
- Inverse Planning: 3D dose distributions can be optimized and better conformed around to the target volume. This method creates higher dose gradients between the target volume and surrounding healthy tissues (including Organs At Risks (OAR)).

The combination of these advances in the radiotherapy field participated to the development of the following techniques: the 3D Conformational RadioTherapy (3DCRT), the Intensity Modulated RadioTherapy (IMRT), the Stereotactic Radiotherapy, the arc therapy and Tomotherapy. The relatively low cost of Linear Accelerators (Linacs), coupled with the efficiency of these techniques, can lead the radiotherapy centers to propose only these types of treatments. Nevertheless, for some particular cases like reirradiation or radioresistant tumors, common radiotherapy strategies are inefficient and other methods have to be considered.

Particle therapy is to date considered as a promising solution for these particular cases, and demonstrated excellent outcomes in the last decades, due to physical and radiobiological properties of protons and, more recently, heavy ions. This field of the radiotherapy is growing at very fast pace and represents the topic of this thesis.

1.1.3. Particle Therapy Generalities

1.1.3.1. Particle centers and patient statistics

During the last years, clinical evidences demonstrated significant advantages of the particle therapy over conventional radiotherapy, which implied a fast increase of the number of centers worldwide and a boost to technological developments. The idea of using accelerated particles to irradiate patients suffering from cancer was suggested by Wilson, a Harvard Cyclotron Laboratory (HCL) physicist, in 1946 [4]. The first trials were realized at the Berkeley Radiation Laboratory 8 years later. The first facility dedicated to regular proton therapy treatments was created in 1961 at HCL by the Massachusetts General Hospital, and treated more than 9,000 patients until its cessation in 2002.

Particle therapy is divided into 2 fields: protontherapy and hadrontherapy. The former deals with protons beams only, the latter with any type of ion beams (such as Carbon ion beams or Oxygen ion beams). The global number of patients treated by these two techniques, since their beginning in the 60’, is unequal (Figure 1-2): nearly 120,000 for proton therapy and around 15,000 only with ions [5], this difference mainly due to the fact that hadrontherapy started later (1975) and its higher costs leading to fewer dedicated centers. Due to the recent increase of particle therapy facilities construction, these numbers are expected to rise substantially during the next years [6].

Figure 1-2

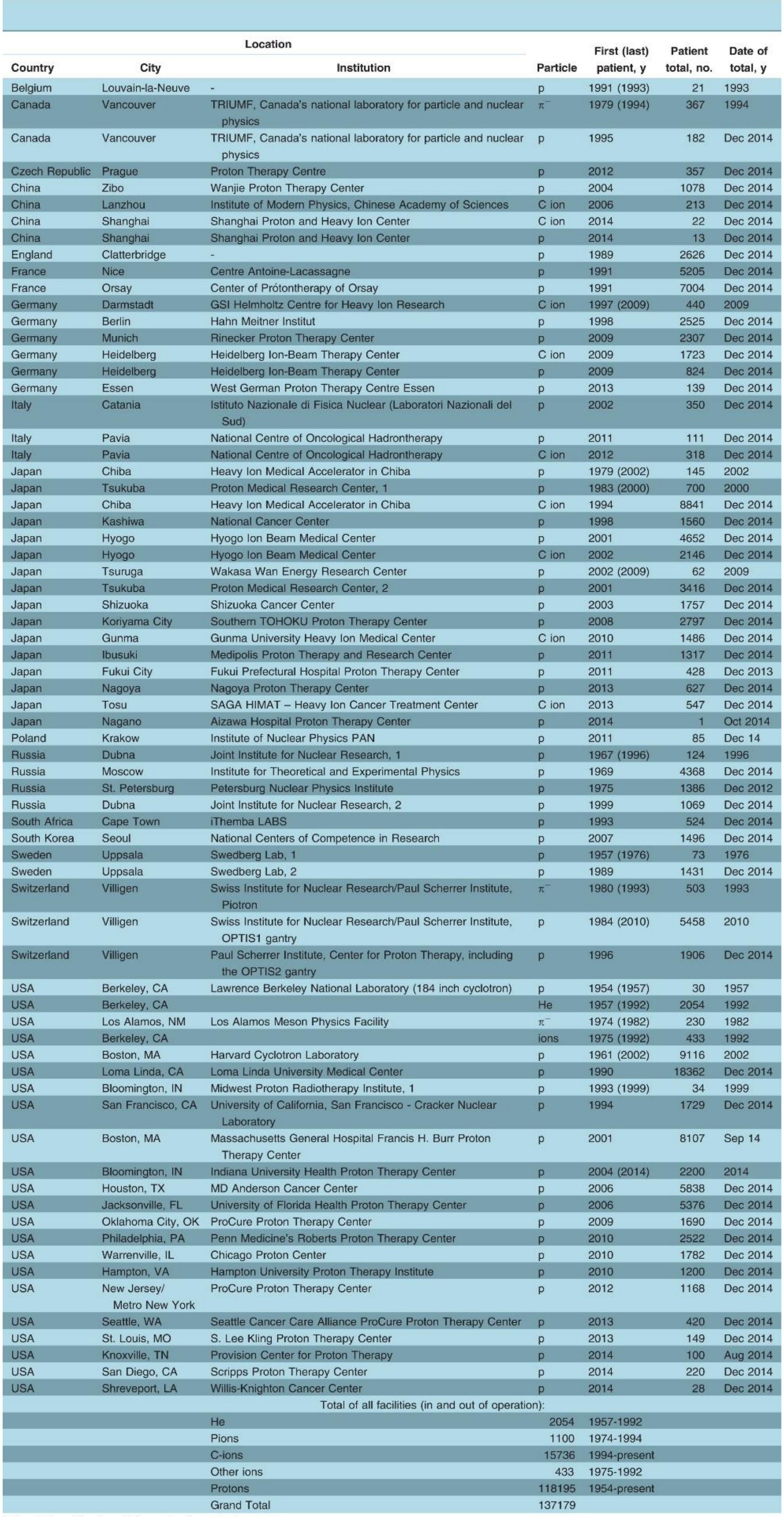

Location						
Country	City	Institution	Particle	First (last) patient, y	Patient total, no.	Date of total, y
Belgium	Louvain-la-Neuve	-	p	1991 (1993)	21	1993
Canada	Vancouver	TRIUMF, Canada's national laboratory for particle and nuclear physics	π^-	1979 (1994)	367	1994
Canada	Vancouver	TRIUMF, Canada's national laboratory for particle and nuclear physics	p	1995	182	Dec 2014
Czech Republic	Prague	Proton Therapy Centre	p	2012	357	Dec 2014
China	Zibo	Wanjie Proton Therapy Center	p	2004	1078	Dec 2014
China	Lanzhou	Institute of Modern Physics, Chinese Academy of Sciences	C ion	2006	213	Dec 2014
China	Shanghai	Shanghai Proton and Heavy Ion Center	C ion	2014	22	Dec 2014
China	Shanghai	Shanghai Proton and Heavy Ion Center	p	2014	13	Dec 2014
England	Clatterbridge	-	p	1989	2626	Dec 2014
France	Nice	Centre Antoine-Lacassagne	p	1991	5205	Dec 2014
France	Orsay	Center of Prótontherapy of Orsay	p	1991	7004	Dec 2014
Germany	Darmstadt	GSI Helmholtz Centre for Heavy Ion Research	C ion	1997 (2009)	440	2009
Germany	Berlin	Hahn Meitner Institut	p	1998	2525	Dec 2014
Germany	Munich	Rinecker Proton Therapy Center	p	2009	2307	Dec 2014
Germany	Heidelberg	Heidelberg Ion-Beam Therapy Center	C ion	2009	1723	Dec 2014
Germany	Heidelberg	Heidelberg Ion-Beam Therapy Center	p	2009	824	Dec 2014
Germany	Essen	West German Proton Therapy Centre Essen	p	2013	139	Dec 2014
Italy	Catania	Istituto Nazionale di Fisica Nuclear (Laboratori Nazionali del Sud)	p	2002	350	Dec 2014
Italy	Pavia	National Centre of Oncological Hadrontherapy	p	2011	111	Dec 2014
Italy	Pavia	National Centre of Oncological Hadrontherapy	C ion	2012	318	Dec 2014
Japan	Chiba	Heavy Ion Medical Accelerator in Chiba	p	1979 (2002)	145	2002
Japan	Tsukuba	Proton Medical Research Center, 1	p	1983 (2000)	700	2000
Japan	Chiba	Heavy Ion Medical Accelerator in Chiba	C ion	1994	8841	Dec 2014
Japan	Kashiwa	National Cancer Center	p	1998	1560	Dec 2014
Japan	Hyogo	Hyogo Ion Beam Medical Center	p	2001	4652	Dec 2014
Japan	Hyogo	Hyogo Ion Beam Medical Center	C ion	2002	2146	Dec 2014
Japan	Tsuruga	Wakasa Wan Energy Research Center	p	2002 (2009)	62	2009
Japan	Tsukuba	Proton Medical Research Center, 2	p	2001	3416	Dec 2014
Japan	Shizuoka	Shizuoka Cancer Center	p	2003	1757	Dec 2014
Japan	Koriyama City	Southern TOHOKU Proton Therapy Center	p	2008	2797	Dec 2014
Japan	Gunma	Gunma University Heavy Ion Medical Center	C ion	2010	1486	Dec 2014
Japan	Ibusuki	Medipolis Proton Therapy and Research Center	p	2011	1317	Dec 2014
Japan	Fukui City	Fukui Prefectural Hospital Proton Therapy Center	p	2011	428	Dec 2013
Japan	Nagoya	Nagoya Proton Therapy Center	p	2013	627	Dec 2014
Japan	Tosu	SAGA HIMAT – Heavy Ion Cancer Treatment Center	C ion	2013	547	Dec 2014
Japan	Nagano	Aizawa Hospital Proton Therapy Center	p	2014	1	Oct 2014
Poland	Krakow	Institute of Nuclear Physics PAN	p	2011	85	Dec 14
Russia	Dubna	Joint Institute for Nuclear Research, 1	p	1967 (1996)	124	1996
Russia	Moscow	Institute for Theoretical and Experimental Physics	p	1969	4368	Dec 2014
Russia	St. Petersburg	Petersburg Nuclear Physics Institute	p	1975	1386	Dec 2012
Russia	Dubna	Joint Institute for Nuclear Research, 2	p	1999	1069	Dec 2014
South Africa	Cape Town	iThemba LABS	p	1993	524	Dec 2014
South Korea	Seoul	National Centers of Competence in Research	p	2007	1496	Dec 2014
Sweden	Uppsala	Swedberg Lab, 1	p	1957 (1976)	73	1976
Sweden	Uppsala	Swedberg Lab, 2	p	1989	1431	Dec 2014
Switzerland	Villigen	Swiss Institute for Nuclear Research/Paul Scherrer Institute, Piotron	π^-	1980 (1993)	503	1993
Switzerland	Villigen	Swiss Institute for Nuclear Research/Paul Scherrer Institute, OPTIS1 gantry	p	1984 (2010)	5458	2010
Switzerland	Villigen	Paul Scherrer Institute, Center for Proton Therapy, including the OPTIS2 gantry	p	1996	1906	Dec 2014
USA	Berkeley, CA	Lawrence Berkeley National Laboratory (184 inch cyclotron)	p	1954 (1957)	30	1957
USA	Berkeley, CA		He	1957 (1992)	2054	1992
USA	Los Alamos, NM	Los Alamos Meson Physics Facility	π^-	1974 (1982)	230	1982
USA	Berkeley, CA		ions	1975 (1992)	433	1992
USA	Boston, MA	Harvard Cyclotron Laboratory	p	1961 (2002)	9116	2002
USA	Loma Linda, CA	Loma Linda University Medical Center	p	1990	18362	Dec 2014
USA	Bloomington, IN	Midwest Proton Radiotherapy Institute, 1	p	1993 (1999)	34	1999
USA	San Francisco, CA	University of California, San Francisco - Cracker Nuclear Laboratory	p	1994	1729	Dec 2014
USA	Boston, MA	Massachusetts General Hospital Francis H. Burr Proton Therapy Center	p	2001	8107	Sep 14
USA	Bloomington, IN	Indiana University Health Proton Therapy Center	p	2004 (2014)	2200	2014
USA	Houston, TX	MD Anderson Cancer Center	p	2006	5838	Dec 2014
USA	Jacksonville, FL	University of Florida Health Proton Therapy Center	p	2006	5376	Dec 2014
USA	Oklahoma City, OK	ProCure Proton Therapy Center	p	2009	1690	Dec 2014
USA	Philadelphia, PA	Penn Medicine's Roberts Proton Therapy Center	p	2010	2522	Dec 2014
USA	Warrenville, IL	Chicago Proton Center	p	2010	1782	Dec 2014
USA	Hampton, VA	Hampton University Proton Therapy Institute	p	2010	1200	Dec 2014
USA	New Jersey/ Metro New York	ProCure Proton Therapy Center	p	2012	1168	Dec 2014
USA	Seattle, WA	Seattle Cancer Care Alliance ProCure Proton Therapy Center	p	2013	420	Dec 2014
USA	St. Louis, MO	S. Lee Kling Proton Therapy Center	p	2013	149	Dec 2014
USA	Knoxville, TN	Provision Center for Proton Therapy	p	2014	100	Aug 2014
USA	San Diego, CA	Scripps Proton Therapy Center	p	2014	220	Dec 2014
USA	Shreveport, LA	Willis-Knighton Cancer Center	p	2014	28	Dec 2014
		Total of all facilities (in and out of operation):				
		He	2054	1957-1992		
		Pions	1100	1974-1994		
		C-ions	15736	1994-present		
		Other ions	433	1975-1992		
		Protons	118195	1954-present		
		Grand Total	137179			

Abbreviations: P, protons, C ion, carbon ions; π^-, pion.

[a]Data collected by the Particle Therapy Cooperative Group.

Particle therapy centers statistics (December 2014) [7].

To date, 42 particle therapy centers are operational worldwide. Nevertheless, only 8 centers, 2 being in Europe (HIT-Heidelberg-Germany and CNAO-Pavia-Italy), provide hadrontherapy treatments. The HIT center started in 2009, the CNAO facility delivered its first carbon ion treatment in 2012. About 20 other particle therapy centers are planned to open by 2018. Figure 1-2 shows the repartition of the different particle therapy centers worldwide and their associated patient statistics.

Due to its recent increase of interest in medical physics, research groups show an evident enthusiasm for particle therapy. This field is currently explored in parallel at different modality levels, including dosimetry, quality assurance, technical devices, patient positioning and imaging, radiobiology and radiation protection.

1.1.3.2. Particle therapy advantages and disadvantages

In this section, particle therapy is compared to conventional radiotherapy. The advantages of particle therapy are twofold: physics and radiobiology.

Advantages:

- Due to their high mass (see section 1.2.2.2 for more details) the trajectory of protons and ions is straight and linear. They create a narrow Bragg peak at the end of the particle range where they release all the residual energy, at an arbitrary depth depending on the incident particle energy (see Figure 1-3). This leads to a sharp dose fall-off downward the dose maximum, straighter for protons than ions, as ions create more secondary particles that release dose beyond the Bragg peak. This ion-specific dose fall-off leads in few millimeters or centimeters to an insignificant dose.

Figure 1-3

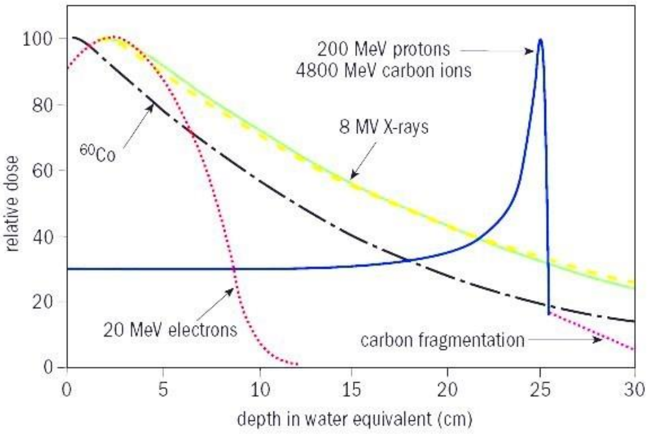

Representation of the depth dose for different "particles" used in radiotherapy. 20 MeV electrons (red dotted line), Co^{60} in black, 8 MV photons (green) and 200 MeV protons and 4800 MeV carbon ions in blue (Bragg peak at 25 cm depth). Carbon ions shows a carbon fragmentation tail, almost inexistent for protons

Particle therapy treatment planning takes advantage of the Bragg peak shape and dose fall-off to conform with a millimetric precision the dose distribution volume around the tumor volume for both superficial and deep-seated tumors in a much better way with respect to photons or electrons [8] [9]. This higher conformational ability lead therapists to prefer particle therapy especially in particular cases of prostate, uterus, salivary glands, brain or backbone tumors, for re-irradiation or boost treatment plans. The fact that no dose is delivered (or very few dose for ions) distal to the Bragg peak depth is the main geometric advantage of hadrons over photons, allowing to reduce significantly the dose to healthy tissues surrounding the tumor site. The irradiation of healthy cells potentially leads to late undesirable effects or radio-induced second tumors in the decades following the treatment, which is of course to be avoided as much as possible especially in children.

- The other beneficial aspect of particle therapy over conventional radiotherapy lies in the higher Relative Biological Effect (RBE) of charged particles (see section 1.3.6 for more details). While the RBE values of protons and photons are very close (respectively 1.1 and 1) [10], for heavier ions this RBE value increases drastically during the last millimeters of their pathway (corresponding to the part of the depth dose profile that is used to treat the tumor). For example, as seen in Figure 1-4 and Figure 1-16, in the Bragg peak area the Carbon ions RBE can reach a value of 3-5, according to the different studies published in the literature. This explains why particle therapy is potentially more efficient for tumor control than conventional radiotherapy at a radiobiology level, especially for radio-resistant tumors [11].

Figure 1-4

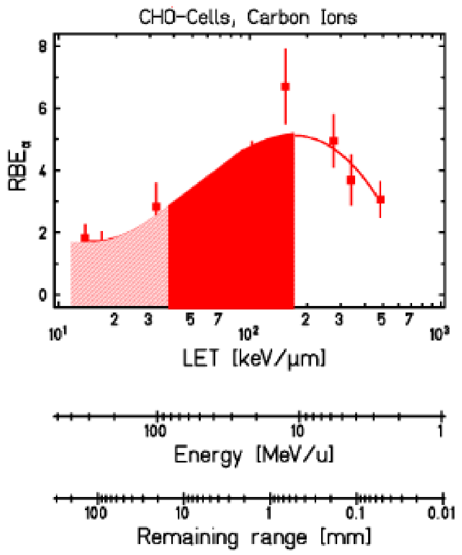

The carbon ions RBE according to the pathway depth of the particles in water [10].

- Since particle therapy is very efficient in delivering dose in a confined area, due to the Bragg peak dose gradient, and also due to high RBE, this technique is particularly indicated for hypo-fractionated treatments, allowing to reduce the number of sessions respected to photon therapy, without inducing any negative consequences for the patient at short and long term [12] [13].

The main disadvantages of particle therapy against conventional radiotherapy are also twofold: the first is the economic factor and the second is the patient positioning.

Disadvantages:

- Costs of particle therapy were largely discussed in the literature and is still today an open question [14] [15] [16]. Unfortunately, cancer centers are like companies and must consider their long-term financial outlook, meaning that radiotherapy facilities (hospitals or private centers) must use their initial investment wisely. The differences in capital cost for facility building and maintenance between particle therapy and conventional radiotherapy are huge. Estimates are nearly 130 million euros in the case of hadrontherapy [17], 90 million euros for proton therapy [18] [19]), and 2-5 million euros for the conventional radiotherapy. This large gap emerges mainly from the expenses due to the technologies required for particle beam production: a cyclotron or synchrotron is needed for particle therapy, whereas a linear accelerator (1-2 million euros) is sufficient for conventional radiotherapy.

  The global treatment cost of a particle therapy treatment to the patient was assessed by Orecchia [20] that showed that a hadrontherapy treatment in Italy amounts to 9400€, compared with 3,300€ for conventional photon radiotherapy and is nevertheless much lower than the chemotherapy treatment costs: 21,500€. These numbers have to be considered with care, as these techniques are not equivalent in terms of results.
- The benefits of particle therapy over conventional therapy was clearly demonstrated in the previous paragraphs, but its additional cost required for clinical practice is still discussed in the literature (Phase III of the clinical research) [18] [21]. To date, due to the recent application of the technique, data are still insufficient to confirm if there is a long-term decrease of radio-induced tumors. A reduction in particle accelerator costs or favorable clinical data gathered during the next years could tilt the balance in favor of particle therapy.
- Particle therapy can deliver more accurate treatments, taking advantage of the physical properties of particles, but there is no advantage in treating a patient with a millimetric dose conformation if the patient is not positioned with the same accuracy during the treatment sessions [22] [23]. Ideally, particle therapy should be associated with infra-millimetric positioning systems made of a high accuracy patient handling device coupled with an imaging system of the same accuracy. For moving tumors (like liver or lung tumors) gating or other motion management strategies are indispensable to guarantee a precise treatment and to avoid a loss of particle therapy therapeutic benefits. All these reasons make of the patient positioning a critical point in particle therapy. More accurate systems with respect to conventional photon radiotherapy (or equivalent to advanced photon radiotherapy units) means also higher expenses and longer treatment fractions, this last factor having a direct consequence on the patient throughput.

1.1.3.3. Suitable cases for particle therapy

As discussed in the previous paragraphs, particle therapy is more indicated than conventional radiotherapy in case of solid, localized and radio-resistant tumors [20]. The better conformation of ions, associated to their lower lateral scattering, allows a higher dose gradient around the tumor volume and is particularly efficient in complex geometry configurations where an OAR surrounds the target volume [24]. Treating highly resistant tumors with photons usually implies to deliver high doses to the target volume. Particularly in case of tumors with large volumes, this leads to unacceptable dose levels delivered to healthy tissues. Amaldi showed that particle therapy is to date the best solution for these specific configurations, due to the high dose gradients and the high RBE provided by this method [25]. Tsuji demonstrated on a large sample of patients that the majority of tumors having a low-response to radiation are better treated by particle therapy than conventional particle therapy [26] [27]. Schultz and Staab confirmed the higher efficiency of particle therapy on high resistant skull-based chordomas [28] [29] and extra-cranial chordomas [30] when compared to photons.

From the previous paragraph, it would be easy to extrapolate and affirm that particle therapy is more efficient than conventional therapy for any tumor type and hence should be the default radiotherapy strategy chosen by therapists. This is economically impossible, as explained above, due to the operating costs of the particle therapy centers and the number of patients to be treated. Only patients that could have a significant and demonstrated benefit should have recourse to this particular. Krengli and Orecchia [31] demonstrated that in Italy only 13% of the patients requiring a radiotherapy treatment are eligible for a proton therapy (see Table 1-1). This estimation falls to 6% for hadrontherapy (see Table 1-2). Moreover, there are also scientific (non-economic) reasons that photons may be preferred: photons have a sharper lateral penumbra than protons. Photons are also less sensitive to anatomical changes and don’t create a neutron bath.

Table 1-1

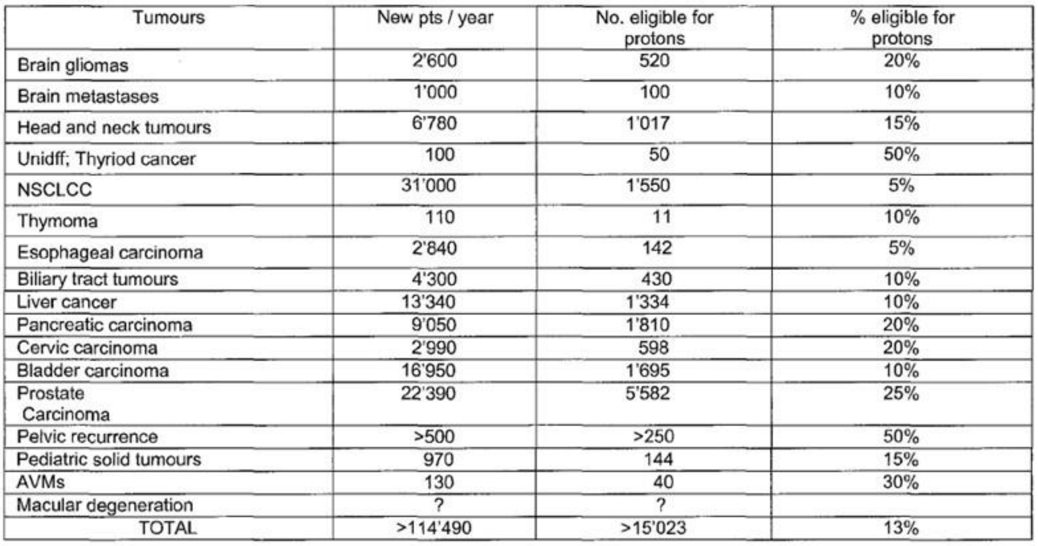

Tumours	New pts / year	No. eligible for protons	% eligible for protons
Brain gliomas	2'600	520	20%
Brain metastases	1'000	100	10%
Head and neck tumours	6'780	1'017	15%
Unidff; Thyriod cancer	100	50	50%
NSCLCC	31'000	1'550	5%
Thymoma	110	11	10%
Esophageal carcinoma	2'840	142	5%
Biliary tract tumours	4'300	430	10%
Liver cancer	13'340	1'334	10%
Pancreatic carcinoma	9'050	1'810	20%
Cervic carcinoma	2'990	598	20%
Bladder carcinoma	16'950	1'695	10%
Prostate Carcinoma	22'390	5'582	25%
Pelvic recurrence	>500	>250	50%
Pediatric solid tumours	970	144	15%
AVMs	130	40	30%
Macular degeneration	?	?	
TOTAL	>114'490	>15'023	13%

Patients eligible for protontherapy [31].

Table 1-2

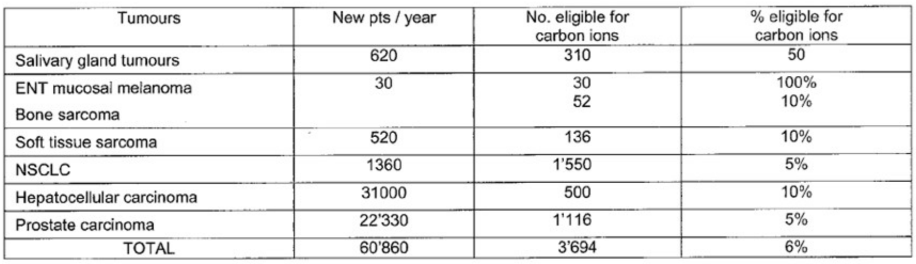

Tumours	New pts / year	No. eligible for carbon ions	% eligible for carbon ions
Salivary gland tumours	620	310	50
ENT mucosal melanoma	30	30	100%
Bone sarcoma		52	10%
Soft tissue sarcoma	520	136	10%
NSCLC	1360	1’550	5%
Hepatocellular carcinoma	31000	500	10%
Prostate carcinoma	22’330	1’116	5%
TOTAL	60’860	3’694	6%

Patients eligible for hadrontherapy [31].

1.2. Particle Therapy Physics & Radiobiology

The advantages of particle therapy comes from the Bragg peak shape, the small lateral diffusion (for ions only) and a higher RBE, as mentioned in the previous section. The maximum dose for photons occurs in the first few millimeters or centimeters, and slowly decreases with depth in the medium. On the contrary, protons and ions release their energy almost entirely at the end of their range. The lateral scattering of ions is smaller with respect to photons, due to the nature of their interactions. This is particularly true for heavy ions as these particles, due to their high mass, are less deviated during the interactions in the medium. Finally, the properties of the interactions of ions with matter are different at microscopic scales; many ionizations occur along the ion pathway, leading to a higher RBE factor than photons. These three advantages of the particle therapy are explained in details in the sections 1.2.2.1, 1.2.2.2 and 1.3.

1.2.1. Quantities associated to particle interactions with matter

Several dosimetric quantities have to be introduced to explain the theory of particle interactions with matter, such as the dose, the stopping power or the Linear Energy Transfer (LET). All useful radiation dosimetry quantities can be defined as physical quantities.

- The most used dosimetric quantity in radiotherapy is the physical absorbed dose D, representing the energy absorbed E_{abs} by a target of mass m:

  $$D = \frac{E_{abs}}{m} (J.kg^{-1} \text{ } or \text{ } Gy)$$

  The dose unit is by definition the Gray (Gy), which corresponds to 1 Joule per kilogram.
- The Stopping Power (STP) S is another quantity that is often referred for energy loss estimations in different materials. It represents the kinetic energy loss dE by the particles in a dx-thick layer of material. The stopping power is dependent of the incident particles energy and on the material composition.

  $$S = \frac{dE}{dx} (MeV.cm^{-1})$$

  For convenience, the STP is organized into look-up tables according to mass stopping power for specific materials. This quantity is almost equivalent in all materials, which is useful for approximations in heterogeneous media:

$$\frac{S}{\rho} = \frac{dE}{\rho . dx}\left(\frac{MeV}{g . cm^{-2}}\right)$$

These two quantities are negative, as particles lose energy in the medium. The STP look-up tables used in this report are all extracted from the NIST look-up tables [32]. Figure 1-5 reports the stopping power of protons in different materials (the negative sign of $\frac{S}{\rho}$ is not represented for convenience).

Figure 1-5

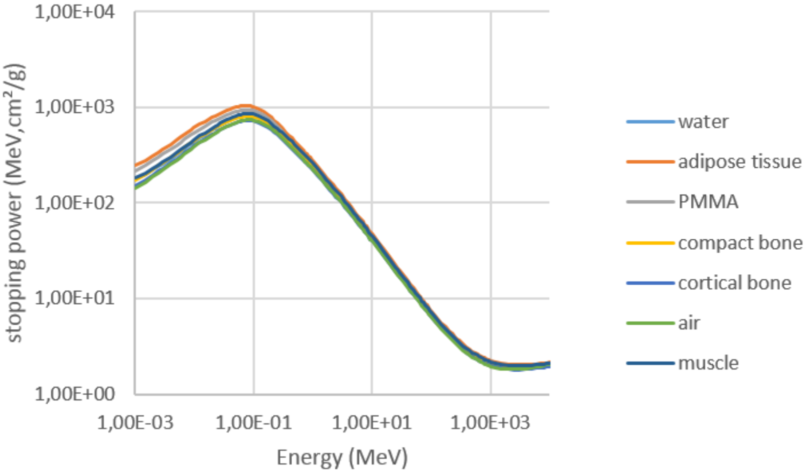

(Mass) Proton stopping power in different materials according to their energy [32].

- The STopping Power Ratio (STPR) is also often used in the case of energy loss comparisons in different materials, it is defined as the ratio of the mass stopping power in a material over the mass stopping power in water and is close to 1 for most of the media and energies involved in radiotherapy.

$$STPR_{mat,w} = \frac{\left(\frac{S}{\rho}\right)_{mat}}{\left(\frac{S}{\rho}\right)_{w}}$$

Figure 1-6 shows the STPR values for different biologic compounds commonly found in the human body in the particle therapy energy range. A method to determine $STPR_{mat,w}$ from Computed Tomography (CT)-images is report in Appendix A.2.

- In radiobiology, the Linear Energy Transfer (LET) is a quantity of interest. Its definition is similar to the stopping power ratio, but it considers the locally imparted energy in the target by both primary and secondary particles. The unit commonly mentioned in the radiobiology studies is the keV.µm^{-1} [33].

$$LET = \frac{dE_{local(prim.+sec.)}}{dx}(keV . \mu m^{-1})$$

The LET is usually defined with an associated *local cession of energy limit*, meaning that every secondary particle with an energy higher than this limit is not accounted in the energy locally absorbed by the target: this secondary particle releases most of its energy in a farther area. In the cases of high values for the local cession of energy limit (called *unrestricted LET conditions*), the LET and the stopping power definitions are equivalent.

The LET is commonly interpreted as an indication of the ionization density (also called the *quality of radiation* in radiobiology) along the particles pathway [34]. Low-LET radiations (such as photons) and high-LET radiation (such as ions) are respectively said to be *sparsely ionizing* and *densely ionizing*. The LET depends on the particle type, the particles energy and the medium composition. Table 1-3 provides some reference LET-values in water involved in the radiotherapy field.

Figure 1-6

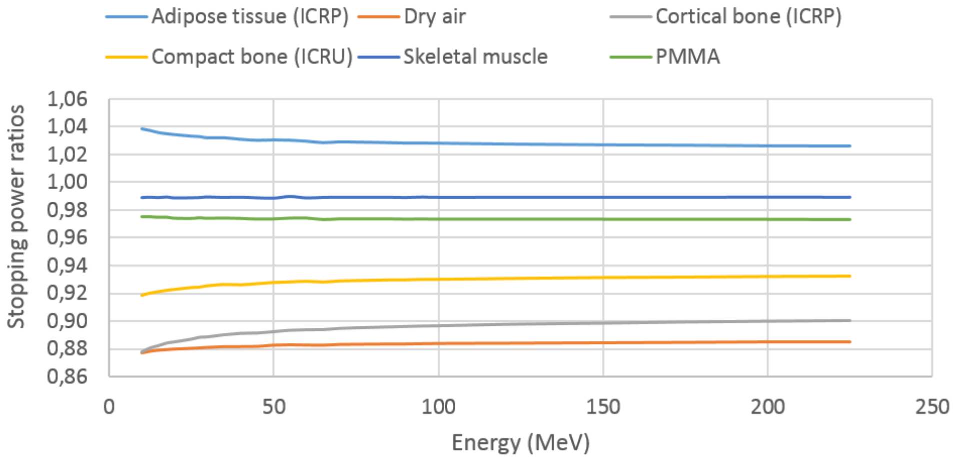

Stopping power ratios of common materials and energies used in the radiotherapy field, based on the NIST stopping power look-up tables [32].

Table 1-3

Particle (charge)	Energy	LET(KeV.µm^{-1})
Electron (-1)	10 KeV	2.30
	100 KeV	0.42
	1 MeV	0.25
Photon (0)	4-25 MeV	0.2-2
Proton (+1)	2 MeV	16
	5 MeV	8
	10 MeV	4
	200 MeV	0.4
α (+2)	5 MeV	95
Neutron (0)	5 MeV	3-30
^{12}C (+6)	10-250 MeV/u	170-14

LET values in water for some particles used in radiotherapy [34] [35].

1.2.2. Interaction of charged particles with matter

The interactions of charged particles with matter can be divided into 3 physical phenomena: the energy loss by Coulomb interactions with the electrons of the medium, the scattering due to Coulomb interactions with the medium nucleus and nuclear interactions, described briefly in the following paragraphs and in details chapter 2.

1.2.2.1. Energy loss

The STP S induced by protons interactions in a medium is entirely described by the Bethe & Bloch's formula [36]:

$$S = \frac{dE}{dx} = -\frac{4\pi}{m_e c^2} \times \frac{nz^2}{\beta^2} \times \left(\frac{e^2}{4\pi\varepsilon_0}\right)^2 \times \left[ln\left(\frac{2m_e c^2 \beta^2}{I \times (1-\beta^2)}\right) - \beta^2\right]$$

where the symbols used in the equation are explained in Table 1-4:

Table 1-4

Symbol	Definition	units
$m_e c^2$	Electron rest mass	511 keV
n	Electron density	cm^{-3}
z	Number of charge of the incident particle	-
β	Relativist term	-
ε_0	Vacuum permittivity	$8.854 \times 10^{-12} F.m^{-1}$
I	Main excitation potential	eV ($I \approx z \times 10eV$)

Definition of the symbols used in the Bethe & Bloch's formula.

In order to understand better this result, an excellent energy loss approximation was developed by Turner [37]. In this approach, the energy of the charged particles is lost by Coulomb interactions (inelastic collisions) with the electrons of the medium. These interactions are said to be *soft*, if the electron reaches an excitation state, or *hard* if it gets ejected (ionization) [38].

Let's consider an incident particle going through a medium at velocity V, and an electron at rest in a cylinder of length dx and width db lying at a distance b from the particle trajectory (see Figure 1-7).

Figure 1-7

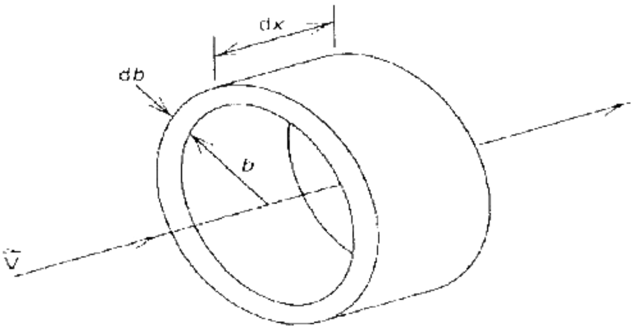

Determination of the energy loss by Coulomb interactions. In this approach a proton going through a media at velocity V interacts with an electron sited in a cylinder of length dx and thickness db at distance b from the incident particle trajectory. From Turner [37].

By symmetry, the resultant force applied to the electron by the proton during this interaction is null on the particle travel axis and directed only on the perpendicular axis. The expression of the Coulombic resultant force is:

$$F = k_0 z e^2 \frac{b}{r^3}$$

where r is the distance between the proton and the electron, k_0 is the Coulomb's constant ($k_0 = 8.9876 \times 10^9 N.m^2.C^{-2}$), e the electron charge and ze the ion charge. By a simple integration of the Newton's movement equations, Turner showed that the energy loss Q by an ion during a single interaction with an electron of the media is inversely proportional to the incident particle energy:

$$Q = \frac{2{k_0}^2 z^2 e^4}{mV^2 b^2}$$

Equation 1-1

where m is the mass of the incident ion. This is quite logical: the shorter the interaction, the lower the negative linear momentum felt by the proton. From Equation 1-1 it easy to estimate the energy loss of an ion in a thickness dx by summing the effects of the interactions with all the electrons of the medium in that thickness:

$$dE = -Q \times 2\pi n \times b \times db \times dx$$

with n the number of electrons per unit volume (assumed constant in the medium). The analytic expression of the stopping power of the ions in a homogeneous medium is then obtained by an integration on the b parameter:

$$S = \frac{dE}{dx} = -2\pi n \times \int_{b_{min}}^{b_{max}} Q \times b \times db = -\frac{4\pi {k_0}^2 z^2 e^4 n}{mV^2} \int_{b_{min}}^{b_{max}} \frac{db}{b}$$

$$S = -\frac{4\pi {k_0}^2 z^2 e^4 n}{mV^2} ln \frac{b_{max}}{b_{min}}$$

Equation 1-2

This expression of the STP corresponds to an excellent approximation of the experimental data shown in Figure 1-8. Equation 1-2 explains why an incident charged particle loses an increasing energy as its velocity slowly decreases (so does its energy). When the velocity of the particle is almost null, the stopping power expression reaches a singularity and the particle loses all its energy in few millimeters. This is called the Bragg peak (see Figure 1-8, left). The Bragg peak is characterized by a relatively constant dose in the entrance channel in the medium, followed by a quick dose increase in the last millimeters of the particle pathway. This property is very useful for saving the surrounding healthy tissues around a target volume, especially when associated with multiple beams intersecting the target volume. The depth of this peak depends on the incident energy of the particles (the higher the energy, the deeper the peak) and on the medium composition.

Another conclusion extracted from Equation 1-2 is that the STP depends directly on the square of the incident particles charge and is inversely proportional to their mass. This is physically quite logical: the higher the charge, the more energy transferred to the electrons by Coulombic forces and the higher the ion mass, the lower its deceleration due to the second Newton's law. Figure 1-9 shows the values of protons and carbon ions STP in water.

Figure 1-8

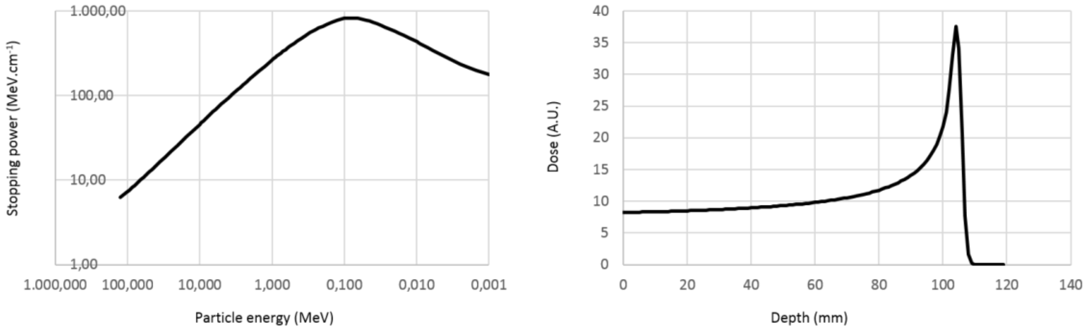

Left - STP of incident protons in water according to their energies [32]. Right – Depth dose (Bragg peak) of 120 MeV protons in water.

Figure 1-9

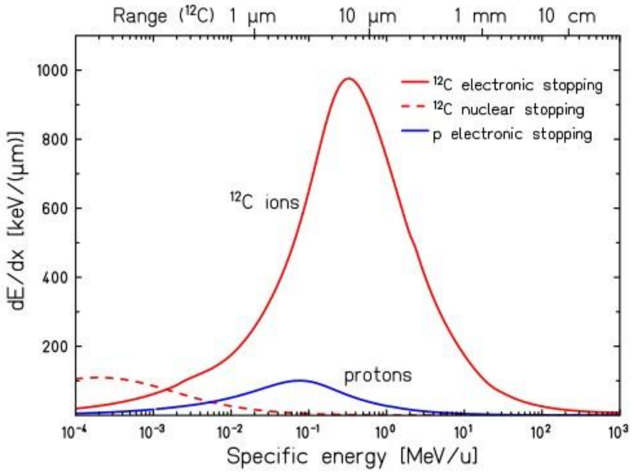

Comparison of protons and ions STP according to their specific energy [39].

This approach is only a model and any given ion has a different history depending on its previous interactions in the medium. These stochastic energy loss histories imply that not all ions come to rest at exactly the same depth but come to rest close to an average depth, called *range*, defined to be the depth of the 80% of the maximal dose, downward the Bragg peak. The particle range depends on the incident particle energy and the medium composition. For example, to deliver a maximal energy to a target located at 30 cm depth in water, 220 MeV protons, 430 MeV/u carbon ions or 600 MeV/u Neon ions are needed. Figure 1-10 shows the relationship between the range and the incident proton energy for some materials.

The energy dispersion (called also *energy straggling*) of a mono-energetic beam, due to the stochastic interactions through a material of thickness Δx , can be approximated by analytic Gaussian distribution [39]:

$$f(\Delta E) = \frac{1}{\sqrt{2\pi\sigma}} e^{\frac{(\Delta E - \overline{\Delta E})^2}{2\sigma^2}}$$

$$with\ \sigma = C \times \Delta x \left(\frac{1-\frac{\beta^2}{2}}{1-\beta^2} \right)$$

C being a parameter depending on the particle and material composition and β the ratio of the particle velocity over the light speed. The energy straggling roughly depends on the inverse of the square root of the ion mass, meaning that the straggling is larger for protons than heavy ions.

Figure 1-10

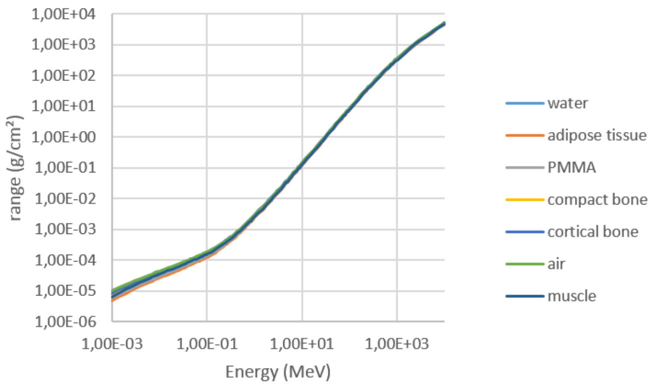

Protons range in different materials according to their energy [32].

The Bragg peak width, called range straggling, is a direct consequence of the energy straggling accumulated along the entire particle pathway in the medium. As mentioned in the previous paragraph, heavy ions are less subject to energy straggling than protons, the conclusion is similar for the range straggling. This property of the heavy ions interactions with matter is very important as it allows to create sharper dose gradients around the target volume at the Bragg peak depth with respect to protons, due to a better longitudinal dose control. As the energy straggling, the range straggling can also be fitted by a Gaussian function, whose Full Width at Half Maximum (FWHM) was estimated to be inferior to 2% of the particle range for protons (see Figure 1-11 and Table 1-5) and inferior to 0.5% for carbon ions [40].

Figure 1-11

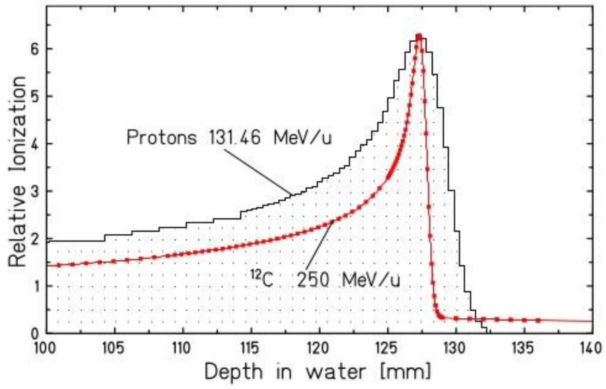

Range straggling for protons and carbon ions corresponding to the same range in water [39].

Table 1-5

Range	16.1mm	76.0mm	133.5mm	186.5mm
Range straggling FWHM	0.7mm	2.3mm	5.0mm	7.0mm

Range and associated range straggling of protons in water [35].

1.2.2.2. Scattering

Scattering theory is quite complex and is a central theme of this thesis. Chapter 2 is devoted to this topic, and the reader is invited to consult it for a detailed physical explanation.

The scattering of ions is mainly due to Coulombic interactions with nuclei. These interactions, being elastic, result in a deflection of the incident ions with a minimal energy loss. They can be divided into 3 interaction levels, all resulting from the same physics laws but divided according to the distance of the ion with the nucleus [40]:

- *Multiple Coulomb Scattering* (MCS): distant interaction from the nucleus, small deflection, common
- Plural scatter: medium distance from the nucleus, medium deflection, rare
- Single scatter: close distance from the nucleus, large deflection, very rare

The physical theory of these particular interactions was developed by Molière in 1948 and 1955 [41] [42]. As a first approximation, the lateral scattering of the charged particles can be represented as a Gaussian distribution whose FWHM increases with depth in the medium. The beam is said to *spread* in the media. Later, more accurate models were also developed, as double Gaussian, triple Gaussian or Cauchy-Lorentz distributions [35] [40]. The Molière description of this phenomenon is known to be too complex for a direct implementation in Pencil Beam Algorithms (PBA). Highland [43] [44] and then Gottschalk [45] [46] simplified this theory by means of different suitable approximations (see section 2.5.4) and provided simple and efficient models dedicated to pencil beam dose calculations.

Even if these interactions occur with the nucleus, there are not considered to be “nuclear interactions” (see next paragraph: Nuclear Interactions), as they are caused by electromagnetic forces of the atom nucleus. The nucleus internal state of the medium atoms doesn’t change during these interactions.

1.2.2.3. Nuclear Interactions

There are 3 different nuclear interactions [40]:

- *Elastic interactions*: Coulomb scattering (described in the previous paragraph) – not said to be a proper nuclear interaction. The nucleus is in the same state before and after the interaction.

$$ion^{+} + {}^{A}X \rightarrow ion^{+} + {}^{A}X$$

- *Inelastic interactions*: The incident ion transfers a part of its kinetic energy to the atom, which reaches an excited state. No new particles are created.

$$ion^{+} + {}^{A}X \rightarrow ion^{+} + {}^{A}X^{*}$$

- *Non-elastic interactions*: The energy transferred to the nucleus is sufficient to break the binding of the nucleus. In a recombination process the nucleus can emit new particles like protons, neutrons, fragments like α particles, or even heavy ions. The residual nucleus is of a different nature after the interaction.

$$ion^{+} + {}^{A}X \rightarrow +^{A-x}Y + (ion + n + p + \cdots)$$

The created fragments also go through the medium, like the primary incident particles, and are responsible of the *dose tail*, observable on the carbon ions depth dose curve in Figure 1-11.

1.3. Radiobiology of charged particles

1.3.1. History and first experiments

One century ago, and only a few months after the discovery of X-rays by Roentgen in 1896, the harmful effects of radiations on living organisms were demonstrated and used by Despeignes to heal a stomach cancer. This achievement is often considered as the beginning of both radiotherapy and qualitative radiobiology. More than 50 years later, Puck and Markus proposed a method assessing the lethal effects of radiation by the counting of colonies [47], marking the beginning of the quantitative radiobiology. This method, still used today and known as “Clonogenic Assay”, is considered the gold standard method to estimate the sensitivity of cell lines to general cytotoxic agents like radiations.

1.3.2. Linear Energy Transfer (LET) and Relative Biologic Effectiveness (RBE)

All kinds of radiation (α, β and γ) lead to ionizations and excitations of atoms in the matter they go through: photons by photoelectric absorptions, Compton interactions and pair production, and charged particles by Coulomb or nuclear interactions (see section 1.2.2) [48].

As explained in section 1.2.2.1, the STP of particles in a medium strongly depends on the incident particles mass and charge. For instance, the mass of a proton or a neutron is 1800 times higher than the mass of an electron: this explains why the interactions of an incident electron or proton have different consequences in the medium. The same statement would be more evident comparing α^{2+} particles or C^{4+} carbon ions with electrons.

To provide an analogy for this idea, ions ionize the atoms along a linear track without being really disturbed (like a truck entering at speed V in a wheat field) when an electron would change direction at every interaction in the medium (like a ball, at speed V would be ejected away or stopped after a couple of bounces in the same wheat field). As shown on Figure 1-12, the absorption of 1 Gy in a cell nucleus volume corresponds to about 1,000 photons tracks but only to 4 α particle tracks. This example shows how much energy is released per unit of distance along a high-LET ion track compared to a low-LET photon track.

Figure 1-12

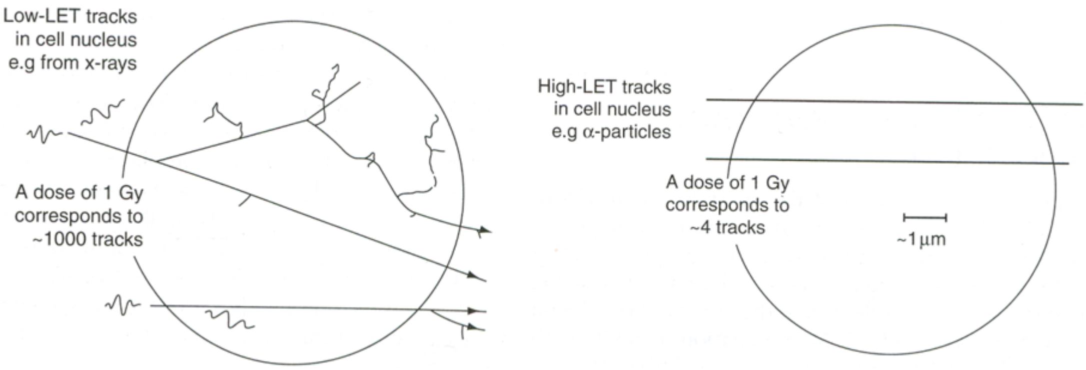

Particle track structures for low-LET radiation like photons (left) and for α particles (right). The circle represents the size of the nucleus of a typical mammalian cell. The tortuous nature of the low-LET secondary electrons tracks are in complete contrast with the straight high-LET α particles tracks [52].

In the last fifty years, numerous experiments have been carried out with different LET [49] [50] [51]. The general conclusion is that biologic effects of direct radiation are not constant with LET. The difference of the biologic effectiveness of radiation is generally expressed as the Relative Biologic Effectiveness (RBE):

$$RBE = \frac{D_{ref-250kV}}{D_{test}}$$

where $D_{ref-250kV}$ is the dose delivered in the reference conditions (250kV photons) and D_{test} the dose of the tested radiation required to obtain the same biologic effects with respect to the reference conditions. The lower the dose to equal the reference biologic effects, the higher the RBE.

As the LET increases, more cell killings occur per Gray. This can be understood from the very different track structures illustrated in Figure 1-12: a hit in the cell nucleus from a high-LET track causes major, irreparable damages in the same area while low-LET tracks release much less energy in the same area, the incident particles continuing on after each interaction. This has important consequences when interactions occur near the DeoxyriboNucleic Acid (DNA) as explained in the next paragraph. Common electron and photon beams used in radiotherapy have a RBE value of 1, protons RBE varies between 1 and 1.1 according to their energy, while the RBE of 5 MeV α particles can reach the value of 4.

1.3.3. Biologic effect

The ionization of an atom in a molecule results in the creation of *free radicals*: the whole molecule becomes unstable and reactive. As cells are composed of over 70% water, most of the free radicals are produced by radiolysis of water, especially OH•, which is very reactive with surrounding molecules and causes damages to them (see Figure 1-13). All components of the cell are damaged by direct and indirect effects of the water radiolysis: proteins, membranes, enzymes and DNA.

Figure 1-13

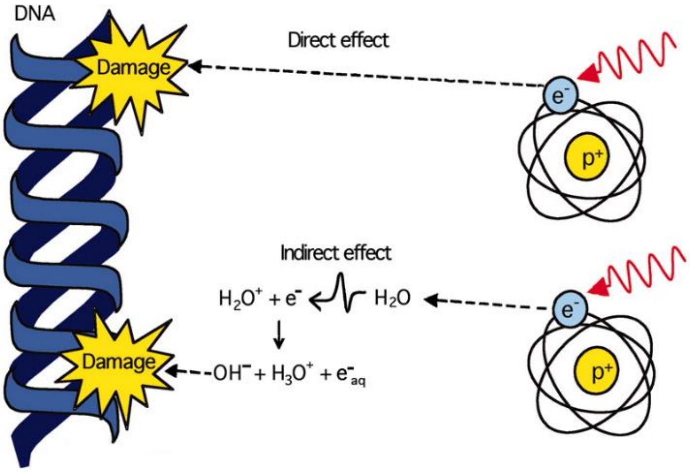

DNA damages induced by direct and indirect effects of the water radiolysis [53].

The probability of damaging a cell component remains quite small. A normal cell, due to the redundancy of the components it contains, deals easily with the loss of some of them. But this is not true for DNA, which is unique in every cell nucleus. Damages occurring to the DNA and induced by radiations lead to the loss or the modification of some genes, meaning a loss of specific functions sometimes essential for cell survival.

Cells have evolved to repair such damages and the DNA repair mechanisms are amazingly efficient. Table 1-6 shows an estimation of the number of DNA damages induced by a 1 Gy irradiation (≈ 200 000 ionizations in the nucleus). In spite of all these damages, most of the cells survive. Nevertheless, damages can occur on some sensitive parts of the DNA strands, preventing the cell from correctly dividing or leading to cell apoptosis. Due to disparities of the different reconstruction mechanisms efficiency, a Double Strand Break (DSB) is more efficient than a Single Strand Break (SSB) in damaging the cell (see section 1.3.4).

Table 1-6

Type of damage	Number of cases per Gy
DNA bases	**10 000**
SSB	**1 000**
Bridging DNA - Proteins	**150**
DSB	**40**

DNA damages induced by a 1 Gy irradiation inside a cell nucleus [53].

1.3.4. DNA repair and genomic instabilities

Multiple experiments have confirmed that ionizing radiations can cause genomic instabilities [54] [55]. In the previous paragraph we saw how radiation induces single or double strand breaks in DNA. Not only radiation, but also other natural, chemical toxicities or even the DNA replicating machinery itself can generate DNA damage. These damages, if not correctly repaired, can lead to apoptosis or to tumor development.

Genome integrity is essential to preserve the fidelity of the genetic information contained in every single cell, and for these reasons the human organism has developed different specific mechanisms to repair DNA damages.

Damage repair deals with SSB through base excision repair, nucleotide excision repair or mismatch repair [34]. Hereditary non-polyposis colorectal cancers provide examples of how defects in these genes can contribute to malignancy [56] [57]. DNA DSB are much difficult to deal with as the damages are physically more serious and some errors during the repair can occur. They are normally repaired at high fidelity through homologous recombination repair, which uses the sister chromosome as a pattern. For example mutations in BRCA1 and BRCA2 (human breast cancer genes) are involved in this pathway and contribute to the formation of solid tumor development [58].

In tumor cells, genomic instabilities show an increased rate, which may come from either increased rates of damages overloading the capacity of the normal repair systems to restore the integrity of the genome, or from imperfect repair mechanisms unable to deal with a normal amount of damages induced by toxic agents (such as natural radiation) [56]. Unfortunately, the genetic code structure is very sensitive: the removal of a single nucleotide can induce important biological consequences. If some cells immediately trigger an apoptosis or are destructed by the immune system, some of them amplify their duplication with an inexact genome and are not detected by the controls preventing them.

1.3.5. Cell survival curves – Linear quadratic model

A cell survival curve is a plot of cell surviving fraction against the dose (not only radiation but any toxic agent) and represents the percentage of surviving cells with respect to the control sample (generally a sample not subjected to any toxic agent). The shape of such graphs for irradiated cells, plotted on linear scales, is a sigmoid (Figure 1-14, left). It is often more convenient to plot these data on a logarithmic scale for the survival fraction, allowing the effects at very low survival levels to be noticeable and analyzed. The shoulder shape of such plots is shown on Figure 1-14 (right).

Figure 1-15 illustrates the range of radiosensitivity commonly found amongst human tumor cell lines. For example, in order to kill 99% of the HX142 neuroblastoma cells in a sample, only 4 Gy is needed, while 12 Gy are necessary to have the same effect on RT112 bladder carcinoma sample.

The model describing the Survival Fraction (SF) is the called the *linear quadratic model*:

$$SF = e^{(-\propto d - \beta d^2)}$$

Equation 1-3

where d is the radiation dose in Gy and α and β are intrinsic parameters depending on the cell line. The linear component is controlled by α and the quadratic component by β. The values of α and β for tumor cell lines is commonly included in the respective intervals [0.1-1] and [0.8-1]. The linear effect is supposed to be linked to the SSBs and the quadratic effect to the DSBs, which explains why the linear effect predominate statistically at low doses [34].

Figure 1-14

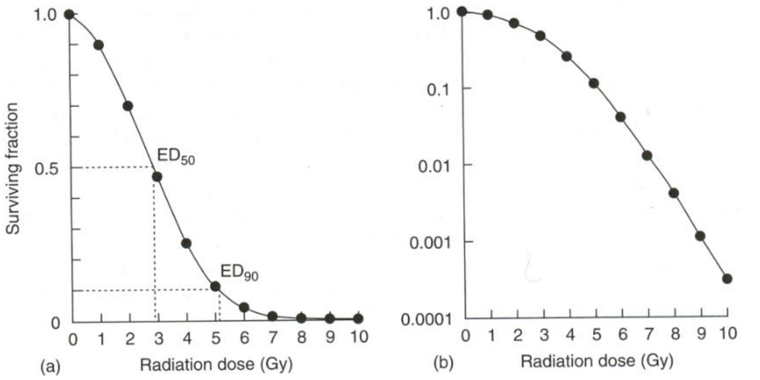

A typical cell survival curve for cells irradiated in tissue-cultures, plotted (a) on a linear scale. On the right (b) is shown the same data plotted on a logarithmic scale [48].

Figure 1-15

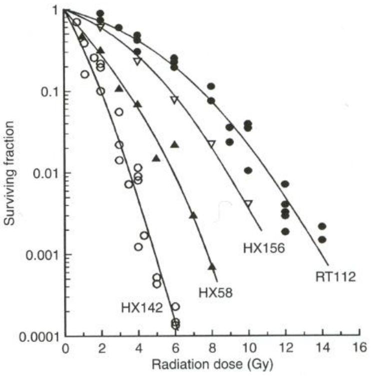

Cell survival curves for four representative human tumour cell lines irradiated at high dose rate [59]. HX142 neuroblastoma; HX58 pancreatic; HX156 cervix; RT112 bladder carcinoma.

While the effects of the dose are well known at high dose levels, it is not true at low doses. Because of the low incidence of radiation-induced cancers compared to natural incidences, it is very difficult to obtain an evidence of the risk magnitude at low doses (<200 mGy). The existence of a threshold is still a topic of controversy: British radiologists have failed in showing any increasing risk due to the low doses they delivered by radiologic imaging devices [60]. Some have even published results with a beneficial effect of radiations at low doses [61]. To date, the Board on Radiation Effect Research and the ICRP (International Commission of Radiation Protection) decided in 2006 that in the absence of a clear evidence to the contrary, the Linear No Threshold model (LNT model) should be assumed. Today, the LNT model is the most successful model according to the experimental data, and the most defended by the radiation protection experts.

1.3.6. The radiobiological consequences of charged particles

In particle physics, the measurement of the physical dose is insufficient to predict the effects at a cellular level. The RBE is also essential to accurately determine the consequences of radiations on a specific tissue. For example, the same physical dose delivered by photons and ions can have very different outcomes on the cell survival fraction (see Figure 1-17). The dependency of the RBE on the incident particle LET is still not well defined even with numerous publications available in the radiobiology field. Figure 1-16 summarizes the main results [62] [63]:

- The RBE of Carbon ions and Neon ions are in the range of [1-3] with respect to photons and 1.0-1.1 for protons. The RBE depends on the particle LET (itself linked to the particle energy).
- Between 1keV/µm and 10keV/µm the RBE slowly increases and equals 1-1.1. Protons reach a RBE of 1.1 at the end of their range.
- Between 10 and 100keV/µm the RBE increases substantially up to 2-3. In this area, the distance between the ionization sites along the particle pathway equals the diameter of the DNA helix (≈2nm) increasing the probability of DSBs.
- After 200 keV/µm, the RBE deeply falls below 1, probably due to an overkilling effect: energy is wasted in realizing many lethal lesions to the same cell when only one would be sufficient, which is energetically counterproductive.

Figure 1-16

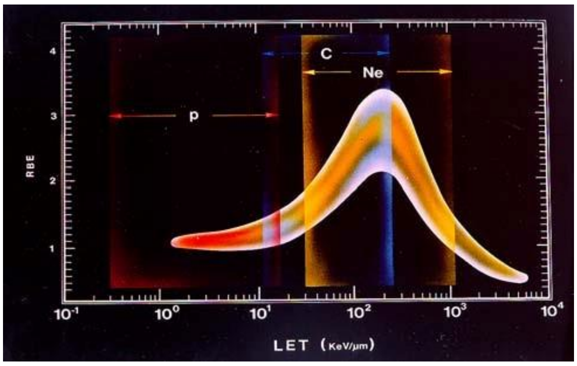

General RBE dependency according to the particle LET delivered in tissues. The range of LET are indicated for three ions commonly used in particle therapy.

Every ion has a different RBE value, according to its energy along the pathway (see section 1.2.2.1) and its physical properties as shown on Figure 1-17 representing different survival fractions induced by common particles used in radiotherapy.

An aim of particle therapy is then to take advantage of these results by using the maximal RBE values on the tumor volume (inducing an increased number of DSB) and the minimal RBE values in the upstream tissues. Protontherapy is used mainly for the ballistic properties of the protons pathway, but not for a superior RBE in the tumor area (RBE = 1.1) [64]. However, ions are definitely interesting for both advantages: for a high accuracy due to the particular ballistic properties and also a higher RBE in the tumor area than in upstream healthy tissues.

Figure 1-17

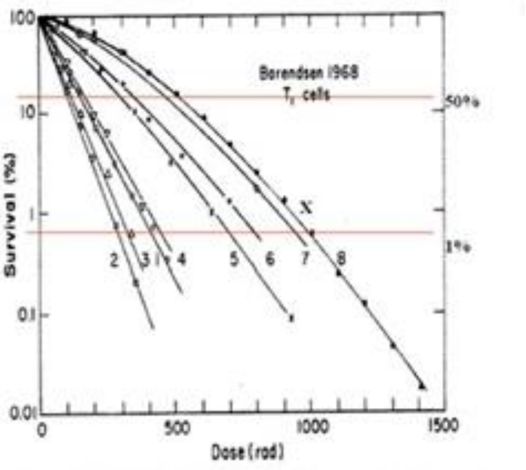

Survival fraction of different ions according to the dose [65]. 1- α 165keV/µm, 2- He 110keV/µm, 3- He 88keV/µm, 4- He 61keV/µm, 5- He 25keV/µm, 6- p 20keV/µm, 7- p 5.6keV/µm, 8- X 250kVp.

As explained above, physical doses are insufficient to build an accurate treatment plan, and radiobiologic doses have also to be considered. The RBE model implemented in commercial Treatment Planning Systems (TPS) is generally a black-box algorithm, inaccessible to the user. Commonly, it is based on the linear quadratic model (Equation 1-3) and uses α and β values extracted from experimental chordomas look-up tables, depending on radiation parameters such as the LET. The RBE model implemented in TPSs also depends on the radiation dose rate and on the dose fractionation, in order to account for the limited velocity and quantitative capacities of the cell repair mechanisms (Figure 1-18 [66]).

At a biological level, the RBE is also dependent on the oxygenation of the tissues [67]: the more hypoxic the cells, the lower the RBE, as oxygen increases substantially the radiosensitivity of the tissues via the creation of free radicals. Moreover, every tissue has a different RBE response to radiations. This can be an advantage in the case of a higher RBE for a specific tumor tissue with respect to the surrounding healthy tissues, or a disadvantage in the opposite situation.

Figure 1-18

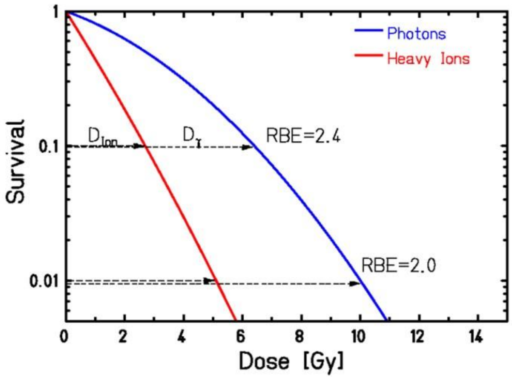

Fractionation effect on the RBE. For the same ion, a 3Gy fractionation induces a 2.4 RBE, for a 5 Gy fractionation the RBE decreases to 2.0 [68].

1.4. Particle therapy beam lines

1.4.1. Charged particle accelerators

The most common way to accelerate charged particles is to introduce them into an electric field, taking advantage of the Coulomb force. Using a static electric field is theoretically possible but would technically involve an extremely long accelerating section in order to reach the energies used for clinics (up to 250 MeV for protons and 500 MeV/u for carbon ions). For this reason, different systems were developed to reduce the volume of the accelerator devices, and mainly two methods are nowadays used in particle therapy facilities to accelerate charged particles: cyclotrons and synchrotrons. Synchrotrons offer a larger range of potential options compared with cyclotrons, but they are technically more complex and much more expensive.

1.4.1.1. Cyclotrons

Cyclotrons use the Lorentz force to drive many times the charged particles into the same small accelerating section. Cyclotrons are composed of two different “Dees”, two half circles (see Figure 1-19) inducing a vertical magnetic field $\vec{B}$. The particles travel in a vacuum chamber, either inside or between the dee regions. In each dee, the Lorentz force applied to a single particle of velocity $\vec{v}$ and charge q is:

$$\vec{F} = q\vec{v}\wedge\vec{B}$$

with $\vec{F}$, being the only force applied to the particle (gravity is neglected), perpendicular to the particle velocity and directed toward the center of the cyclotron. This unique force represents the centripetal force:

$$\overrightarrow{F_C} = \frac{mv^2}{r}\vec{u}$$

with $\vec{u}$ the vector unit perpendicular to the velocity of the particle and directed towards the cyclotron center in the dee plan and r the radius of the path.

In the absence of any other force than the Lorentz force, the radius of the path r is constant in a dee:

$$r = \frac{mv}{qB} = cst$$

Equation 1-4

As the mass of the particle, its charge and the magnetic fields are constant, once the particle enters in a dee, it follows a perfectly circular path inside the dee and exits from the symmetric position with respect to its entrance position (see Figure 1-19).

Each time the charged particle exits a dee, it is accelerated by the electric field between the two dees (called *acceleration gap* region) and acquires a higher velocity. This increased velocity, laps after laps, induces a larger radius of the path, until it reaches the periphery of the dee and gets kicked out towards the treatment room. The final trajectory of a typical proton is shown on Figure 1-19.

Figure 1-19

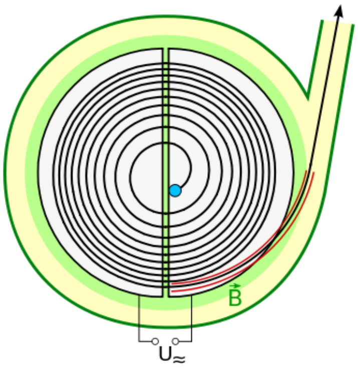

Cyclotron structure. A cyclotron is composed of 2 "dees" (white) subjected to a different potential. The charged particles are accelerated between the dees and their trajectory is curved inside the dees.

To accumulate positive accelerations, each time the particle exits the acceleration gap, the polarity of the electric field has to be reversed, as the particle will cross it again in the opposite direction after its turning back. Fortunately, the frequency of the polarity is constant, as the time for a proton to travel through the dee is constant whatever its energy/velocity (in the non-relativistic hypothesis):

$$\Delta t = \frac{pathlength}{v} = \frac{\pi r}{v} = \frac{m}{qB} = cst$$

with the help of Equation 1-4.

In the case of an improper frequency tuning of the radiofrequency device, the particle receives random positive and negative accelerations and is trapped inside the cyclotron.

Cyclotron devices produce charged particle beams of a single energy which is proportional to the square of the dees radius R:

$$E = \frac{1}{2}mv^2 = \frac{q^2R^2B^2}{2m}$$

with the help of Equation 1-4.

Here again, particle therapy centers are confronted by a device limitation: the cyclotron radius. In order to produce very energetic particles, the diameter of the cyclotron and the magnetic fields have to be increased. Nowadays, cyclotrons of a couple of meters are sufficient to produce protons for clinical applications, but they would be inadequate for accelerating ions like carbon ions to the clinical energy range (up to 500 MeV/u). In that case, synchrotrons are the best solution.

1.4.1.2. Synchrotron

The charged particles driving of synchrotrons and cyclotrons is based on the same physical laws. In synchrotrons, the particles are extracted from a particle injector and accelerated by a linear accelerator (*energy ramp*) until they reaches the ring and follow at each turn the same trajectory inside a ring-shaped vacuum chamber (see Figure 1-20).

Figure 1-20

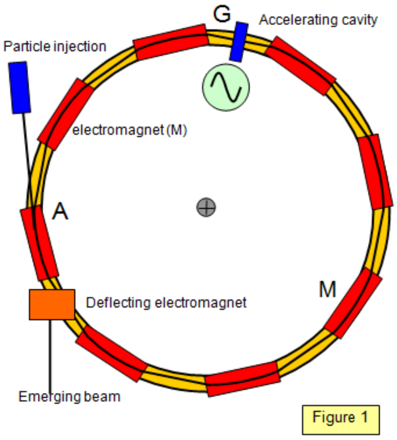

Synchrotron device. The particles are introduced from the particle injector (blue) into the linac and accelerated to the synchrotron ring. At each turn, the particles are accelerated in the accelerating cavity (blue) and deviated by the magnets (red and yellow) to circle many time on the same ring-trajectory.

Powerful magnets are used to drive the charged particles along the ring and make them go through the accelerating cavity many times, until they are kicked out from the device once the expected energy is reached.

As mentioned in the previous paragraph (“cyclotrons”), the radius of the path of the charged particles in a magnetic field is proportional to the particle energy. This means that the amplitude of magnetic field of the magnets has to increase to provide the adequate deviation driving the particles in the same ring, lap after lap. The magnetic field induced by the synchrotron magnets requires a high accuracy for both amplitude and frequency, as the magnets have to be synchronized with the particles position, lap after lap. Without this magnetic field synchronization during the entire beam production, the charged particles get lost in the ring edges before reaching the expected energy. This synchronization means that particles can only be accelerated by “bunches” or packets, when cyclotrons can produce a continue beam. Dipoles, quadrupoles and sestupoles are also used between the magnets to focalize the beam along its axis and avoid a spread due to the beam deviation.

The energy of the particles depends on the number of laps in the accelerating cavity. This technique is very convenient for changing the beam energy without modifying any downward beam line devices. The energy range reached by synchrotrons is much higher than the cyclotrons one, especially for ions: up to 500 MeV/u for the synchrotron available at the Centro Nazionale di Adroterapia Oncologica (CNAO, Pavia, Italy), and depends on the magnet power and frequency only, not on the radius of the device. When such energies are involved, the classical physics is not valid anymore and relativistic effects have to be considered. Synchrotrons are to date the only suitable way to accelerate ion beams dedicated to clinical treatments, when a cyclotron is sufficient for protontherapy treatments only. These technical considerations induce also higher costs of synchrotrons respected to cyclotrons.

1.4.2. Passive and active irradiation

At the accelerating device output (cyclotron or synchrotron), the beam has to be shaped in both amplitude (dose prescription) and shape (corresponding to the dose target volume) to correctly satisfy the dose distribution corresponding to the medical prescription. Mainly two different types of beam lines are implemented in particle therapy centers, the passive scattering and the active scanning systems. These two beam line structures use different techniques for modelling dose distributions in both longitudinal and lateral directions. The longitudinal spread of charged particle beams is the object of the next paragraph. The lateral spread of the charged particles is described in details in Chapter 2, the reader is invited to consult this entire chapter for details.

1.4.2.1. Spread Out Bragg Peak (SOBP)

Due to the high dose gradients in the Bragg peak region (see Figure 1-21), a mono-energetic beam of protons and ions is not suitable for covering a large tumor in the longitudinal direction with an even dose distribution. For this reason, many Bragg peaks of different energies have to be cleverly overlapped and weighted in order to create a flat dose distribution covering the whole target volume, but the dose has also to be as small as possible outside of it [29]. The lower limit in energy of the SOBP is set to reach the most proximal area of the target volume (minimum geometric Water Equivalent Depth (WED) of the target volume), and the upper limit in energy is set to reach the most distal area of the target volume (maximum geometric WED).

To evenly shape a dose on a depth segment, the most energetic Bragg peak is the only one to reach the most distal part of the PTV and has to deliver all the dose to this region by itself. Instead, the second most energetic Bragg peak provides only the dose that is missing at its own Bragg peak depth, as part of the dose was already delivered by the channel of the most energetic Bragg peak. The same process occurs down to the minimal energy, with always decreasing mono-energetic beam amplitudes, as part of the dose was already released by all the more energetic mono-energetic beams, as shown on Figure 1-21.

As explained in section 1.3.2, the physical dose is insufficient to describe the cell killing effect by ions. The approach explained in the previous paragraph is acceptable for protons, but for carbon ions the RBE factors have to be considered for the creation of an even radiobiologic dose along the SOBP. As the RBE substantially increases near the Bragg peak region, it creates a disequilibrium on the radiobiologic dose (relatively higher at the Bragg peak depth and relatively lower at the beam entrance). This induces a different mono-energetic beam weight set for heavy ions in order to build up a homogeneous radiobiologic dose delivered on the entire target volume (see Figure 1-22) [68].

Figure 1-21

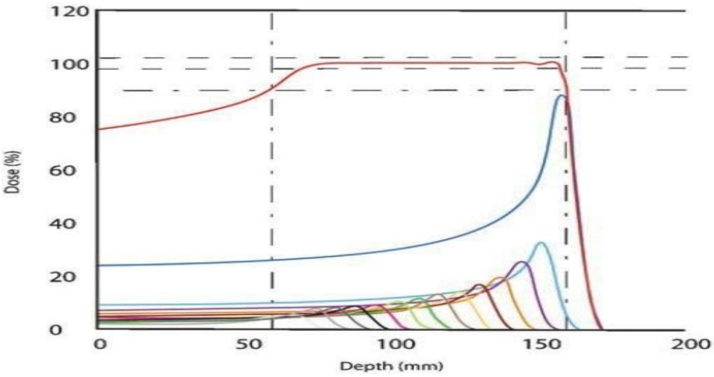

SOBP depth dose curve, to cover a [60-160] mm depth target volume with an even dose. The red depth dose curve (SOBP) is the overlapping of all the weighted mono-energetic beams (other colors). The amplitude of all the mono-energetic Bragg peaks represents their weight [69].

Figure 1-22

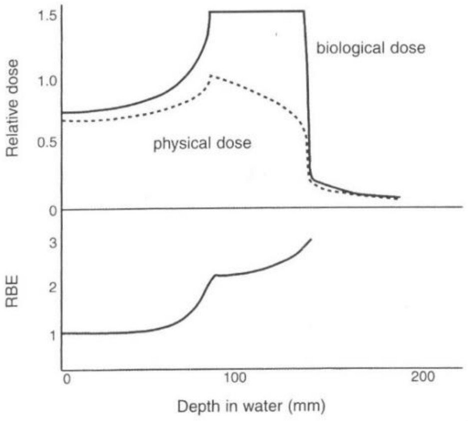

For heavy ions, the radiobiologic dose delivered to the target volume has to be even. This induces a disequilibrium of the physical dose released by the most energetic mono-energetic beams.

1.4.2.2. Passive scattering beam lines

The passive scattering beam line is the traditional beam line used by the majority of the particle therapy centers. In this approach, the beam is shaped in three dimensions by two types of passive devices: beam-modifier and beam-limiting devices introduced in the beam line [70]. A scheme of these different elements is shown on Figure 1-23.

- As the raw beam is too narrow (≈1-2 mm) to treat a whole target of some centimeters, a scattering system (or scattering foil with high atomic number Z material) is introduced in the beam line to spread the raw beam out as a Gaussian shape. Usually the scattering occurs in the two lateral dimensions (see chapter 2) in an efficient way to cover the entire target volume. A single scattering foil is sufficient for small field, but in the case of large field, a double scattering foil can be used. This double scattering foil is made of a central part of high Z material to strongly spread out the beam, and low Z peripheral materials to modulate the particles energy, creating a large and uniform field.

Figure 1-23

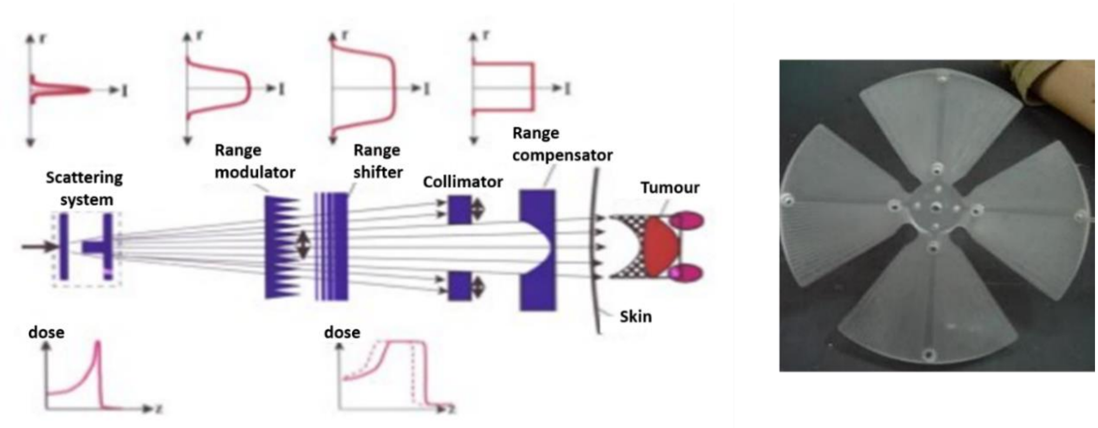

Left: Passive scattering beam line. Right: a rotating range modulator.

- The mono-energetic beam is broadened in depth by a range modulator (commonly a rotating disk with various media thicknesses that may rotate at around 50 Hertz), or by ridge filters (a material created to locally weight Bragg peaks by the insertion of different material thicknesses). This is needed to widen the energy spectrum of the output beam and cover the whole thickness of the tumor (SOBP creation). Immediately after the range modulator, a range shifter can be added, to shift the peak depth and make it correspond to the tumor depth. In other words, the range compensator acts on the thickness of the depth dose, and the range shifter on its depth offset.
- The last two elements, the collimator and the range compensator are specific to the patient:
    - The collimator (Figure 1-24 – left) blocks the parts of the beam not needed for treatment. Its shape corresponds the projection of the target volume (including margins) in the beam frame.
    - The range compensator (Figure 1-24 – right) introduces water equivalent material to compensate for the variations of media thickness in the upstream channel of the target volume and in the patient heterogeneities. The range compensator makes the beam perfectly conformed to the distal surface of the target volume (including margins). Range compensators are made of low Z materials (commonly PMMA), allowing the beam to lose energy with a minimal scattering effect.

This beam line is technically simpler than an active scanning system, but is also less efficient for sparing healthy tissues. Indeed, the dose is conformed only to the distal surface of the PTV and not to the proximal surface. Thus, healthy tissues that lie upstream from the target volume receive the full dose prescription. The only way to reduce this effect is geometrically dividing the dose into multiple beams at different entrance angles. Nowadays, most new particle therapy centers opt for an active scanning beam line.

Figure 1-24

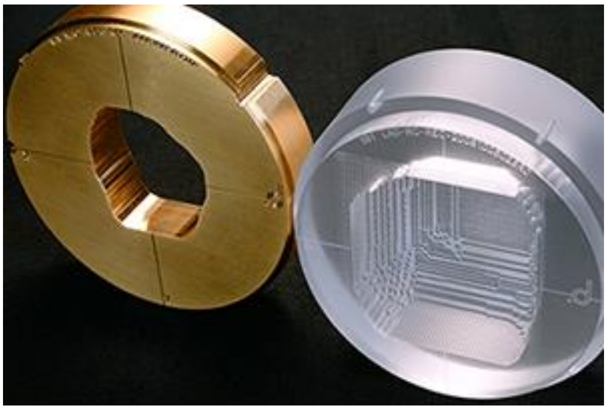

A brass collimator (left) and a PMMA range compensator (right).

1.4.2.3. Active scanning beam lines

The active scanning concept is very different from the passive scattering system as it uses a narrow beam that is steered to scan and cover the whole target volume [71]. In this approach, the target volume is segmented in iso-energy slices (see Figure 1-25). For cyclotrons, the beam energy slices are set up thanks to degraders (a material introduced in the beam line to reduce the beam energy) for each iso-energy slice. For synchrotrons, the particles exit from the device with the adequate energy.

In section 1.4.1 it was mentioned that, unlike photons, a charged particle trajectory is bent in the presence of a magnetic field and this allows it to drive accurately any charged particle beam. Two fast, orthogonal magnets coupled with the accelerator are used to steer the charged pencil beam to deliver the required dose across the iso-energetic slice in an area corresponding to the tumor projection (see Figure 1-25). This coupling is very important as the magnet intensity depends on the particle energy, and the fluence of each dose spot (or exposure time) has to correspond to the treatment plan parameters.

This process, repeated for each iso-energetic slice, shapes a 3D dose distribution corresponding exactly to the target volume and avoiding the useless irradiation at full dose of healthy tissues proximal to the target volume [72] [73]. Finally, the last advantage of this method is that no patient-specific element is needed in the beam line, and inhomogeneous irradiation is also possible. This is particularly useful for re-irradiation or so-called "*dose painting*" to consider RBE variations. Furthermore, because no material is introduced in the beam trajectory, the creation of neutrons and second particles contamination, problematic for both dosimetric considerations and radiation protection is avoided.

This method has also some disadvantages: the complexity of the method induces higher costs and more efforts on the commissioning and maintenance. Moreover the patient positioning has to be performed with high accuracy, so that each pencil is directed accurately at the right "target voxel". This is critical for the treatment of moving organs, like lungs or livers, and methods for organ motion management are required to synchronize the machine dose delivery with the patient breath cycle. Finally, in the last years, a significant work has been dedicated to TPS focused on active scanning systems and powerful algorithms were developed to optimize 3D dose distributions for multiple beams [74] [75].

Different methods exist to scan the dose in the iso-energetic slice: at least 4 of them are currently used in particle therapy centers (see Figure 1-26):

- Spot scanning and optimized spot scanning - step and shoot approach. An overlapping of dose spots is used to create homogeneous and heterogeneous 3D dose distributions. The optimized method is conceptually based on the same approach but the spot grid doesn't follow a regular grid but rather is an optimized spot site map computed by the TPS.
- Raster scanning and contour scanning: a continuous steering of the beam line is applied (called *wobbling*) allowing to draw homogeneous and heterogeneous 3D dose distributions according the velocity of the pencil beam across the iso-energetic slices.
- Generally a multi-beams treatment strategy can easily be used in a fixed beam line configuration in the treatment room, the different beam angles being performed by rotations and translations of a 6-degrees of freedom couch. Gantries can be used to provide beams from different angles, but due to the high mass of protons and especially heavy ions these structures are massive and extremely heavy (some hundreds of tons), and require considerable work for commissioning to achieve sub-millimetric accuracy. Some centers already use this system for protons, but heavy ion gantries are still largely considered a research project. To date, only a single gantry dedicated to both protons and ions is in clinical use at the Heidelberg Ion Therapy.

Figure 1-25

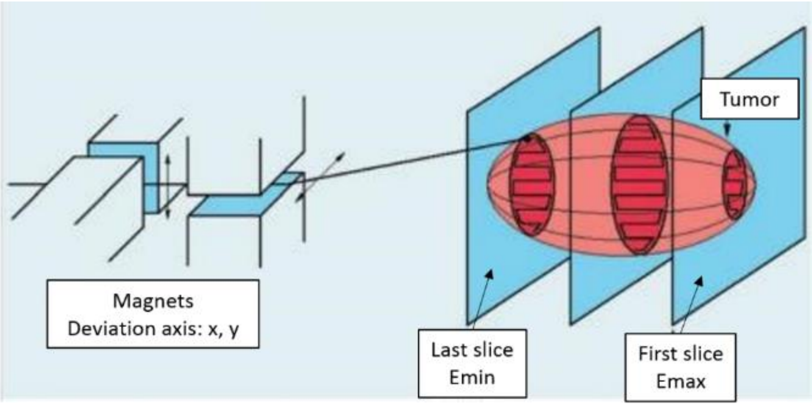

Active scanning beam line geometry [3]. The dose is delivered to iso-energetic slices after iso-energetic slices. In each iso-energetic slice, the beam is steered by fast magnets to laterally cover the dose map represented by the target volume projection.

Figure 1-26

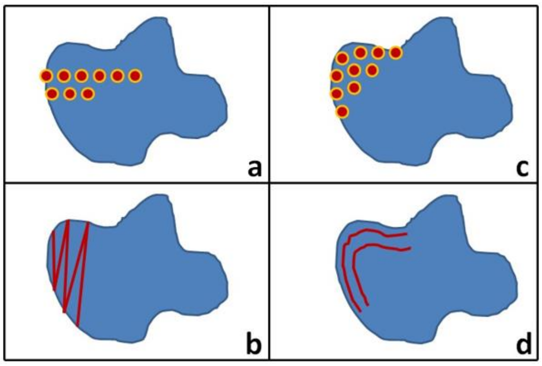

4 different dose delivery methods: a: spot scanning, b: optimized spot scanning, c: raster scanning, d: contour scanning [22].

1.5. Conclusion

Particle therapy is now considered a future direction in radiotherapy. In the previous paragraphs, the advantages and disadvantages of this technique were discussed at different levels such as physics, radiobiology and engineering. It is clear that in the first two fields, protons provide a benefit for patients with respect to conventional radiotherapy, but induces a more important effort for engineering and higher costs for the structure, devices, commissioning and maintenance.

Protons and heavy ions provide high dose gradients and higher RBE, both crucial parameters for tumor control and healthy tissues sparing. Both of these advantages are more significant for heavy ions and depend on physical properties of the particles. The ideal ion candidate for particle therapy would be a particle that induces a maximal RBE with a maximal dose conformality. Figure 1-27 shows these 2 factors for different particles compared to the conventional radiotherapy field.

Figure 1-27

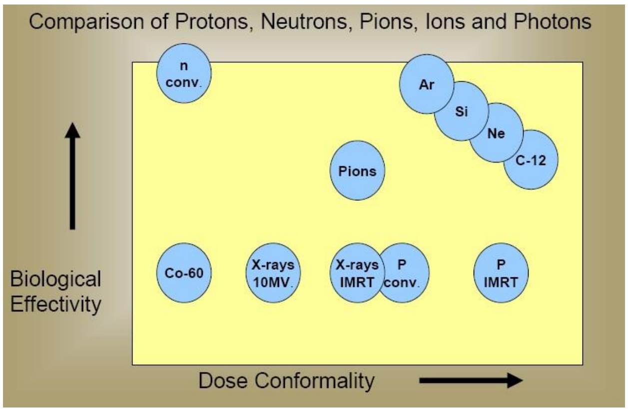

Dose conformality and RBE values for different ion species.

Heavier ions induce more fragmentations and secondary particles, creating a fragmentation tail (see Figure 1-11) that enlarges the irradiated volume and reduce the gradients in the Bragg peak area. Light ions have an inferior LET and are less efficient at a radiobiologic levels. A compromise has to be found and studies [25] [76] [77] showed that the best association between RBE and dose conformality is found for species of atomic numbers $Z \in [3; 6]$. Many other studies confirmed these results. This explains why efforts in particle therapy are focused on carbon ions.

To conclude, particle therapy can be considered the best option in the radiotherapy field for any type of solid tumors deeply seated or not. It allows treating the target volume with higher radiobiological doses respected to conventional radiotherapy and at the same time sparing healthy tissues surrounding it. If the particle therapy costs and technical needs were equivalent to conventional radiotherapy, the latter would nowadays be relegated to niche usage.

2. DOSE CALCULATION METHODS AND BEAM SPREAD COMPUTATION

2.1. The necessity of accurate dose calculation methods

In order to definite the beam parameters of an optimized treatment plan from radiologic images from a specific patient, a tool called a *Treatment Planning System* (TPS) is indispensable. A TPS is a software that allows simulation of different beam line settings and straightforward analysis of the 3D dose distribution in the patient. By analyzing the output dose distribution provided by the DCE included in a TPS, the dosimetrist can change the beam parameters or try different scenarios to build an optimized dose distribution. During the last two decades, inverse planning algorithms have become common and some TPS provide also the possibility to determine the optimized beam line settings to create arbitrary 3D dose distributions defined *a priori* with the help of dose constraints on different volumes defined in the input CT-images.

Dose calculation is often mistaken with treatment planning but it represents only a part of the entire treatment planning process. Treatment planning also includes other phases such as the acquisition of patient anatomical data, anatomy contouring or dose distribution analysis. It is nevertheless an essential part and needs to be sufficiently accurate to provide an efficient treatment to the patient. The accuracy of the dose calculation methods needs always to be considered in the context of:

- the CT calibration accuracy [78] [79]
- the patient positioning accuracy and its reproducibility [78] [80]

both inducing incorrect estimations of the dose delivered to the patient. The former leads to a systematic error during the treatment planning process, the latter to intrafractional and interfractional systematic and random errors (see section 1.1.3.2). These two issues are critical for particle therapy where high dose gradients are involved.

Dose calculation, for both Monte Carlo methods (MC, see section 2.2) and Pencil Beam Algorithms (PBA, see section 2.4), are not instantaneous and a trade-off has always to be found between dose accuracy and computation time. For clinical applications, dose accuracy prevails over computation time, but patient throughput requirements demand reasonable speed. The perfect TPS is then accurate and fast in predicting the dose delivered to the patient. With the development of more complex and more accurate dose calculation algorithms, coupled with inverse planning algorithms, the dose computation requirements increased substantially during the last decades and is to date only counterbalanced by technological improvements in hardware computational capacity.

Mainly four techniques of dose calculation are commonly used in clinics [40] and this report is focused on two of them: PBA and MC simulations. The MC is nowadays considered as the gold standard for dose calculation and is often used for both clinical dosimetric validations and dose distribution evaluations in the literature [81] [82]. The other two methods not mentioned in this thesis are Broad Beam Algorithms and Convolution Algorithms. PBA and MC simulations are the purpose of the following paragraphs of this report (section 2.2 and 2.4).

2.2. Monte Carlo (MC) Simulations

The Monte Carlo method models with a high definition the transport properties of particles and their consequences in any type of medium (homogeneous or heterogeneous). When a particle is generated, its interactions with the medium are followed along its pathway at two different levels [83]:

- The intrinsic parameters of the particles (like energy, position and direction) are updated due to interactions with the medium or an external field.
- The action of this primary particle on the environment is monitored (like the absorbed energy) and the secondary particles created during the interactions of the primary particle in the medium are also tracked.

The interactions (or *events*) occurring to a particle are simulated randomly according to empirical look-up tables representing with a high accuracy the real randomness of interactions properties with the matter. Figure 2-1 shows the example of a 2D dose matrix extracted from MC simulations.

Figure 2-1

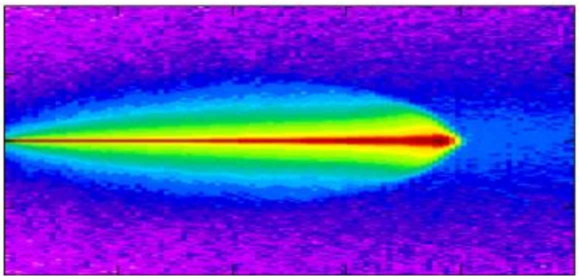

2D dose matrix extracted from a MC simulation (Fluka). The incident proton beamlet spreads in a water phantom. In this picture the dose is represented in a colorwash, logarithmic scale in order to show the trail of the protons (blue) highlighting the interaction randomness.

As each particle is generated, one by one, and followed along its pathway, the MC simulations are very time consuming (from some minutes to some days depending on the required accuracy and initial conditions). A delay of some hours or days to assess the dose distribution for a unique treatment plan is inconceivable for radiotherapy centers, which are compelled to invest in a parallel-computing environment (cluster). Indeed, the time dedicated to dose calculation for particle therapy treatment planning should be less than 5 minutes, roughly the time to generate a million of particles, which can lead to unconverged and inaccurate dose distributions, especially for large field sizes and complex geometries. Dosimetrists try several different treatment plan settings before finding the optimized treatment plan for a specific patient. With MC dose calculation methods only, only a few beam line settings can be attempted per day for a unique patient.

The critical parameters for MC simulations duration are the particle energy, the field size, the grid resolution of the measurement matrix (called "*tally*") in the medium and of course the number of the simulated particles (called "*histories*"). For example, using the MCNPx (for Monte Carlo N-Particle extended) MC code, a simple simulation of 10^7 protons of energy 100 MeV, 4 x 4 cm^2 field size in a bone phantom, lasts about 6 hours on a dual core computer (or 10 minutes on 64 processors). When higher energies are involved and all secondary particles like neutrons are followed, the computation time can be much longer: the simulation of a single 250 MeV proton beamlet (1 x 1 mm^2) in a large water phantom ($10 \times 10 \times 40\ cm^3$, tally resolution: $0.25 \times 0.25 \times 0.25\ mm^3$) involves the computation of 128 processors during 72 hours for the same number of particle histories [40].

2.2.1. Detailed History Method

Because MC algorithms achieve with high accuracy the particle interactions properties to any medium composition they are going through, it is considered as the gold standard especially for heterogeneous media. Historically, the particles were simulated and followed in their environment according to their physical properties, each event being simulated one by one, and each secondary particle being followed one after the other. This method, called as *Detailed History* is very accurate but extremely slow.

2.2.2. Condensed History Method

The previous process was improved by the development of the *Condensed History* method, which is the algorithm implemented in two famous MC radiation transport codes MCNPx and GEANT4 (Fluka). The Condensed History provides similar results with respect to the Detailed History but is much faster. This method divides the whole particle trajectory into a sample of segments, according to a statistical method derived from the scatter theory, creating a randomly oriented walk of the particles in the medium, statistically very similar to the real pathway of the particles [83]. The number of segments depends mainly on the atomic number of the media, the lower the atomic number Z, the longer the segments. Each segment invokes an approximate description of the interactions that occur on the entire segment, extracted from models or experimental data. As every single event is not considered one by one anymore, but by groups or clusters, the computation time is much lower than the Detailed History method. Unfortunately, the Condensed History is still today inappropriate for achieving high patient throughput of particle therapy centers due to its slowness. Nevertheless, it remains a powerful and accurate tool for dose computation in heterogeneous media and is the reference method to validate any survey or investigation in the research fields, where time is not as important as it is for clinics [84].

2.2.3. Track-Repeating Methods and Graphical Processing Unit

During the last decade, a particular effort was dedicated to track-repeating algorithms, mainly thanks to the Yepes' work [85] [86] [87] to develop faster and accurate MC simulation algorithms. This approach uses sets of pre-calculated particles pathways in water enlarged or stretched according to the stopping power ratio of the medium. As the particle trajectories are pre-computed and stored, as if they were look-up tables, they are straightforwardly available and their effects are summed, saving the computation time that is usually dedicated to this process in the Condensed History method. Nevertheless, this adds another approximation that induces inaccuracies. Moreover, as many particles trajectory are anyway involved, it requires an important set of computation devices for a unique dose calculation. These two reasons explain why this new method is not commonly used by particle therapy centers [85].

2.3. Ray Tracing Algorithm

The Ray Tracing Algorithm (RTA) represents a historical dose calculation approach used in clinics when TPS didn't exist more than 30 years ago. This very simple approach is based on depth dose curves only and doesn't consider any lateral scattering. Each voxel of the output volume receives a dose that depends on the WED in medium that is crossed by the ray extending from the source to the voxel. The WED l at depth z on the ray axis is computed by Equation 2-1, the dose D being extracted from depth dose curves in water DDC_w (from analytic models or experimental data, see Figure 2-2).

$$D(z) = DDC_w(l)$$

$$with\, l = \int_0^z STPR_m \times dx$$

Equation 2-1

where $STPR_m$ is the stopping power ratio of the material over water for the particle. A reference proton depth dose curve implemented in dose calculation algorithms can be computed from the Bortfeld model [88].

Figure 2-2

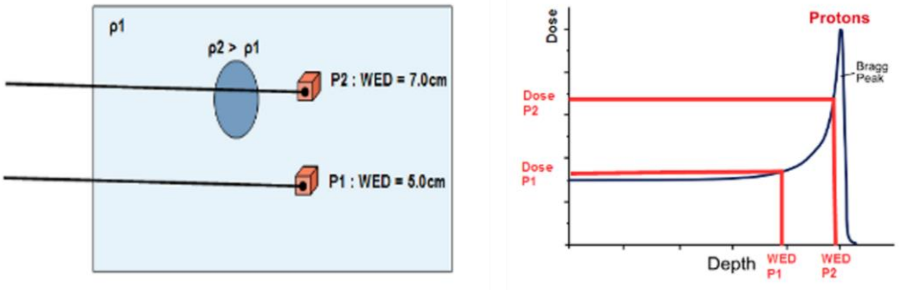

Left: calculation of the WED for two different voxels in a heterogeneous medium. Right: Calculation of the primary dose from analytic or experimental depth dose curves in water. The dose delivered to the two voxels of interest are determined from the WED computed on the left figure.

Only the voxels contained in the beam frame receive a dose contribution. This means that the dose distributions created by this algorithm have no penumbra and are accurate only in the central region of large fields. This method is valid for homogeneous media and simple geometric configurations only. Moreover, the proton and ion Bragg peak flattening due to the presence of heterogeneities in the medium is not observed on RTA dose distributions [89].

2.4. Pencil Beam Algorithms (PBA)

2.4.1. Generalities

The PBA methods for charged particles consider at least the lateral scattering induced by Multiple Coulomb Scattering and provides accurate dose distributions in many configurations where the RTA fails. The basis of the PBA algorithms were broadly described in the literature [40] [70] [71] [90] [91] [92] [93] [94] [95] [96] [97]. This method decomposes in the beam frame a broad beam into small *beamlets*. Each beamlet is associated to a 3D dose distribution representing the elementary dose contribution released by the beamlet into a reference medium (usually water), called the *pencil beam dose kernel*. The final dose distribution is then the sum of all the elementary dose contributions coming from all the active rays in the beam frame. This method seems similar to MC simulations, but the elementary dose distributions coming from each ray are already well defined mathematically in a tridimensional geometry, generally from semi-empiric equations, and don't need to be simulated. According to the initial settings, the PBA computation times stretch from some seconds to some minutes.

2.4.2. Theory

A convenient description of the dose distribution shape, coming from a single elementary beamlet directed along the z^* axis in the Cartesian geometry, implies the decomposition into two terms of the delivered dose d to an arbitrary point $P(x, y, z)$ [98]: the central-axis term $C(z)$, depending on the depth only, and the off-axis term $O(x', y', z)$ depending on both the transverse distance from the beamlet axis z^* and the depth in the medium.

$$d(x, y, z) = C(z) \times O(x - x_0, y - y_0, z)$$

Equation 2-2

where x_0 and y_0 are the coordinates of the z^* axis in the (xOy) beam frame (see Figure 2-3).

In the previous paragraph, the total dose was defined as the sum of the contributions of all the elementary beamlets going through the beam collimator. The expression of the global dose $D(x, y, z)$ to a point $P(x, y, z)$ is then expressed as following:

$$D(x, y, z) = \iint\limits_{\substack{beam \\ aperture}} d(x', y', z) \times dx' \times dy'$$

$$= \iint_{\substack{beam\\aperture}} C(z) \times O(x' - x_0, y' - y_0, z) \times dx' \times dy'$$

Figure 2-3

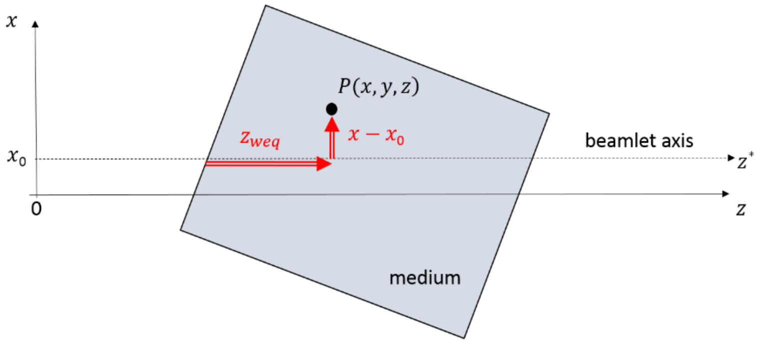

Description of the geometric configuration for the dose decomposition of an elementary beamlet into a central axis term and an off-axis term. The beam axis is represented as a plain line and the ray axis z^* as a dotted line. This figure would be equivalent in the $(y0z)$ plan.

By applying this formula to infinite broad beams in a semi-infinite water phantom (guaranteeing the lateral scatter equilibrium) with the surface phantom perpendicular to the z axis, it is easy to show that the central axis term $C(z)$, constant for all beamlets at depth z, can be arbitrary chosen to correspond to the measured depth dose in the medium. This implies a normalization of the off-axis term to 1 when integrated on an infinite orthogonal plan at any depth z:

$$D(x, y, z) = C(z) \times \iint_{\substack{beam\\aperture}} O(x' - x_0, y' - y_0, z) \times dx' \times dy'$$

The general expression of the dose in a water equivalent medium is then expressed for a water equivalent depth z_{weq} as:

$$D(x, y, z) = DD_w\left(z_{weq}\right) \times \iint_{\substack{beam\\aperture}} O(x' - x_0, y' - y_0, z)\, dx'\, dy'$$

$$with\ \forall z, \int_{-\infty}^{\infty} \int_{-\infty}^{\infty} O(x' - x_0, y' - y_0, z)\, dx'\, dy' = 1$$

Equation 2-3

where DD_w is the depth dose curve measured in a semi-infinite water phantom in broad beam conditions.

Generally, the off-axis term is assumed to be described by the off-axis term in water. A more accurate description of the off-axis expression is dealt in details in Chapter 3, accounting for the heterogeneities along the beamlet pathway. The off-axis term distribution for charged particles was proposed by Eyges [99] as a 2D single Gaussian shape, considering the small-angle approximation of Multiple Coulomb Scattering (MCS):

$$O(x,y,z) = \frac{1}{2\pi\sigma^2(z)} e^{-\frac{x^2+y^2}{2\sigma^2(z)}}$$

Equation 2-4

where σ is called the Standard Deviation of the Pencil Beam Profile (SDPBP) and is responsible of the beam spread due to the interaction of the particles in the medium. The $\sigma(z)$ values are difficult to assess as they depend on the energy of the beam but also on the medium composition and geometry crossed by the particle beamlet. As each beamlet has a different story in a heterogeneous media, the $\sigma(z)$ functions need to be computed individually for each beamlets.

Look-up tables of $\sigma_{water}(z)$ in water are easily found in the literature [70] and implemented in basic algorithms for dose calculation in water equivalent media. In the presence of heterogeneities, the general SDPBP $\sigma(z)$ is usually replaced by $\sigma_{water}(z_{weq})$ as a first approximation, but as shown in the Chapter 3 and 4 of this report, this approximation can lead to significant errors. The construction of an accurate $\sigma(z)$ function for any energy and any configuration in heterogeneous media is the one of the aims of this thesis and is established in Chapter 3. The reader is then invited to consult this chapter for more details.

The expression of the single Gaussian off-axis term for charged particles (Equation 2-4) is in agreement with the normalization required in Equation 2-3. This model is only an approximation to account mainly for MCS, plural and single scatter, but not for nuclear interactions. More complex and accurate models are proposed in the literature [40] [71] [100] [101] but involve longer computation times.

From Equation 2-3 and Equation 2-4, the final expression of the 3D dose distribution of a unique pencil beam directed along the z^* axis is then:

$$d(x,y,z) = DD_w(z_{weq}) \times \frac{1}{2\pi\sigma^2(z)} e^{-\frac{(x-x_0)^2+(y-y_0)^2}{2\sigma^2(z)}}$$

Figure 2-1 shows a 2D slice of this dose distribution induced by an elemental beamlet in water on a logarithmic dose scale for a better visualization of the beam spread.

This formula is very accurate to assess the dose to an infinitesimal point by summing the dose released by all the beamlets going through the aperture. In clinics instead, the dose distributions are usually determined in voxelized volumes, each voxel containing the averaged dose in its volume, as if the energy released in each voxel was evenly distributed inside it, which is physically wrong: some parts of the voxel receive more dose than others. To consider this *volume effect*, the dose Δ released to a voxel $P(x,y,z)$ of dimension $w_x \times w_y \times w_z$ from a pencil beam directed along the z^* axis is then expressed as:

$$\Delta(x,y,z) \ = \frac{DD_w\left(z_{weq}\right)}{2\pi\sigma^2(z)} \int\limits_{y-w_y/2}^{y+w_y/2} \int\limits_{x-w_x/2}^{x+w_x/2} e^{-\frac{\left(x'-x_0\right)^2+\left(y'-y_0\right)^2}{2\sigma^2(z)}} \times dx \times dy'$$

reasonably assuming that the depth dose curve DD_w and σ are constant in the voxel. As x and y are independent, Δ can be simplified as following:

$$\Delta(x,y,z) \ = \frac{DD_w\left(zz_{weq}\right)}{2\pi\sigma^2(z)} \times \int\limits_{x-\frac{w_x}{2}}^{x+\frac{w_x}{2}} e^{-\frac{\left(x'-x_0\right)^2}{2\sigma^2(z)}}\, dx' \times \int\limits_{y-\frac{w_y}{2}}^{y+\frac{w_y}{2}} e^{-\frac{\left(y'-y_0\right)^2}{2\sigma^2(z)}}\, dy'$$

By doing the change of variables $X = x - x_0$ and $Y = y - x_0$,

$$\Delta(x,y,z) \ = \frac{DD_w\left(z_{weq}\right)}{2\pi\sigma^2(z)} \times \int\limits_{x-x_0-\frac{w_x}{2}}^{x-x_0+\frac{w_x}{2}} e^{-\frac{X^2}{2\sigma^2(z)}}\, dX \times \int\limits_{y-y_0-\frac{w_y}{2}}^{y-y_0+\frac{w_y}{2}} e^{-\frac{Y^2}{2\sigma^2(z)}}\, dY$$

$$= \frac{DD_w\left(z_{weq}\right)}{2\pi\sigma^2(z)}$$

$$\times \frac{\sqrt{\pi}}{2} \times \sqrt{2\sigma^2(z)} \times \left[erf\left(\frac{x - x_0 + \frac{w_x}{2}}{\sqrt{2\sigma^2(z)}}\right) + erf\left(\frac{x_0 - x + \frac{w_x}{2}}{\sqrt{2\sigma^2(z)}}\right)\right]$$

$$\times \frac{\sqrt{\pi}}{2} \times \sqrt{2\sigma^2(z)} \times \left[erf\left(\frac{y - y_0 + \frac{w_y}{2}}{\sqrt{2\sigma^2(z)}}\right) + erf\left(\frac{y_0 - y + \frac{w_y}{2}}{\sqrt{2\sigma^2(z)}}\right)\right]$$

with erf the error function corresponding to the empiric integral of the Gaussian function. The direct expression of the released dose Δ to a voxel $P(x,y,z)$ of dimension $w_x \times w_y \times w_z$ from a pencil beamlet directed along the z^*axis equals:

$$\Delta(x,y,z) = \frac{DD_w\left(z_{weq}\right)}{4} \times \left[erf\left(\frac{x - x_0 + \frac{w_x}{2}}{\sqrt{2\sigma^2(z)}}\right) + erf\left(\frac{x_0 - x + \frac{w_x}{2}}{\sqrt{2\sigma^2(z)}}\right)\right]$$

$$\times \left[erf\left(\frac{y - y_0 + \frac{w_y}{2}}{\sqrt{2\sigma^2(z)}}\right) + erf\left(\frac{y_0 - y + \frac{w_y}{2}}{\sqrt{2\sigma^2(z)}}\right)\right]$$

Equation 2-5

Finally, the global dose D_Δ released in the voxel is the sum of the contribution of all the pencil beamlets:

$$D_\Delta(x,y,z) = \sum_{pencil\ beams} \Delta(x,y,z)$$

2.4.3. Discussion

The only undetermined parameter in Equation 2-5 is the SDPBP σ of each pencil beam. In heterogeneous media, the usual approximation of this parameter is extracted from beamlet spreads in water, scaled to the water equivalent depth z_{weq}, but can be insufficient for computing accurate dose distributions dedicated to radiotherapy treatments, especially in the presence of air gaps or dense materials like cortical bones. Chapter 3 deals with a differential model developed to account correctly for these heterogeneities.

A disadvantage of this model is called the "*central axis approximation*": only the heterogeneities on the beamlet axis are considered for the SDPBP computation, leading to substantial errors near sharp edged heterogeneities or asymmetrical geometric configurations. Figure 2-4 shows an example of the inaccuracies induced by the central axis approximation: the PBA model extrapolates the information on the beamlet axis to the infinite transverse plan, which is conceptually valid only for infinite slabs perpendicular to the beamlet axis (one of the Fermi-Eyges prerequisites in the construction of Equation 2-4 [99]). Nevertheless, Petti [91] showed that this approximate model is able to predict the presence of hot dose spots due to the presence of heterogeneities with a general accuracy of 2-3%, which is acceptable and much better than RTA estimations. It is today the best trade-off between dose distribution accuracy and fast computation time.

Figure 2-4

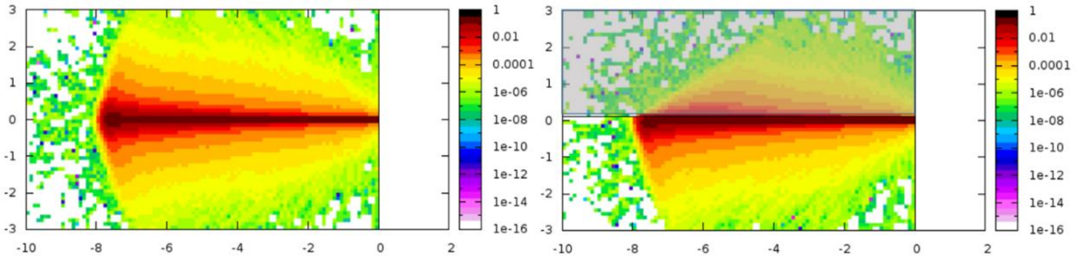

Monte Carlo simulations of two beamlet spreads in water only (left) and in a medium made of two regions: water (white) and cortical bone (grey). The dose is represented on a logarithmic scale. As the beamlet spread is based on the media crossed by the beamlet axis only (in water for both cases), the dose distribution calculated by the PBA model for these two configurations would be identical which doesn't correspond to experimental and MC measurements as shown on this figure.

PBAs are the dose computation methods implemented in commercial TPS (Syngo from Siemens, XiO from Elekta and Eclipse from Varian), and are based on methods published in the literature for both Passive Scattering and Active Scanning beam lines [70] [101] [102]. The PBA models for active scanning also consider the nuclear interactions. Knutson [40] proposed a detailed description of a second pencil beamlet computing the 3D dose distributions released by nuclear interactions only (see section 2.5.6), added to the primary pencil beamlet. Even if this correction can be neglected for passive scattering, it becomes indispensable for active scanning, especially for heavy ions. Nevertheless, the computation of this second pencil beam induces longer computation times, which is to be confronted to its practical benefit for dose accuracy.

2.5. Beam Spread and Particle Interactions

2.5.1. Background

The beamlet spread of proton and ion is induced by two types of interactions: Coulomb interactions and nuclear interactions. In general, most of the deflections are small and insignificant, but their high frequency and cumulative effects lead to a beamlet spread, which is often very important and cannot be ignored by the dose calculation algorithms. This beamlet spread depends on both incident particle intrinsic parameters (energy, mass and charge) and media properties. Particles go through different types of media along their pathway from the cyclotron to their rest position: air, beam line devices and patient. It is then important to assess in an accurate way the beamlet spread induced by these different media. This section focuses on the presentation of the different methods implemented in commercial TPS computing an acceptable estimation of the beam spread function $\sigma(z)$ in Equation 2-4. The most accurate models are often the most complex and most time consuming for computations. Unfortunately, as time is a critical constraint in clinics, less accurate approximations based on few parameters are often implemented in the TPS algorithms.

The energy loss of incident particles, developed in section 1.2.2.1 is not the only effect of the elastic, inelastic and non-elastic interactions of particles with matter. Due to Newton’s equations, as the medium electrons and nucleons are not aligned on the incident particles pathways (and also due to nuclear interaction processes), a lateral impulse is transmitted to the incident particles, deviating their trajectory from the beamlet axis. These random interactions occurring along the particle pathway result in an angular broadening of the pencil beamlet. This deflection depends on the mass and charge of the incident particle and on physical properties of the medium. In section 1.2.2, the different interactions types are described, including the fact that small angular scattering is much more likely than large angle scattering. Nevertheless the total beamlet spread is constituted of a combination of these different interaction types, including the dosimetric consequences of the secondary particle emissions.

In a semi-infinite homogeneous media, due to symmetry considerations, the beam spread is a symmetric distribution centered on the beam axis, isotropic in any plan perpendicular to the beamlet axis, and always increasing with depth. Many scientific publications are dedicated to beam spread models in different materials [45] [70] [99], most of them based on physical measurements or MC simulations. It was demonstrated that the lateral dose distribution induced by proton beamlets is generally Gaussian-shaped (or double Gaussian-shaped) as a first approximation in common materials and compounds.

The theory of charged particles interactions is very accurate but unfortunately too complex and not suitable for a direct implementation in a quick PBA approach and several approximations were developed with fewer parameters [45]. The next paragraphs deal with the first beam spread theory and its simplifications and approximations developed during the following years:

- Introduction to the scattering power and the Fermi-Eyges transport equations
- The Molière's scatter theory
- The Highland's and Gottschalk's simplifications
- Recent Models

2.5.2. Introduction to the scattering power and the Fermi-Eyges transport equations [99]

The energy lost by particles in an infinitesimally thin slab of a stopping medium was defined by the introduction of the stopping power quantity in Equation 1-2. The definition of the *scattering power* is similar to the stopping power expression, as it represents the increase of the scattering characteristic angle in an infinitesimally thin slab of a scattering medium du along the beamlet axis:

$$T(u) = \frac{d\big(\theta^2(u)\big)}{du}$$

Equation 2-6

The scattering power is a local variable of the scattering medium and depends on the incident particle energy and mass, and the atomic properties of the medium (in section 2.5.5 are proposed different models describing the scattering power T).

It is easy to define the lateral beamlet spread $\sigma^2(z)$, from from the definition of T (Equation 2-6). Let's consider the effect of a material slab du of scattering power $T(u)$ introduced at depth u in a beamlet of characteristic scattering angle θ (see Figure 2-5). Assuming a circular symmetry of the pencil beam divergence along the z axis, the characteristic scattering angle θ and the lateral beam spread σ can be written exclusively as components in the perpendicular plane (xOy):

$$\theta^2(z) = {\theta_x}^2(z) + {\theta_y}^2(z) \; and \; \sigma^2(z) = {\sigma_x}^2(z) + {\sigma_y}^2(z)$$

And by symmetry:

$${\theta_x}^2(z) = {\theta_y}^2(z) = \tfrac{1}{2}\theta^2(z) \; and \; {\sigma_x}^2(z) = {\sigma_y}^2(z) = \tfrac{1}{2}\sigma^2(z)$$

By using Equation 2-6, the differential expression of the square characteristic scattering angle ${\theta_x}^2(z)$ is:

$$d\left({\theta_x}^2(u)\right) = \frac{1}{2}d\big(\theta^2(u)\big) = \frac{1}{2}T(u)du$$

With an identical expression for ${\theta_y}^2(z)$, the general expression of the characteristic scattering angle θ is:

$$\theta(z) = \sqrt{\theta^2(0) + \int_0^z T(u)du}$$

Figure 2-5

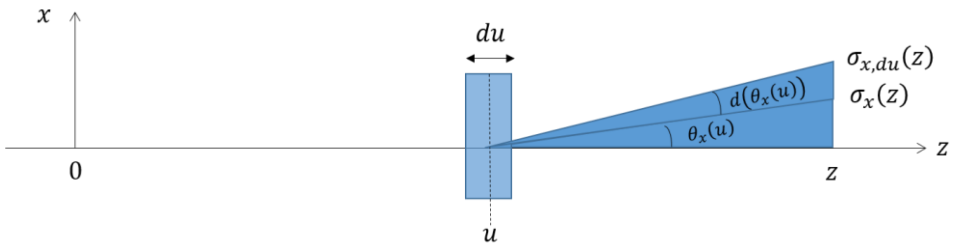

1D representation of the lateral beamlet spread increase due to an infinitesimally thin scattering slab du introduced in the beam line at depth u.

If the beam spread is null at the entrance in the media ($z = 0$),

$$\theta(z) = \sqrt{\int_0^z T(u)du} .$$

Let's now express the beam spread as a function of the scattering power. With the approximation of the small angles, according to Figure 2-5:

$$\sigma_{x,du}(z) = \sigma_x(z) + (z-u) \times \tan d\big(\theta_x(u)\big) \approx \sigma_x(z) + (z-u) \times d\big(\theta_x(u)\big)$$

The differential expression of the square of the beam spread on x, ${\sigma_x}^2$, at depth z is then:

$$d\big({\sigma_x}^2(z)\big) = {\sigma_{x,du}}^2(z) - {\sigma_x}^2(z)$$

$$= {\sigma_x}^2(z) + 2\sigma_x(z)(z-u) \times d\big(\theta_x(u)\big) + (z-u)^2 \times \Big(d\big(\theta_x(u)\big)\Big)^2 - {\sigma_x}^2(z)$$

$$= 2\sigma_x(z)(z-u) \times d\big(\theta_x(u)\big) + (z-u)^2 \times \Big(d\big(\theta_x(u)\big)\Big)^2$$

By eliminating the differential term of the second order:

$$d\big({\sigma_x}^2(z)\big) = 2\sigma_x(z)(z-u) \times d\big(\theta_x(u)\big)$$

Then, using the geometric definition of the characteristic scattering angle and Figure 2-5:

$$\sigma_x(z) = \theta_x(u) \times (z-u)$$

and

$$d\left({\theta_x}^2(u)\right) = 2\theta_x(u)d\big(\theta_x(u)\big)$$

The final differential expression of $d\big({\sigma_x}^2(z)\big)$ is then:

$$d\big({\sigma_x}^2(z)\big) = (z-u)^2 d\left({\theta_x}^2(u)\right)$$

By using Equation 2-6,

$$d\big({\sigma_x}^2(z)\big) = \frac{1}{2}(z-u)^2 \times T(u)du$$

By symmetry, $d\left({\sigma_y}^2(z)\right) = d\big({\sigma_x}^2(z)\big)$ and:

$$d\left(\sigma^2(z)\right) = (z-u)^2 \times T(u)du$$

The global expression of the beam spread for any material is then:

$$\sigma^2(z) = \sigma^2(0) + \int_0^z (z-u)^2 T(u)du$$

Equation 2-7

If $\sigma^2(0)$ is a non-zero value, this means that lateral scattering occurred downward in the beam line devices. The scattering into a medium (heterogeneous or homogeneous) starting at $z = 0$ induces then the following beam spread at depth z:

$$\sigma(z) = \sqrt{\int_0^z (z-u)^2 T(u)du}$$

This general expression of the beam spread accounts for any heterogeneity in the medium, as the scattering power and its position respected to the depth of interest z are evaluated at each step du along the pencil beam axis. As the integrated term is positive, the beam spread always increases with depth as seen on Figure 2-6, whatever the energy of the particles or the composition of the scattering material. Physically, the term $(z-u)^2$ means that the effects of the scattering power of a material are not local but contribute to the beam spread at every depth in the downward region. This is very important for heterogeneous media because the beamlet spread expression contains two kinds of information about the pathway history: the position of each material crossed by $(z-u)^2$ and its composition by T.

Figure 2-6

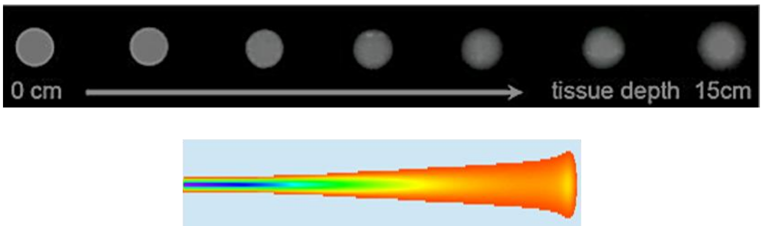

Top: Lateral scattering of 200 MeV protons in water, showing the beam spread effects blurring the perfect circular shape of the incident collimated beam [103]. Bottom: a 100 MeV proton beamlet dose kernel computed in a water phantom by the Plastimatch DCE (see section 3.3.A.1).

The $\sigma(z)$ function is the easier parameter to be defined from experimental data: a simple lateral measurement of the lateral dose induced by proton beamlets provides its width. From these measurements, it is possible to assess the characteristic scattering angle θ by using the relation $\sigma(z) = \theta \times z$, z being the depth in the medium. The scattering power $T(z)$ is more difficult to evaluate, as it is the derivative function of the characteristic angle, and needs complete information about different characteristic angles measured at different depths in the medium.

Gottschalk [46] reviewed six different models for analytic, semi-empirical or empirical determinations of the scattering power T, based on materials and compounds intrinsic parameters and approximations (see section 2.5.5). All of these models account for both MCS and single scattering and propose a scattering power definition compatible with the single Gaussian model of the Fermi's transport equations.

2.5.3. The Molière's scatter Theory

The Molière's theory is based on the Gaussian transport equations of the Fermi-Eyges theory. Instead of using a statistical approach based on the Gaussian distribution statistics and scattering powers, Molière developed a complete method describing the scattering due to 2 types of interaction with the nucleus:

- Small scattering (numerous collisions occurring far from the nucleus and screened by the electrons of the atom, small deflections)
- Large scattering (very rare, close interaction to the nucleus, large deflections)

Molière separated these scattering expressions by the introduction of two characteristic angles:

- X_a, the screening angle, representing the interactions due to small scattering
- X_c, the characteristic single scattering angle due to large scattering.

The analytic expression of these two scattering angles were calculated by Molière [41] [42]:

$$X_c{}^2 = 4\pi N_A(\alpha\hbar c)^2 \frac{Z^2}{A}\frac{\rho z}{(pv)^2}$$

and

$$X_a{}^2 = \left(1.13 + 3.76\left(\frac{zZ}{137\beta}\right)^2\right) \times \left(\frac{\hbar \times Z^{1/3}}{0.468 \times 10^{-8}\,(cm)\ \times p}\right)^2$$

with z the depth in the medium, N_A the Avogadro's number, α the fine structure constant, $\hbar$ the reduced Planck constant, Z the atomic number of the scattering medium, A the atomic mass of the scattering medium, ρ the density of the scattering medium, p and v respectively the momentum and the velocity of the particles and β the ratio between v and c, c being the speed of light.

Finally, from numerical expressions computed by himself, Molière propose the final equation for the total characteristic angle θ_M for a thin target in the particle therapy energy range:

$$\theta_M = X_c\sqrt{1.153 + 2.583 \times log_{10}\left(\frac{X_c{}^2}{X_a{}^2}\right)}$$

This equation could look quite simple, but it is not: the X_c and X_a are quite difficult to assess for a particular medium. Moreover, these parameters vary when the energy of the particles decreases with depth or if the media is heterogeneous. This formula is then correct only for a thin homogeneous target and more complex considerations need to be performed to provide a final estimation of the characteristic scattering angle in real conditions. Scott [104] developed a general expression based on the Molière's approach, accounting for energy loss in the medium and heterogeneities, but is also mathematically too complex for an easy computation in PBA.

Hanson [105] adapted the Molière's equations to the single Gaussian beam spread approximation and proposed the single characteristic angle θ_H:

$$\theta_H = \theta_M \sqrt{1 - \frac{1.2}{1.153 + 2.583 \times log_{10}\left(\frac{{X_c}^2}{{X_a}^2}\right)}}$$

Here again this expression is still too complex for a straightforward implementation in a fast dose calculation PBA as θ_M, X_c and X_a needs anyway to be calculated. Nevertheless, the accuracy of the Hanson approximation, was estimated to be in the range of 2% [46].

2.5.4. The Highland's and Gottschalk's simplifications

Highland used mathematical simplifications of analytic functions, and provided a fast and accurate equation representing the characteristic scattering angle in thin slabs, adapted to the single Gaussian model. This equation depends only on few parameters: the density ρ of the scattering medium, the depth z in the medium, the initial momentum p_1 and velocity v_1 of the incident particles, and the radiation length of the medium X_0:

$$\theta_{HL,thin} = \frac{14.1}{p_1 v_1}\sqrt{\frac{\rho z}{X_0}}\left(1 + \frac{1}{9} log_{10}\frac{\rho z}{X_0}\right)$$

The radiation length depends on intrinsic parameters of the medium and look-up tables are easily found in the literature [106]. Gottschalk [46] derived the characteristic scattering angle approximation proposed by Highland, and integrated it on semi-infinite materials:

$$\theta_{HL,thick}(z) = 14.1\left(1 + \frac{1}{9} log_{10}\frac{\rho z}{X_0}\right)\sqrt{\int_0^z \left(\frac{1}{(pv)(u)}\right)^2 \frac{\rho}{X_0} du}$$

Equation 2-8

with $p(u)$ and $v(u)$ the momentum and the velocity of the particles in the element du. Lynch and Dahl [107] also simplified the Highland formula (Equation 2-8) using approximations and provided two analogous expressions: the first one independent to the atomic number of the medium and the second independent to the radiation length.

Figure 2-7 reports the values of characteristic angles experimentally measured and computed by the Highland/Gottschalk model for 158.6 MeV protons in different materials.

Figure 2-7

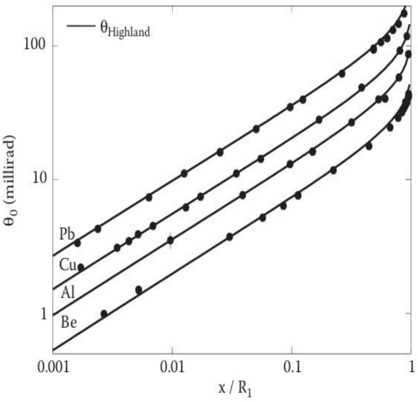

Characteristic scattering angle in different media of a 158.6 MeV proton beamlet in different materials according to the depth x in the medium. The points represent the experimental data and the plain line the Highland/Gottschalk model [108]. R_1 *is the range of the particles in the medium.*

The Highland/Gottschalk was tested by different groups in homogeneous media and its accuracy was estimated to be about 10% [95] [35]. This model is valid for any homogeneous material in the range of the particle therapy energies and is commonly used by PBA dose calculation engines. The lateral scattering occurs also in air before the beamlet reaches the patient (air gap ≈ 10-50 cm) but is insignificant for high energy protons. For low energy protons instead, this beam broadening can be critical in the case of thin beamlets driven by active scanning systems [109].

The XiO TPS from Elekta is based on the Hong algorithm [70] which easily computes the characteristic scattering angles from the Highland/Gottschalk formula. In heterogeneous conditions, the Highland approximation can lead to significant errors, especially in the presence of air gaps or high density materials (see section 4.B.1.2). The method proposed in section 3.3.B.4 deals with this problem and provides a general expression of characteristic scattering angles in any heterogeneous material in the range of energies of common particle therapy treatments.

2.5.5. Other recent models

Six models for the expression of the scattering power T were published in the literature [46]. Some of the following definitions are based on material radiation length X_0, other models rely on intrinsic parameters of the medium like the atomic number Z or introduce a new variable X_s, the scattering length. Complex numerical fits are also proposed, with the depth or the particle velocity as input parameters. Some definitions are more straightforward than others according to the context of the algorithms to be implemented.

- Fermi-Rossi [110]:

$$T_1 = \left(\frac{15.0\,MeV}{pv}\right)^2 \frac{1}{X_0}$$

- ICRU report [111]:

$$T_2 = \left(\frac{15.0\ MeV}{pv}\right)^2 \frac{1}{X_s}$$

  with X_s the scattering length defined as:

$$\frac{1}{X_s} = \alpha N {r_e}^2 \frac{Z^2}{A}\left[2\,log\left(33219(AZ)^{-1/3}\right) - 1\right]$$

  with r_e the classical electron radius.

- The linear displacement from Kanematsu-1 [112]:

$$T_3 = 10^{-3}\frac{X_{0,W}}{X_{0,M}}\frac{1}{R_W - \frac{S_M}{S_W}x}$$

  with $X_{0,W}$ the radiation length of water, $X_{0,M}$ the radiation length of the material, R_W the range of the incident particles in water and S_M/S_W the stopping power ratio of the material.

- Overas-Schneider [113]:

$$T_4 = \left(\frac{19.9\ MeV}{p_1 v_1}\right)^2 \frac{1}{X_0} \times (1-t)^{-(1+k)}\left[C_0 + C_1\left(t - \frac{1}{2}\right)^4 + \frac{4C_1}{k}\left(t - \frac{1}{2}\right)^3 (1-t)(1-(1-t)^k)\right]$$

  with $t = \frac{x}{R}$, R being the range of the particles,

$$C_0 = (201/200) - \left(\frac{23}{5000}\right)\rho X_0$$

$$and\, C_1 = -(11/2) - \left(\frac{43}{1000}\right)\rho X_0$$

- Kanemastu-2 [114]:

$$T_5 = \left(\frac{15.0\ MeV}{pv}\right)^2 \frac{1}{X_0} \times 0.970 \times \left(1 + \frac{ln\, l\,(x)}{20.7}\right)\left(1 + \frac{ln\, l(x)}{22.7}\right)$$

$$with\, l(x) = \int_0^x \frac{du}{X_0(u)}$$

- Improved non – local formula [46]:

$$T_6 = f(pv, p_1 v_1) \times \left(\frac{E_s}{pv}\right)^2 \frac{1}{X_S}$$

  where:

$$f(pv, p_1v_1) = 0.5244 + 0.1975\, log\left(1 - \left(\frac{pv}{p_1v_1}\right)^2\right) + 0.2320\, log(pv) \\ - 0.0098\, log(pv)\, log\left(1 - \left(\frac{pv}{p_1v_1}\right)^2\right)$$

The corrective function $f(pv, p_1v_1)$ is introduced in order to account for single and plural scattering and not only MCS as T_1 and T_2 do.

The description of these scattering powers all depend directly or indirectly on a non-local variable, responsible of an increase of the beam spread: T_1, T_2, T_5 and T_6 summon the inverse of the particle momentum, T_3, T_4 and T_5 the depth in the medium (T_5 being the only definition with the two dependencies). For all these definitions, at the end of the pathway $pv = 0$ or $x = R$ create a singularity in the definition of the scattering power and is not defined beyond. This is quite logical: when the particle is still, its trajectory doesn't define anymore an angle with respect to the beam axis.

These models provide comparable results in water and water equivalent materials. They are also satisfying approximations for the description of a multi-slab geometry in the particle therapy energy range [46]. Gottschalk demonstrated that the differential expression T_6 leads to better results than algorithms implemented in commercial TPS based on the Highland model (Equation 2-8) [46] [70] [101]. It is still not clear which scattering power definition is the most accurate model, as the accuracy of each model varies with the explored parameter ranges and also depends on the accuracy of the medium parameters (radiation length, scattering length and stopping power).

2.5.6. A short review of nuclear interactions

The Coulomb interactions described in section 1.2.2 are not the only type of interactions occurring in media. Interactions involving the strong nuclear force also occur, from transfer reactions at low energy to fragmentation processes at energies higher than 1GeV/u. Protons interact at a rate of 1.2% g^{-1} cm^2 by nuclear interactions [115]. If the incident particle remains at rest after the interaction, meaning that most of its energy was transferred to the secondary particle, this latter can act like the primary particle and even induce other nuclear reactions. This kind of interaction can produce secondary particles that deliver dose deeper than the Bragg peak depth, especially when heavy ions transfer most of their energy to a lighter particle with a low charge (see Figure 1-11).

As explained in section 1.2.2, charged particles are interesting for dose conformation due to their particular depth dose distribution that allows the sparing of healthy tissues around the target volume. Some secondary particles, such as neutrons, exit completely from the target (or even from the patient) and energy is lost locally. Secondary particles are also created by nuclear interactions in the beam line devices, but their scattering angles being generally large, many do not reach the patient. Nevertheless the activation products created by nuclear interactions in the beam line devices, patient or more generally in the treatment room have to be considered for radiation protection.

The nuclear interactions produce an undesirable consequence as they release dose downward the target volume. For heavy ions, the ratio of the dose released in the tail compared to the dose released to the Bragg peak is about 20%. Moreover, as explained in section 1.3, even if the physical dose released by neutrons seems negligible, due to their high RBE their radiobiologic effects on surrounding tissues are significant. Table 2-1 reports the average energy distribution divided on the secondary particles for incident 150 MeV protons.

Table 2-1

Particles	Fraction of the initial energy carried by secondary particles
protons	57.0%
Deuteron	1.6%
Triton	0.2%
^{3}He	0.2%
α	2.9%
Nucleus (recoil)	1.6%
Neutrons	20.0%
Photons	16.5%

Average energy distribution between the different secondary species produced by nuclear interactions induced by an incident 150 MeV proton [116].

It is commonly accepted that the effects of nuclear interactions are small for protons and involve target fragmentation only. For a passive scattering beam line, it is possible to account for them by implementing an experimental depth dose curve in the PBA model. Other models, especially dedicated to active scanning beam lines, consider the additional dose released by secondary particles [71] [95].

It is impossible to describe both nuclear interactions and Coulomb interactions in a single Gaussian distribution, as the angular deviations of nuclear interactions are much larger. The dose distribution induced by nuclear interactions only is called *nuclear halo* and is often modeled as an independent Gaussian distribution that is added to the primary pencil beam (it is said that it surrounds the primary beamlet) [71]:

$$D(x,y,z) = N(z)\left[(1-w)\frac{1}{2\pi{\sigma_P}^2}e^{-\frac{x^2+y^2}{2{\sigma_P}^2}} + w\frac{1}{2\pi{\sigma_N}^2}e^{-\frac{x^2+y^2}{2{\sigma_N}^2}}\right]$$

with $N(z)$ a normalization dose factor on the axis, w the relative weight of the nuclear halo and σ_N the SDPBP due to nuclear interactions.

Usually, for passive scattering beam lines or to reduce by half the computation time, the second Gaussian is neglected ($w = 0$). For active scanning beam lines, Pedroni showed that not considering nuclear interactions can lead to errors in the order of 10% in proton dose calculations [71]. For heavy ions, nuclear interactions represent a high percentage of the total delivered dose, and this double Gaussian model is indispensable. Some more complex models describing the dose halo distribution are also proposed, like the Rutherford hyperbola [100]:

$$D(x,y,z) = N(z)\left[(1-w)\frac{1}{2\pi{\sigma_P}^2}e^{-\frac{x^2+y^2}{2{\sigma_P}^2}} + w\frac{b}{\pi}\frac{1}{(x^2+y^2+b)^2}\right]$$

with b a screening parameter.

For both models (and many others not quoted in this report), the determination of w, σ_N or b is experimentally based on lateral dose profiles measured on MC simulations in water [95].

2.6. Review of the most important and recent developments in proton PBA and models of proton beam spread

This publication list is summarized from the original articles quoted in this report and from the review published by Chapman [95]. Only the most relevant studies are mentioned in the following list. The reader is invited to consult the Chapman's review about proton PBA for more details.

- Russell - 1995 [90]: In this publication a new method considers both MCS and single scattering effects (based on the Eyges-Fermi theory [99] and on the Molière theory [41] [42]) and demonstrates excellent results on the estimation of SDPBP in water. This model, based on the scaling of pre-computed dose distributions, takes theoretically into consideration eventual heterogeneities, but no measurements in such condition was provided in the publication.
- Hong – 1996 [70]: This study proposes a complete model of a passive scattering beam line for protons, considering the scattering that occurs in the beam-modifier and beam-limiting devices, and in the patient. This work is based on the Highland model of the beamlet spread due to MCS [43] [44]. The SDPBP of each element of the beam line is added in quadrature (see Chapter 3 for a more detailed description). Even if this study only deals with homogeneous media, it is still considered today as a reference for a complete dose calculation method dedicated to passive scattering beam lines. This method is implemented in the XiO commercial TPS from Elekta.
- Deasy – 1998 [93]: In contrast to Russel [90], Deasy didn't use pre-computed and scaled dose distributions but started from the Molière's equations [41] [42]. He proposed to represent any intrinsic parameters of the medium as a function of the WED, and built an accurate model accounting for MCS and single scattering, applicable also in heterogeneous media.
- Schaffner – 1999/2007 [102] [117]: This model is implemented in the Eclipse TPS (Varian) and is dedicated to proton active scanning systems. Like Hong [70], Schaffner computed the beam spread by considering a fluence approach in air gap regions and a scattering approach in the patient. This algorithm is based on double Gaussian fits built on MC dose distributions. In heterogeneous media, the dose distribution models are simply scaled according to the media WED.
- Pedroni – 2005 [71]: Pedroni showed that not accounting for non-elastic nuclear interactions in active scanning beam lines can lead to significant dosimetric inaccuracies (up to 10%). He proposed an empirical double Gaussian PBA based

on experimental data measured on the Paul Scherrer Institute (PSI) beam line. The second Gaussian term represents the nuclear halo.

- Soukup – 2005 [101]: Soukup developed the most powerful algorithm known to account for heterogeneities. The basis of this algorithm are equivalent to the Pedroni's PBA. He used the proton scattering powers of materials along the beamlet axis for computing the beam spread in different materials. He obtained acceptable results in heterogeneities between materials of similar densities (dose errors < 3%). In high density gradient regions, the errors were larger than 3%.
- Kanematsu – 2009 [112] [118]: Kanematsu proposed a generalized differential expression for the characteristic scattering angle in heterogeneous media based on proton scattering powers and intrinsic properties of the media.
- Gottschalk – 2010 [46]: Gottschalk reviewed the different definitions and approximations available for the scattering power definitions in materials, and demonstrated that a correct use of scattering power data can lead to accurate dose calculations (errors < 3%).

The PBA developed in this report is dedicated to passive scattering beam lines (Chapter 3) and takes advantage of the best methods of the publications previously mentioned: it is a hybrid PBA based on the Hong model for the entire beam line model [70], the beamlet spread estimation in heterogeneous media is based on the scattering power approach which was generalized for any material thanks to the differential expression of the characteristic scattering angle proposed by Kanematsu [118].

3. AIMS, MATERIAL AND METHODS

3.1 Introduction and general aim of the project

During the last decades an important effort has been dedicated to the dose calculation in particle therapy, in particular Monte Carlo (MC) simulations and Pencil Beam Algorithms (PBA). Unfortunately, the commercial proton TPSs are still very expensive: from 200,000€ to 1,500,000€ when a license for hadrontherapy is included. The aim of this project is the implementation of a proton TPS software, equivalent to a basic commercial TPS and dedicated to a basic proton passive scattering beam line. In order to help research groups in particle therapy that couldn't afford a real commercial TPS, this TPS is proposed as an open-source, free and multiplatform software devoted to research only. At a dosimetric level, the accuracy of our PBA Dose Computation Engine (DCE) is considered as acceptable if the 3%-3 mm gamma index scores reaches 95% in homogeneous and heterogeneous conditions when compared to MC simulations. Moreover, these results have to be computed in a reasonable computation time (≈5 min) on a common laptop or workstation. Unlike GPU methods (see section 2.2.3) this software should not require any specific hardware.

For the sake of clarity and coherence Chapter 3 (material & methods) and Chapter 4 (Results and Discussion) are divided in three parts A, B and C. The DCE developments in Plastimatch are gathered in parts A & B and the TPS interface implementation and connection to the DCE is presented in part C:

- Part A – *Beam line*: this part deals with the beam line model and the four dose summation algorithms implemented in Plastimatch during this project (Figure 3-1).

Figure 3-1

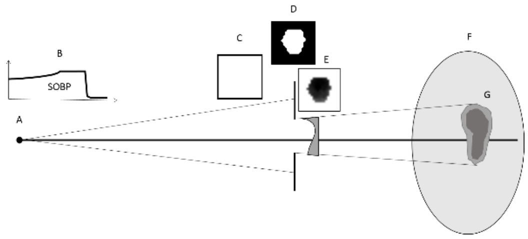

Passive scattering beam line description and implementation: from the source to the dose computation in the patient.

- Part B – *Beam spread corrections*: this part is dedicated to an accurate beam spread model in PMMA range compensators and in heterogeneous media (patients) in Plastimatch (Figure 3-2).

Figure 3-2

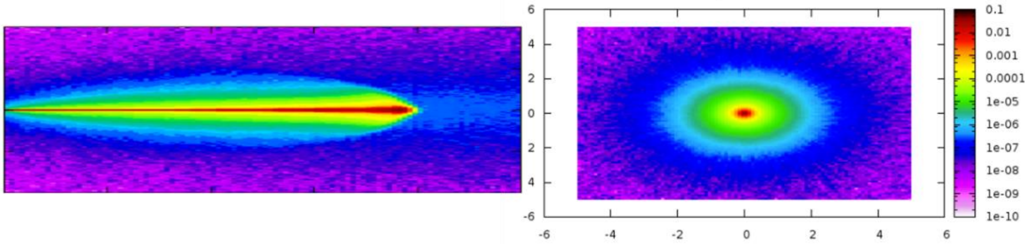

100 MeV proton beamlet dose distribution in water (MC simulation).

- Part C – Software *interface*: this part describes the implementation of the TPS interface in SlicerRt, a toolkit dedicated to radiotherapy in the open-source software 3D Slicer (Figure 3-3).

Figure 3-3

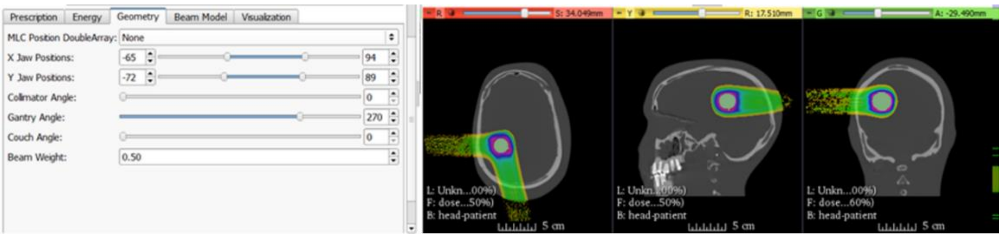

MLC Position DoubleArray: None
X Jaw Positions: -65 94
Y Jaw Positions: -72 89
Collimator Angle: 0
Gantry Angle: 270
Couch Angle: 0
Beam Weight: 0.50

Implementation of the TPS interface in the SlicerRt toolkit.

Each part A, B and C is associated with dedicated Aims, Material & Methods (Chapter 3) and Results/Discussion (Chapter 4) sections.

3.2 Aims

3.2.A Aims – Part A – *Beam line*

In this part we propose to build a complete DCE simulating a basic passively scattered proton beam line. This DCE is built on the Hong model [70], but other faster dose reconstruction algorithms are also implemented and tested. This model considers a source, a range compensator, a collimator and a patient. Practically a passively proton beam line is more complex than this model. The Hong approach deals with that problem by including the effects of the other beam line elements in the source size, the nominal beam energy or in the range compensator definition as a first approximation.

Moreover, tools helping for treatment planning are also implemented, such as the automatic creation of Spread Out Bragg Peaks (SOBP) or an automatic shaping of the collimator, both associated to a target volume. Two options are then available to the user:

- The user builds a treatment plan by setting the beam line parameters (such as the field size, beam angle, beam energy…). This option is called the "*Physics"* modality.
- The user indicates the target volume and the DCE creates automatically a range compensator, a collimator and the optimized energy spectrum (SOBP) to evenly cover the entire target volume (including eventual margins). This option is called the *"Clinics"* modality.

This DCE is not validated for clinical applications, but is dedicated to the research field. It provides the beam line parameters associated to treatments that are theoretically deliverable to a patient based on the calibrated Bragg peak weights (or exposure time), the 2D map of the beam aperture and the 2D map of the range compensator widths.

3.2.B Aims – Part B – Beam spread corrections

The reference proton dose calculation algorithm implemented in the XiO TPS is the Hong algorithm [70], based on the Highland approach in homogeneous media (see section 2.5.4). It is demonstrated (section 4.A.1.7) that this approach is not sufficient for a correct computation of the beamlet spread in heterogeneous media, especially in high density materials or in presence of air gaps. Moreover, the Hong's model for the computation of beamlet spreads induced by a PMMA range compensator are underestimated when compared with MC simulations. In this part, we propose two models based on MC simulations: the first one accounting in an accurate way for heterogeneities in the patient, the second modeling pencil beamlet spreads in air due to the presence of a PMMA range compensator in the beam line. Coupled with performing dose reconstruction algorithms (Part A), the dose distributions computed by the DCE implemented in this project are expected to be accurate in any real condition (homogeneous phantoms or heterogeneous patients).

3.2.C Aims – Part C – Software interface

Part C proposes the implementation of an interface helping the user during the setting of the treatment plan parameters directly from the 3D Slicer software. The interface also proposes to represent the associated geometrical shape of the created beams on the 3D CT-images before the dose computation. Once the input parameters are correctly set by the user in the interface, the DCE computes the 3D dose distribution associated to the specific input parameters. Finally the output 3D dose distribution can be overlain onto the input CT-images to help the user with the dosimetric validation of the treatment plan.

3.3 Materials and Methods

3.3.A Materials and Methods – Part A – *Beam line*

This study is focused on the implementation of a basic passively scattered beam line based on the well-known Hong's approach [70] for proton dose calculation in patients. In this method, the beam line is decomposed in different beam-modifier and beam-limiting devices (see Figure 3-4):

- The source: effects of the source size are accounted in the dose distribution computation. The source size is also used to model beam spread due to beam line elements located upward the range compensator and aperture.
- The energy spectrum: the energy of the incident protons can be set and Spread Out Bragg Peaks (SOBP) can also be created.
- The collimator (beam-limiting device). A collimator is introduced in the beam line to block the area of the beam not directed toward the target volume irradiating the surrounding healthy tissues.
- The range compensator (beam-modifier device). Different thicknesses of PMMA are added in the beam line to compensate for the shape of the target volume and make the dose distribution conforms to the distal surface of the target volume. The longitudinal and lateral deformations of the beamlets going through the range compensator are considered.
- The patient: the patient also contributes to the beamlet shape as the protons reach the target volume.

The details of this method describing the source, range compensator and patient effects on the proton beamlets are described in the next paragraphs.

Figure 3-4

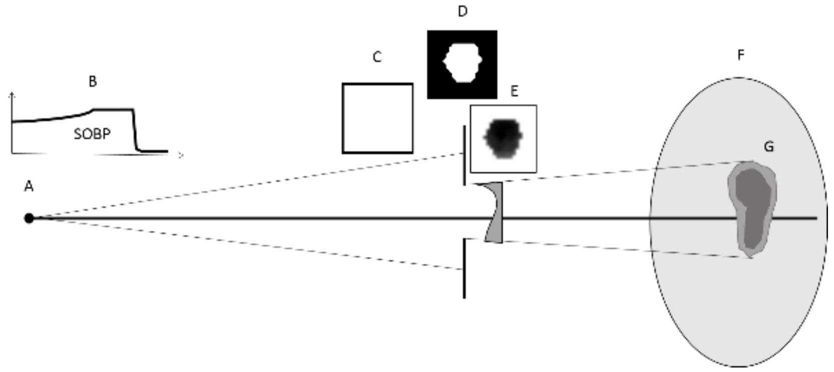

Representation of a basic passive scattering beam line and its elements: A – the source, B – the SOBP, C – the homogeneous field, D – the collimator, E – the range compensator, F – the patient, G – the target volume.

According to the Hong model, the beam spread in the input image volume (patient or phantom CT-images) is modeled by a single Gaussian, corresponding to the definition of Equation 2-4. The Standard Deviation of the Pencil Beam Profile (SDPBP, or σ) is decomposed into 3 simpler terms, added in quadrature (see Equation 3-1): the SDPBP of the source size, the SDPBP due to MCS in the range compensator and the SDPBP due to MCS in the patient:

$$\sigma^2(z) = {\sigma_{src}}^2(z) + {\sigma_{rc}}^2(z) + {\sigma_{pt}}^2(z)$$

Equation 3-1

This expression of the quadrative sum of the SDPBPs from each of the beam elements is a direct consequence of the Equation 2-7. The analytic and semi-empirical definitions of σ_{src}, σ_{rc} and σ_{pt} are respectively discussed in sections 3.3.A.3, 3.3.A.5 and 3.3.A.6.

Hong proposed also a dose summation method to calculate the total dose released to the patient by adding the contribution of every pencil beam in the beam frame plan. This method was directly applied in our TPS. In addition to the Hong's dose summation method (section 3.3.A.9-d), three other methods are also proposed: the ray tracer (RT-section 3.3.A.9-a), the Cartesian Geometry dose Summation (CGS – section 3.3.A.9-b) and the Divergent Geometry dose Summation (DGS – section 3.3.A.9-c). Moreover, some additional and automatic tools were implemented: a SOBP designer, a range compensator creator and a collimator shaper.

3.3.A.1 Plastimatch environment

The dose calculation algorithms described in Part A were implemented in the open-source software Plastimatch [119]. This multiplatform software primarily proposes a selection of image computing tools (especially for volumetric image registration [120]) dedicated to research. Plastimatch is coded in C++ and regularly updated with new algorithms. It is proposed as a Berkeley Software Distribution (BSD)-style license, allowing modifications and redistribution. The entire proton beam line and the dose computation algorithms are exclusively developed in the Plastimatch environment as a new tool for proton dosimetry based on Computed Tomography (CT)-images.

3.3.A.2 The ray tracer as a geometric tool

In order to describe the pencil beamlet geometry, a ray tracer algorithm is used to assess the properties of the medium along each pencil beam axis. This algorithm is called the *ray tracer tool*. This tool samples the different properties of a medium at different depths along its axis, according to regular steps fixed by the user (Figure 3-5).

Figure 3-5

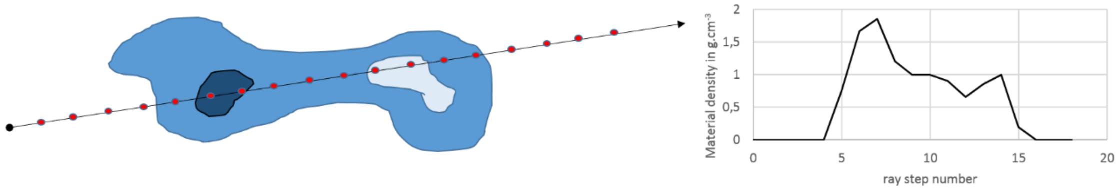

Left: the ray tracer tool crossing a CT image. Right: example of the density values returned by the ray tracer tool along the ray trajectory shown on the left picture.

The advantage of this method lies in the possibility of sampling any kind of material property along the pencil beam axis, even accumulated properties like the WED. The ray tracer intervenes each time a pencil beam central-axis term or off-axis term is computed.

3.3.A.3 The source size

The Hong method accounts for the source SDPBP based on a projection of its spread at the depth of interest z from the source size normalized at the aperture. This definition has sense due to the Thales' theorem, as seen on Figure 3-6.

Based on Figure 3-6, the expression of the source SDPBP is then:

$$\sigma_{src}(z) = \sigma_{src,collimator} \times \left(\frac{z - z_{collimator}}{z_{collimator}}\right)$$

Equation 3-2

with $\sigma_{src,collimator}$ the projection of the source SDPBP at the collimator depth $z_{collimator}$. Experimentally, the projection of the source SDPBP in the collimator frame is determined by the help of lateral dose profiles in air [70]. The analysis of the penumbra width in small or broad beam conditions allows an accurate determination of $\sigma_{src,collimator}$ as seen in section 3.3.A.3, where a concrete estimation of this parameter is extracted from measurements based on the Massachusetts General Hospital's (MGH) proton beam line.

Figure 3-6

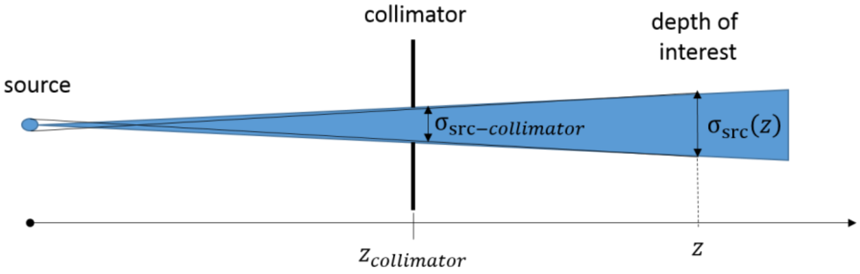

Determination of the source SDPBP at depth z due to the source size from the source SDPBP at the collimator depth.

3.3.A.4 The beam frame and collimator

The beam is decomposed as a 2D matrix defined in the aperture frame, located at a well-defined distance (called *offset*) from the source set by the user. This beam frame (or field size) is characterized from the position of the first pixel of the matrix, the pixel numbers (*resolution*) and pixel spacing size (*spacing*) as shown on Figure 3-7. The beam axis is defined from the positions of the source and isocenter of the beam. The parameters introduced in this paragraph need to be defined before the DCE is called for dose computation.

Figure 3-7

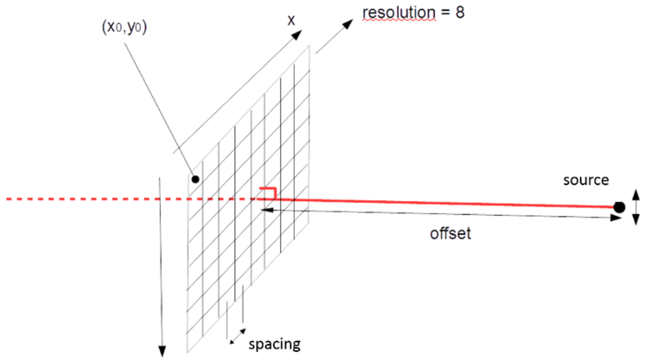

Definition of the beam frame at the aperture distance (offset). The beam frame is defined as a 2D matrix from the position of the first pixel (x_0, y_0), the matrix resolutions and the pixel spacing.

The collimator is a beam-limiting tool that is introduced in the aperture plan and can be automatically created to conform a target volume or uploaded in the algorithm from a file. The automatic creation of the collimator uses the ray tracer tool (see section 3.3.A.2). Each beamlet of the beam frame is tested: if it crosses the target volume then the associated pixel of the collimator receives the 1 value. If it doesn't cross the target volume, it gets the 0 value.

Even the most external boundaries of the target volume must receive 100% of the dose prescription, but with this method they would receive only half of the dose, due to the lack of lateral scattering. In order to account for this fact, a geometric smearing is applied (chosen by the user) to enlarge the collimator and compensate for this lack of lateral scattering (Figure 3-8).

The collimator shape matrix is computed automatically and exported as a 2D image, and inversely a 2D map can also be imported into the DCE as a collimator.

Figure 3-8

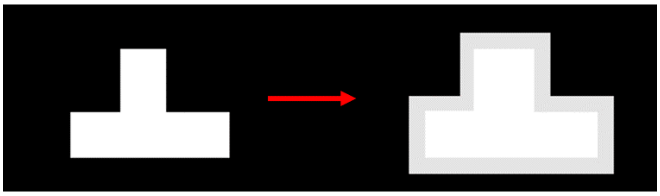

Smearing of the collimator to account for the lack of lateral scattering in the (xOy) *plan. The width of the smearing (grey band) is an input parameter to be defined by the user.*

3.3.A.5 The Range Compensator (RC)

The RC is a PMMA device that is introduced in the beam line to compensate for the differences of WED (heterogeneities or air gaps) crossed by the most energetic beamlets before they reach the distal part of the target volume. The RC induced two important modifications on the beamlets that cross it:

- The central-axis term accounts for the PMMA RC thickness and the length of the beamlets pathway is reduced downward in the patient.
- The Gaussian off-axis term is enlarged as MCS occurs in the RC (single and plural scattering are not considered as they are mainly lost in air between the RC and the patient).

The effects of the introduction of different materials in a beam line were studied in the literature [45] [46] [70], especially for pure elements (like copper or lead). Hong [70] provided a method assessing the beamlet spread induced by a PMMA RC (Figure 3-9) at the point of interest $P(x, y, z)$:

$$\sigma_{rc}(E, l, z) = \theta_0(E) \times \gamma(l/R) \times \left(z + z'_{rc}(l, E)\right)$$

Equation 3-3

with E and R respectively the energy and the range of the incident particles, l the thickness of the RC, z the depth of interest from the RC downward surface, θ_0 the FWHM for the Gaussian angular distribution for protons of energy E in the medium (i.e.

maximal characteristic angle, $l = R$), γ the relative characteristic angle after a range compensator of thickness l/R and z'_{rc} the depth of the scattering effective origin. The functions θ_0, γ and z'_{rc} are given as figures in the Hong publication (Figure 3-10). This beam spread contribution is added by quadrature to the effects of the source size and the scattering in the patient as explain in Equation 3-1.

Figure 3-9

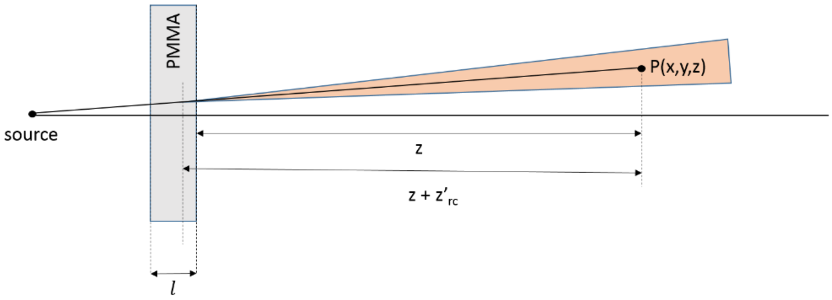

Geometric description of the beam spread at a point of interest $P(x, y, z)$ due to a PMMA RC introduced in the beam line.

Figure 3-10

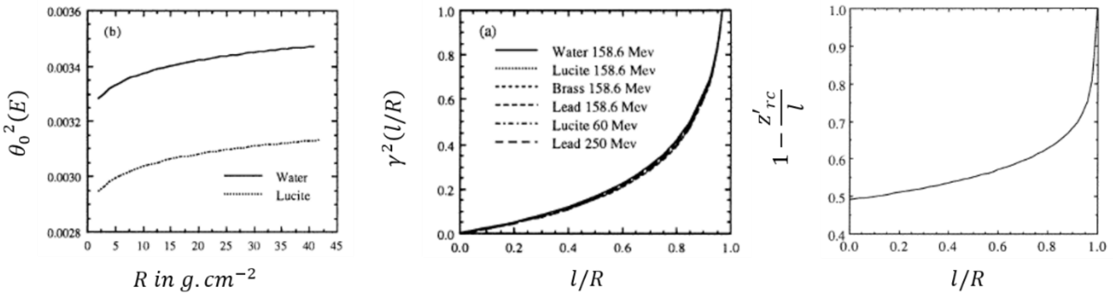

Figures for the definition of the θ_0, γ and z'_{rc} functions from Hong [70].

As explained above, the range compensator is a device that is used to optimize the proton dose distributions by reducing the dose released downward the target volume. For each ray in the beam frame, the WED of the intersection with the most distal face of the target volume (including margins) is calculated. The 2D matrix containing the Lucite Equivalent Depth (LED) is then computed to compensate for the lack of medium and heterogeneities upward the distal limit of the target volume.

A smearing of the PMMA thicknesses is also applied to account for the lateral dose equilibrium at the distal surface depth of the target volume (Figure 3-11). This matrix is associated to the smeared collimator matrix. The range compensator thickness matrix is also exportable as a 2D image, and inversely, a 2D matrix can also be uploaded as range compensator in the DCE.

Figure 3-11

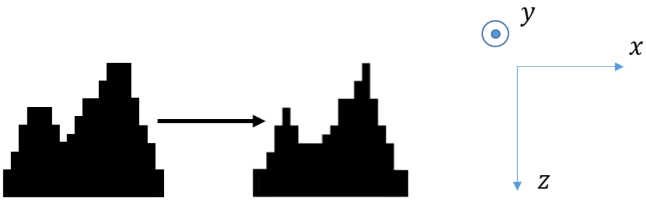

2D representation of the range compensator smearing (before: left, after: right). This process doesn't occur only in the x direction but on the entire plan (xOy) *by convolution. The range compensator thickness is represented on the vertical z axis, the beam going through from up to down.*

3.3.A.6 The patient

As in the range compensator, the particles lose energy and the beamlet spreads due to interactions in the patient.

- The central-axis term accounts for the WED crossed by the pencil beam in the medium (patient).
- Hong described the beamlet spread evolution in the patient by using the single Gaussian Highland approximation (see section 2.5.4) in homogeneous media [70], theoretically from Equation 2-7 and Equation 2-8:

$$\sigma_{pt}(z) = 14.1cm\left(1 + \frac{1}{9}.log_{10}\frac{z}{X_0}\right)\sqrt{\int_0^z \left(\frac{z-x}{(pv)(x)}\right)^2 \frac{dx}{X_0}}$$

Equation 3-4

with z the depth in the medium, X_0 the radiation length of the medium, and p and v respectively the momentum and the velocity of the particles.

Practically, as in the previous paragraph, the beamlet spread in the patient is estimated by look-up figures fitting beamlet lateral profiles in water (Figure 3-12):

$$\sigma_{pt}(z) = \sigma_{0,w}(R) \times \gamma_w(z/R)$$

Equation 3-5

with $\sigma_{0,w}$ the maximum beamlet spread in water for particles of range R and γ_w the relative beam spread at depth z/R, z representing the depth in the patient.

In the patient heterogeneities the beamlet dose distributions are longitudinally scaled according to the WED crossed by the particles. In other words, in Figure 3-12 and Equation 3-5, in the case of heterogeneities, the depth z is replaced by the WED l crossed at depth z, and the expression of the pencil beam spread due to the MCS in heterogeneous media becomes:

$$\sigma_{pt}(z) = \sigma_{0,w}(R) \times \gamma_w(l/R)$$

Figure 3-12

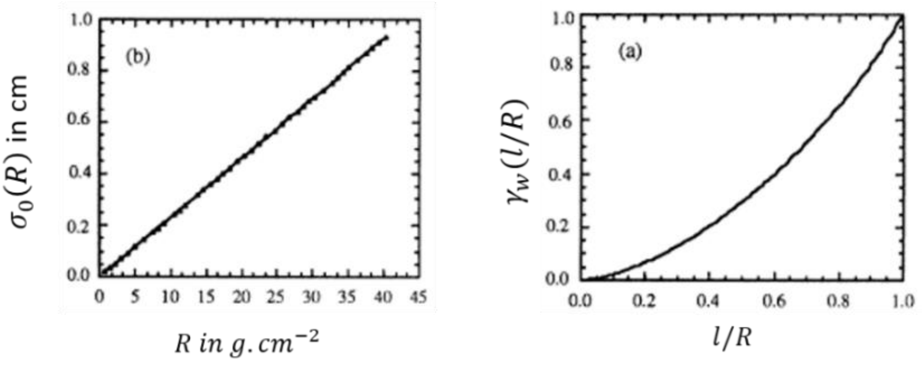

Look-up figures for the definition of the σ_0 *and* γ_w *functions in water [70].*

The WEDs are computed from Equation 2-1. The STopping Power Ratios ($pSTPR_m$) are computed from look-up tables [113] [121] based on the Hounsfield Units (HU) of the medium (see Appendix A2) sampled by the Ray Tracer tool in the input CT-images.

The expression of the beam spread in the patient is the last member of the quadrative sum for the beam spread decomposition defined in Equation 3-1.

3.3.A.7 3D dose distribution released by a proton pencil beamlet

Using the initial definition of the pencil beam dose distribution from Equation 3-1, and the decomposition of the beam spread into 3 SDPBP contributions (section 3.3.A.3, 3.3.A.5, 3.3.A.6), the global 3D dose distribution released by a single pencil beamlet of energy E is:

$$d(x,y,z) = \frac{DD_w\left(l_{RC} + l_{pt}\right)}{2\pi\sigma^2(z)} e^{-\frac{x^2+y^2}{2\sigma^2(z)}}$$

where

$$\sigma^2(z) = \left[\sigma_{src,collimator} \times \left(\frac{z - z_{collimator}}{z_{collimator}}\right)\right]^2$$

$$+ \left[\theta_0(E) \times \gamma\left(\frac{l_{RC}}{R}\right) \times \left(z + z'_{rc}(l_{RC}, E)\right)\right]^2$$

$$+ \left[\sigma_0(R) \times \gamma_w\left(l_{pt}/R\right)\right]^2$$

with l_{RC} the water equivalent length of the PMMA thickness and l_{pt} the WED in the patient. The proton depth dose curves in water DD_w were computed from the Bortfeld analytic method [122] (Figure 3-13).

Figure 3-13

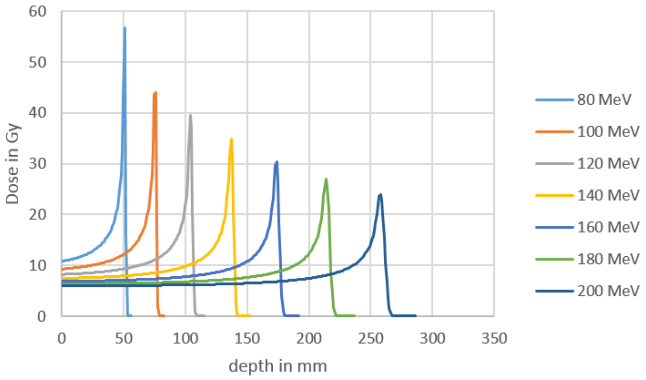

Depth dose profiles (Bragg peaks) computed by the Bortfeld analytic method [122].

3.3.A.8 The Spread Out Bragg Peak (SOBP) creator

As seen in section 1.2.2.1, the dose released by a proton Bragg peak is too thin to cover an entire target volume. A set of weighted mono-energetic Bragg peaks of different energies is used to even the dose on a whole 3D target volume. The SOBP is built as a global property of the beam, while the local heterogeneities of the patient are accounted for by the range compensator defined in section 3.3.A.5. The minimal and maximal energy of the SOBP are respectively determined by the minimum and maximum WED values from all the pencil beamlets within the target volume (margins and RC thickness included).

The weight of each mono-energetic beam is determined by an algorithm that optimizes the evenness of the dose distribution in a depth interval defined by the target volume. Moreover, the algorithm also minimizes the dose around the target volume in order to spare the healthy tissues. The energy resolution (nominal energy difference between two consecutive Bragg peaks) is a parameter set by the user. The global Output Dose Volume (ODV) receives a dose contribution from each weighted mono-energetic sub-beamlet of the SOBP, for each beamlet of the beam.

3.3.A.9 Dose Summation methods

In addition to the Hong’s dose summation method (HGS for Hong Geometry dose Summation), three other algorithms were developed in Plastimatch: the Ray Tracer (RT), the Cartesian Geometry dose Summation (CGS) and the Divergent Geometry dose Summation (DGS). Three of these algorithms (CGS, DGS and HGS) account for the lateral scattering occurring in the medium by computing the off-axis term of the pencil beam model, mathematically defined in Equation 2-4. The beamlet spread is identical for these three algorithms and is considered as a simple Gaussian model, as determined in section 3.3.A. The RT computes only the dose on the central-axis, without beamlet spread.

The next paragraphs describe in details the four algorithms implemented in Plastimatch. Each algorithm computes a 3D dose distribution in an ODV, identical in dimension to the input CT-images volume, but dedicated to receive a dose contribution values.

The dose summation methods were compared with MC simulations (Fluka code – see section 3.3.B.1), considered as the gold standard for dose measurements in homogeneous and especially in heterogeneous media when dose measurements are not easily realizable in the particle therapy field.

a) Algorithm 1 - The Ray Tracer as a dose summation method:

In section 3.3.A.2, the ray tracer tool was used for sampling a numerical value from CT-images (like HU numbers, density or even cumulative quantities like WED). In Plastimatch, the RT is also used as a dose computation method. Each voxel of the ODV is investigated by its position: if the voxel is located outside from the beam frame, the dose received to that voxel is null. If it is located in the beam frame, then the proton WED of the voxel is sampled by the ray tracer tool. The dose received by this voxel is then extracted from the Bortfeld's analytic depth dose curves [122] at a depth corresponding to the WED of the voxel.

Advantages	**Disadvantages**
• Very fast computation time.	• Accurate only in the regions satisfying the lateral dose equilibrium. • Inaccurate near sharp edges. • Doesn't consider any lateral scattering – no penumbra.

b) Cartesian Geometry dose Summation (CGS)

For every pencil beamlet in the beam frame, the 3D dose distribution released around the beamlet axis is followed and summed in the ODV. This means that the computation time is directly proportional to the number of beamlets passing through the beam aperture (aperture resolution). The geometry of the input images is transferred to the beam frame geometry (see Figure 3-14), in which the released dose from each pencil beam is evaluated. The scattered dose is evaluated by Equation 2-5 in every plan perpendicular to the beam axis. Only the voxels located at a distance within 3σ from the pencil beam axis receive a significant dose (Figure 3-15): mathematically, due to the single Gaussian shape of the off-axis term, the dose released to the area farther than 3σ is less than 0.3% and is neglected for computation time optimization. Once the dose is computed in the beam frame geometry, the dose matrix is transferred back to the ODV geometry, by the inverse transformation described in Figure 3-14.

Figure 3-14

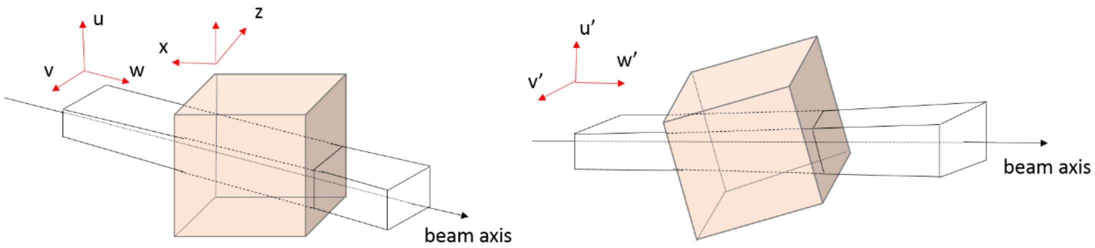

Left: input volume geometry defined in the room reference (x, y, z). Right: beam frame geometry (u, v, w). The geometry of the input volume is transferred in the beam frame geometry, where the 3D dose distribution is calculated. Once the dose computation process is over, the dose matrix is transferred back to the ODV geometry (input image geometry).

Advantages	**Disadvantages**
• Accounts for lateral scattering. • Fast. • The dose calculation considers only the active beamlets.	• The computation time is proportional to the pencil beamlet resolution. • The computation time for a single beamlet increases with σ^2.

Figure 3-15

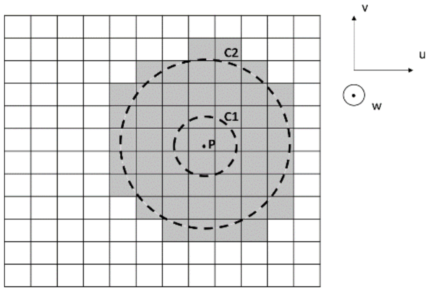

Dose released in the beam frame for a single pencil beamlet. The intersection of the pencil beamlet with the plan occurs in P, the 1σ *area is defined by the C1 circle area and the* 3σ *circle area by the C2 circle area. Only the voxels located in the grey area* (3σ) *receive a dose contribution computed from Equation 2-5. The white voxels are too far from the pencil beamlet central axis to receive a significant scattered dose, the dose delivered in this voxel is considered to be zero.*

c) Divergent Geometry dose Summation (DGS)

This dose summation method is by construction similar to the DGS, but in a completely different geometry: the divergent geometry. This geometry is represented as a 3D parallelepiped matrix (2 dimensions for the beam aperture resolution and the third dimension for the depth along the beam axis). The number of voxels in the 2D cross section corresponds to the pencil beamlet resolution of the beam aperture. In this new geometry, each voxel of the 3D matrix (Figure 3-16 right) contains four different data: the position of this voxel in the initial input geometry (x, y, z) and the dose it contains. The entire dose distribution is then represented as a parallelepiped 3D matrix containing the dose and its associated position in Cartesian coordinates (input geometry). On the contrary to the CGS algorithm, the size of the divergent ODV doesn't depend on the beam divergence or on the depth in the medium. Lateral adequate margins are added to the divergent volume to contain the laterally scattered dose in the area around the active set of beamlets (beam penumbra).

Figure 3-16

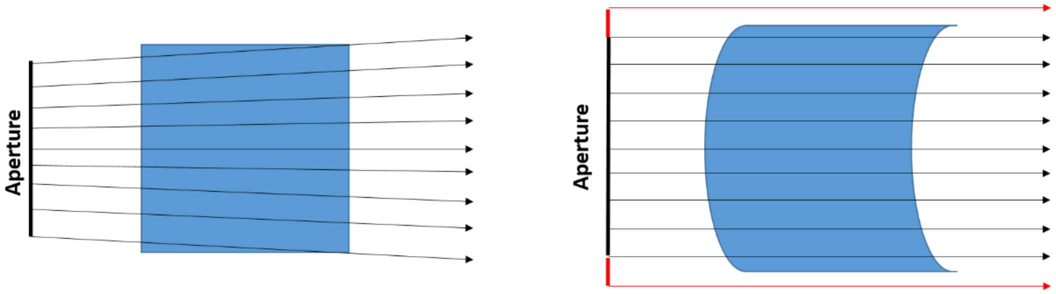

Transformation of the input Cartesian geometry (left) to the divergent geometry (right) following the beam divergence. Each voxel of the divergent geometry contains both the position of the associated voxel in Cartesian coordinates, and the released dose computed by the dose summation algorithm in this voxel. The margins applied to the volume are shown in red.

The dose distribution is computed in the divergent matrix, along each ray. Each voxel receives the scattered dose coming from the pencil beam rays contained in the 3σ radial area around it (Figure 3-17). In each voxel the dose is computed according to Equation 2-5, by considering that the voxels are not evenly distributed in space: w_x and w_y (the associated Cartesian size of the voxels) increase with depth due to the beam divergence. Moreover, the DGS algorithm computes the dose contribution coming from an ellipsoid surface, which was considered as a plan in the CGS algorithm (Figure 3-15). This approximation is acceptable as the divergence is small (small field size compared to the source-aperture distance. Finally, due to the divergent geometry, the spatial dose resolution decreases with depth as the voxel size laterally increases.

Figure 3-17

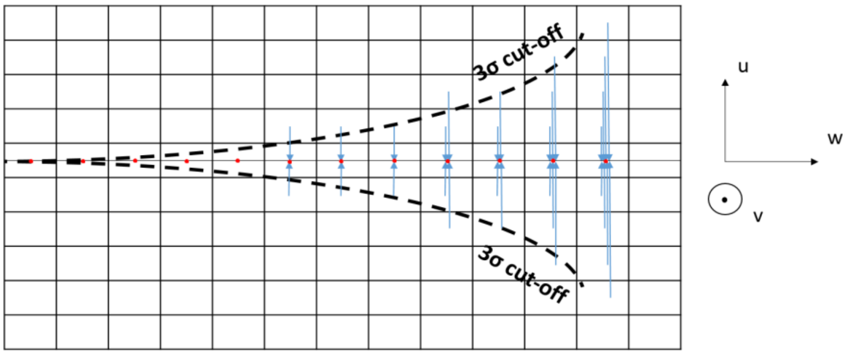

Dose summation in the divergent geometry. Only the dose contributions from pencil beam rays in a 3σ radial area around the voxel of interest are considered during the dose computation. The $(u0v)$ plan represents the beam aperture resolution and the w axis represents the beamlet axis depth.

Once the dose was computed in the divergent geometry volume, the dose volume is transferred back to the initial Cartesian geometry.

Advantages	**Disadvantages**
• Accounts for lateral scattering. • Dose calculation process occurring only inside the active beamlet frame region (and margins).	• The resolution decreases with depth. • Computation time for a single voxel increases with σ^2. • High density materials in the penumbra area create dose artefacts.

d) The Hong algorithm dose Summation Geometry (HGS)

The HGS is described in details in the Hong's publication [70], and is the dose summation algorithm implemented in the XiO TPS. The dose in each voxel of the ODV is computed by summing the scattered dose contributions coming from a 3σ circular radial area (perpendicular to the beam axis) around the voxel. This circular radial area is decomposed into sectors (Figure 3-18). For each voxel, the coordinates of the sectors center are easily calculated in the Cartesian geometry and assumed to be on the plan perpendicular to the beam axis.

Figure 3-18

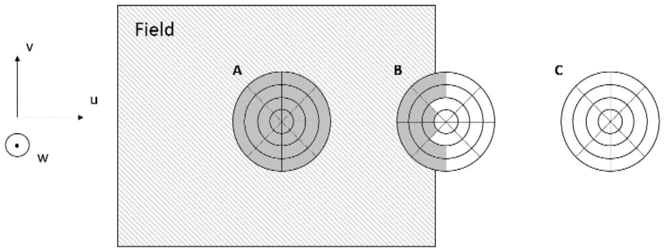

HGS method: the $(u0v)$ represents the beam frame plan, w being the beam axis direction. Case A: the voxel of interest and all sectors are included in the active beam frame, each sector contributes to the global scattered dose at the voxel of interest. Case B: the voxel of interest is near the active field size (beam edge), only some of the sectors contribute to the scattered dose at the voxel of interest. Case C: the voxel of interest and all its sectors are outside from the active beam frame, the dose received at the voxel of interest is zero.

The number of sectors is a parameter set by the user, and is determined by the number of radial and angular sections. Hong's recommend the value of 4x8 sections respectively for the radial and angular sections as shown on Figure 3-18. The dose delivered to each voxel of interest is computed by using the Equation 2-5. The scattered dose coming from each sector is assumed to be even in the whole sector and equal to the dose scattered by the center of the sector. If a sector center is not in the active beam aperture, the scattered dose from this sector is zero (case C of Figure 3-18).

Advantages	Disadvantages
Accounts for lateral scattering. The aperture resolution has almost no incidence on the computation time.	Slow for high resolution volumes. The theoretical beamlet spread (even in the inactive part of the beam frame) is investigated for every voxel of the ODV. High density materials in the penumbra area create dose artefacts.

3.3.A.10 Dose normalization and beam weight

The dose released by a unique pencil beamlet doesn't depend on the field size, or on the aperture resolution. It is intrinsically determined by the Equation 2-5. On the contrary, the final ODV, being the sum of the contributions from all the pencil beamlets, depends on the field size and on the pencil beamlets density (aperture resolution): the higher the pencil beam density, the higher the dose accumulated in the ODV. In order to provide absolute dose computations, the dose is normalized for each beam to a *Reference Dose Point* (RDP) according to each beam weight and the dose prescription. If no RDP is defined in the input parameters list, the isocenter of the beam is set as the RDP by default.

As a concrete example, let's consider a two beams dose calculation, normalized in $P(x_0, y_0, z_0)$ at the dose prescription D_{Norm}. The non-normalized ODV distribution associated to the first and second beams after dose computation are respectively $D_1(x, y, z)$ and $D_2(x, y, z)$.

The respective normalization constants of the non-normalized ODV C_1 and C_2 are defined as:

$$C_1 = \frac{D_{Norm}}{D_1(x_0, y_0, z_0)} \; and \, C_2 = \frac{D_{Norm}}{D_2(x_0, y_0, z_0)}$$

If the beam weights are respectively defined as w_1 and w_2 (usually $w_1 + w_2 = 1$), the total ODV is normalized as following:

$$D_{tot}(x, y, z) = D_{Norm} \times [C_1\, w_1 D_1(x, y, z) + C_2\, w_2 D_2(x, y, z)]$$

3.3.A.11 Executable file and input parameters

The input parameters for the dose computation are defined in an input text file (.txt) with a line associated to each input parameter. The different parameters are listed in the Appendix B of this report and an input file for computing a dose distribution in an input CT-image volume is also proposed as an example.

The input parameters are divided in 3 categories:

- the parameters of the plan (such as the dose prescription, the path of the input CT-images, the path of the output dose volume, etc.)
- the parameters of the beams (such as the source position, the isocenter, the aperture resolution, etc.)

- the Bragg peak definition parameters (such as the energy, the straggling, and the weight of the Bragg peak in a SOBP).

It is recommended to consult the website documentation [119] for an updated definition of the input flags instead of Appendix B (written in 2015), as the Plastimatch source code is regularly updated with new computation possibilities.

The DCE is released in the Plastimatch software, and its executable name is *proton_dose.exe,* which must be associated with the input parameter file as following:

```
../proton_dose.exe input_file.txt
```

3.3.B Materials and Methods – Part B – *Beam spread corrections*

As explained in Part A, the reference dose calculation method is the Hong dose computation algorithm [70]. When the ODV computed by the Hong algorithm were compared to MC simulations, some errors (up to 30% in air gaps and up to 20% in high density heterogeneities, see section 4.B.1.2), were found on beamlet spread estimations, even in very simple geometrical configurations. These errors come from approximations of the beam spread models in beam-modifiers devices introduced in the beam line and from heterogeneities in the patient.

By construction, the beamlet spread due to the source size is supposed to be correctly described, as it is geometrically defined by the user from the experimental data. Moreover, the simulations performed in this part were all realized with a pointed source (source size = 0). This means that the errors in the beam spread estimations come necessarily from the media introduced in the beam line.

As shown in section 3.3.A, the beam spread is decomposed as a quadrative sum of the beam spread from the range compensator and from the MCS in the patient. Two approximations can explain this unsatisfying assessment of the total beam spread:

- The Hong's model for the beam spread induced by the MCS in the range compensator are based on a general model averaged on many materials. It is then globally satisfying on all materials but the model is not exclusively dedicated to PMMA.
- The Highland approximation in heterogeneous materials (by a WED scaling on the longitudinal axis) is unsatisfying.

This study proposes to provide an accurate description of the total beam spread by improving its definition at two different levels:

- σ_{rc}: A study of the broadening of infinitesimal beamlets in air going through different PMMA range compensators. An analytic single Gaussian model is built on the response of MC simulations, for range compensator thicknesses and energies commonly used in particle therapy.
- σ_{pt}: The establishment of a better single Gaussian model for the description of the scattering inside the patient also accounting for patient heterogeneities.

3.3.B.1 *Monte Carlo simulations with Fluka*

The FLUKA MC code [123] [124] was selected for benchmarking TPS predictions and taken as golden standard for comparisons, as it is considered as a superior and accurate tool for dose calculation, especially in complex geometries and tissue heterogeneities, when compared to analytical algorithms. FLUKA has been validated to predict fluence and dose distributions within the accuracy requirements needed for clinical applications in particle therapy [125] [126] [127]. Indeed, one of the FLUKA MC code application is the validation of TPS dose prescription in hadrontherapy.

In the input files, the “HADRONTHErapy” default option, using δ-ray production and 100keV transport cuts, was selected. Neutrons are tracked down to thermal energies. Electromagnetic physics is described through the EMF package handling energy loss, straggling and MCS of charged particles. Proton-nucleus interactions are described by the PEANUT model [128], including an intra-nuclear cascade stage followed by a pre-equilibrium stage, and then the equilibrium.

The FLUKA output files, for dose estimations, are made of a matrix containing the released dose recorded in the cell (in $\mathrm{GeV.g^{-1}}$) associated to the statistical percent error on this quantity. Any kind of graphical representation (1D or 2D graphs), statistical analysis or fit can be realized from these dose matrices.

The FLUKA output dose volumes were used at two levels in the beam spread model improvement:

- to create the dataset of beam spread measurements in air due to the presence of a PMMA range compensator in the beam line (section 3.3.B.3). The new beamlet spread model is based on these beam spread measurements in air.
- to assess the new beamlet spread model in heterogeneous media (or in patients) – section 3.3.B.4.

The 2D map of a dose distribution released by an infinitesimal beamlet in water computed by FLUKA is shown as in Figure 2-1.

3.3.B.2 *Radial dose profiles analysis with ROOT*

The CERN ROOT [129] multiplatform framework and the MINUIT minimization package [130] were used to fit, by single Gaussian functions, proton lateral dose profiles in different materials. The MINUIT package is a minimization tool for multi-parameters functions that computes the best fit parameter values and their associated uncertainty. Only the dose superior to 20% of the central axis dose was considered for the fit samples, in order to neglect the signal from the second Gaussian model (especially single scattering and nuclear interactions) and build a beam spread dataset due to MCS only and compatible with the Hong’s single Gaussian model. The beam spread value, or SDPBP, represented by the FWHM of the Gaussian distribution, was retrieved together with its error evaluation by the association of ROOT and MINUIT, as shown on Figure 3-19.

Figure 3-19

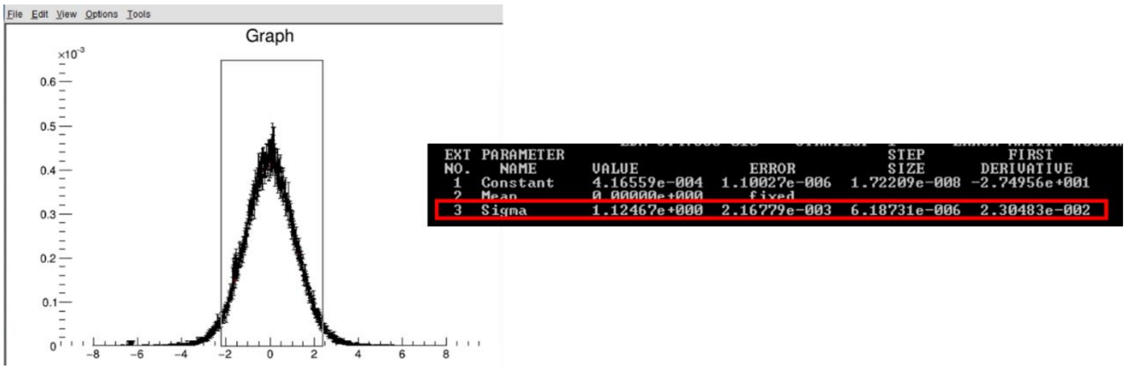

```
 EXT PARAMETER                                STEP         FIRST
 NO.   NAME      VALUE          ERROR          SIZE      DERIVATIVE
  1  Constant    4.16559e-004  1.10027e-006  1.72209e-008 -2.74956e+001
  2  Mean        0.00000e+000     fixed
  3  Sigma       1.12467e+000  2.16779e-003  6.18731e-006  2.30483e-002
```

Beam spread estimation on lateral dose profiles computed by Monte Carlo simulations (left), fitted by ROOT/MINUIT as a single Gaussian model (right). The sigma parameter represents the beamlet spread for the single Gaussian model. The single Gaussian fit is represented on the left picture (red line) but is hidden by the experimental data (black error bars).

3.3.B.3 Optimization of the beamlet spread model induced by a range compensator based on MC measurements

Hong proposed a general description of the beamlet spread in air due to the presence of a range compensator introduced in the beam line (model A in Table 3-1, the range compensator geometry is reported in Figure 3-9). When compared to MC simulation (see section 4.A.1.5), the beamlet spread estimations in PMMA are underestimated from about 8%.

Preliminary MC simulations and Hong's study [70] confirmed that only three input parameters are significant to describe the beamlet spread in air due to a range compensator: the incident energy of protons E, the physical length of the range compensator l and z_0 the depth of interest from the downward face of the range compensator. Hong observed that the parameter l/R is more suitable than l as an input parameter model, as the maximal characteristic angle in the range compensator is empirically almost independent from the incident particle energy.

In this study, in addition to the Hong's beam spread model, four different models are proposed and semi-empirically built on MC simulations data. In a second time, new and independent MC simulations with random input parameters are compared to the output response of these models as an evaluation of their accuracy. The four new models, B, C, D and E are presented in Table 3-1.

A dataset of beam spread measurements in air, from infinitesimal thin beamlets going through different PMMA range compensator thicknesses, was created from MC simulations. The beam spread were measured at 5 different distances from the downward surface of the range compensators (25, 50, 75, 100 and 150 cm), for energies in the particle therapy range (40-220 MeV) and range compensator thicknesses varying from 0 to the range of the protons in PMMA for each energy. Distances greater than 50 cm are not clinically relevant, but these configurations were used to determine in a more accurate way the beam spread occurring in the range compensator, taking advantage of the geometric dilatation in vacuum. The incident pencil beamlets were perpendicular to the entrance surface of the range collimator. Every simulation from this dataset was realized with 10 runs of 5×10^5 proton histories. The beam spread was evaluated from radial dose profiles in air at the 5 distances mentioned above, along a parallelepiped. The voxel resolutions of this parallelepiped were $\Delta x \times \Delta y \times \Delta z = 0.1\,mm \times 2\,mm \times 4mm$. The response accuracy of the five models is assessed in section 4.B.1.1.

Table 3-1

Name	Semi-empirical expression	Function to be defined by MC simulations
A – Hong	$\sigma_{rc}(E,l,z) = \theta_0(E) \times \gamma(l/R) \times \left(z_0 + z'_{RC}(l,E)\right)$	All the functions are defined from look-up tables
B	$\sigma_{rc}(E,l,z) = f_1(E) \times f_2(l/R) \times z_0$	f_1, f_2
C	$\sigma_{rc}(E,l,z) = f_1(E) \times f_2(l/R) \times (z_0 + l)$	f_1, f_2
D	$\sigma_{rc}(E,l,z) = f_1(E) \times f_2(l/R) \times \left(z_0 + z'_{RC}(l,E)\right)$	f_1, f_2 z'_{RC} is determined from a look-up table
E	$\sigma_{rc}(E,l,z) = f_1(E) \times f_2(l/R) \times \left(z_0 + z'(l,E)\right)$	f_1, f_2, z'

Mathematic definition of the alternative models proposed in this study. The parameters signification is defined in Figure 3-9 and section 3.3.A.5.

3.3.B.4 The differential scattering in patient heterogeneities

In Equation 3-4, the expression of the beam spread in homogeneous medium was expressed as an approximation in homogeneous media. Unfortunately, this model is accurate in homogeneous media only and can lead to important errors in air gaps and in high density heterogeneities [89] [131] [132]. Many studies have proposed corrections for heterogeneities, and different models are available to account for heterogeneities [46] [89] [133] [134]. By using the T_5 scattering power definition (see section 2.5.5), Kanematsu [112] derived a differential expression of the scattering power in heterogeneous media:

$$T_5 = \left(\frac{15.0\,MeV}{pv}\right)^2 \frac{1}{X_0} \times f_{dH}(l)$$

$$with\; l(x) = \int_0^x \frac{du}{X_0(u)}$$

$$and\; f_{dH}\big(l(x)\big) = 0.970 \times \left(1 + \frac{\ln l(x)}{20.7}\right)\left(1 + \frac{\ln l(x)}{22.7}\right)$$

Equation 3-6

In this approach the scattering media is decomposed in dx-thick slabs of different materials, each slab contributing to the global beamlet spread σ at the depth of interest z.

By using Equation 3-6 and Equation 2-7,

$$\sigma_{pt}(z)^2 = \int_0^z (z-u)^2 T(u)\,du$$

$$= \int_0^z (z-u)^2 \left(\frac{15.0\ MeV}{(pv)(u)}\right)^2 \frac{1}{X_0(u)} \times f_{dH}\big(l(u)\big)du$$

Kanematsu [112] [135] mentioned that as a first approximation:

$$\frac{1}{l}\int_0^l f_{dH}(l)dl \approx \left(1+\frac{1}{9}log_{10}\, l\right)^2 \times 0.94^2$$

So as a first approximation,

$$\sigma_{pt}(z)^2 = (15.0 \times 0.94)^2 \left(1+\frac{1}{9}log_{10}\, l\right)^2 \int_0^z \left(\frac{z-u}{pv(u)}\right)^2 \frac{du}{X_0(u)}$$

Finally, the global expression of the beam spread at the depth of interest z is then:

$$\sigma_{pt}(z) = 14.1\left(1+\frac{1}{9}log_{10}\, l(z)\right)\sqrt{\int_0^z \left(\frac{z-u}{pv(u)}\right)^2 \frac{du}{X_0(u)}}$$

Equation 3-7

to be compared to the homogeneous approximation (Equation 3-4).

In this more complex approach, the beamlet spread doesn’t depend only on the water equivalent depth in the medium but also on the radiation length of the different materials crossed by the beamlet axis.

Moreover, the particle pathway history has a consequence on the final beamlet spread. As the energy losses are different in any material, these quantities have to be assessed in any dx-slab. In other words, both the position and the composition of the materials are taken into account in this model, due to the integrated term of Equation 3-7 and the definition of l that cannot be simplified for general heterogeneities. Two configurations with the same material thicknesses but placed at different depths lead to different beam spread at the depth of interest z. This is a different approach respected to the Hong approximation that defines a beam spread directly from the WED crossed without considering the position of the eventual heterogeneities.

In order to evaluate the beamlet spread at a depth of interest z, Equation 3-7 must be integrated along the beamlet pathway axis. This integration is computed by analyzing the medium in each voxel crossed by the beamlet axis ray: both the radiation length X_0 and the stopping power ratio $pSTPR_m$ have to be determined. The direct determination of these two quantities from HU numbers in the input CT-images is explained in the Appendix A of this report.

The momentum and the velocity of the particles, integrated in Equation 3-7, were implemented by using their relativistic definition, considering the energy loss in every dx-slab of material along the pencil beam axis. For each step in the medium, the momentum p and the velocity v of particles of kinetic energy E are both reasonably supposed constant in the dx-slab:

$$p = \frac{\sqrt{2E(E + mc^2)}}{c}$$

and

$$v = c\sqrt{1 - \left(\frac{mc^2}{E + mc^2}\right)^2}$$

with mc^2 the proton energy at rest.

The energy lost in the dx-slab is calculated from the proton stopping power ratio of the material $pSTPR_m$ (extracted from the correlation reported in Appendix A2) and from the proton stopping power in water $\left(\frac{dE}{dx}(E)\right)_w$ defined as a look-up table from the National Institute of Standards and Technology (NIST) proton data [32]:

$$\Delta E = -pSTPR_m \times \left(\frac{dE}{dx}(E)\right)_w \Delta x$$

3.3.C Materials and Methods – Part C – *Software interface*

3.3.C.1 TPS and open-source policy

In order to help the research groups that couldn't afford a proton TPS, this project provides to the scientific community an open-source TPS implemented in the 3D slicer software. This report presents the interface of the software, for a passively scattered proton beam line. This project was created and founded by the National Alliance for Medical Image Computing (NA-MIC). This TPS is released as a multiplatform software, included in the SlicerRt toolkit (see section 3.3.C.2), an add-in package of 3D Slicer.

This TPS software is composed of an interface and allows a visualization of the CT-input images (including DICOM images), the volume definitions and visualizations by the help of tools already developed in 3D Slicer. Once the input parameters are set in the interface, the Plastimatch DCE can be called: the software transfers the treatment plan settings to the DCE which returns after a couple of seconds or minutes the ODV associated to these input parameters.

3.3.C.2 3D Slicer, the SlicerRT toolkit and the Plastimatch DCE

The 3D slicer software was originally built as an open-source software dedicated to medical image visualization and computation [136]. It is developed in C++ and is multiplatform. The source code is released under a BSD-style licensing agreement, including no restrictions on its use: the user is free to make any change on the source code and use it as needed. The source code is available on-line from the 3D slicer official website [136].

This proton TPS is released in the SlicerRt toolkit [137], an add-in toolkit of 3D Slicer devoted to image computation and visualization tools dedicated to research in the radiation therapy field. The SlicerRt toolkit contains 4 extensions: the SlicerRt code, Matlab Bridge, Multi-dimensional Data and Gel Dosimetry [120] [138] [139].

Both 3D Slicer software and the SlicerRt toolkit are regularly updated with new functions thanks to flexible, maintainable architecture and automated testing. The Plastimatch DCE algorithm called by the SlicerRt toolkit is based on PBA and is described in Part A and B, which the reader can consult for details.

3.3.C.3 Treatment plan settings hierarchy

In the DCE hierarchy, the input parameters of the proton treatment plan are members of a RtPlan class. Each RtPlan class contains a set of parameters only related to the general plan settings (like the name of the plan, the input CT-images and output ODV locations, the dose prescription…) but also RtBeam subclasses, one for each beam of the plan, as shown on Figure 3-20.

Each RtBeam subclass defines a unique beam configuration and encloses a pointer containing its associated sub-ODV: this volume contains the computed dose induced by the settings of this beam. A RtPlan can contain as many beams as required as shown in Figure 3-20 (left). Multiple-beams dose computation is then possible by simply calling the DCE as a loop on each of the RtBeam class contained in the RtPlan, one after the other. The total ODV computed by the DCE and corresponding to the entire plan is simply the sum of each weighted sub-ODV.

Figure 3-20

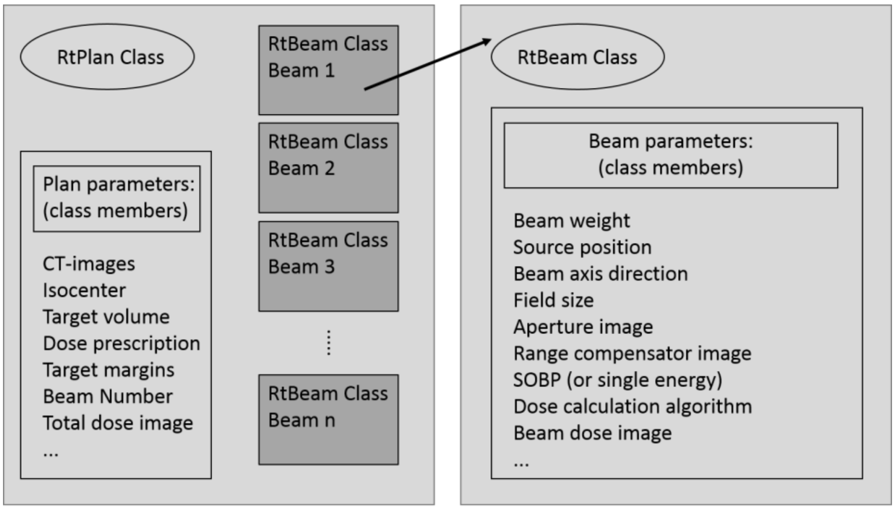

Hierarchy of the treatment planning settings. The hierarchy is mainly divided into two levels: the RtPlan classes (left), and the RtBeam classes (right) included as subclasses of the RtPlan class.

3.3.C.4 Software interface implementation and 3D visualization tools

The software interface was implemented with the help of Qt libraries in the SlicerRt toolkit (see section 3.3.C.2). This library allows the creation of different modules defining both plan and beam parameters with user-friendly tools. Coupled with the ITK library, the interface provides also the opportunity to visualize the input CT-images, including the associated structures that can be considered for treatment planning (like the beam geometry shape or the position of the RDP).

As a commercial TPS, the SlicerRt toolkit proposes a beam geometry visualization implemented with the VTK library: when a beam is created as a new object (from the interface action “add beam”), the beam orientation and limits are displayable on the input CT-images. This 3D beam shape visualization is automatically updated if the user changes a beam parameter from the interface. Moreover, two other tools helping the user are also available from the SlicerRt toolkit: a Beam Eye View (BEV) image creator and a Digital Reconstructed Radiography (DRR) creator (tools created by the SlicerRt team before this project).

Once the minimal set of plan parameters is set by the user (CT input images, isocenter, source…), the interface transfers the plan parameters to the DCE that returns the total ODV. Finally, this ODV can be overlapped on the input CT-images volume and its associated structures, with the help of dose visualization tools (colorwash images, isodoses…) to help the user in the dosimetric validation of the treatment plan.

This list of available functionalities from the interface is not exhaustive, we incite the reader to try it by itself in order to have a full overview of the abilities of this software. Some screenshots of the interface are shown in section 4.C.1.3 for two treatment planning examples (pelvis and brain regions, Figure 4-33 and Figure 4-34).

4. RESULTS, DISCUSSIONS AND CONCLUSION

4.A Part A – The beam line

4.A.1 Results – *The beam line*

4.A.1.1 The ray tracer tool adapted to particle therapy

The ray tracer tool, an algorithm already implemented in Plastimatch that samples different quantities in an input image volume, was modified to provide physical properties associated to particle therapy such as material density or stopping power ratios. Accumulated and non-local physical properties were also computed, such as the radiologic WED or proton WED. The ray tracer tool is the keystone of every dose computation process in Plastimatch.

Figure 4-1 shows a concrete example of the determination of a local parameter and a non-local parameter along the ray axis, using the ray tracer tool: the HU (Figure 4-1, center) and its associated proton WED (Figure 4-1, right), sampled in Head & Neck CT-images.

Figure 4-1

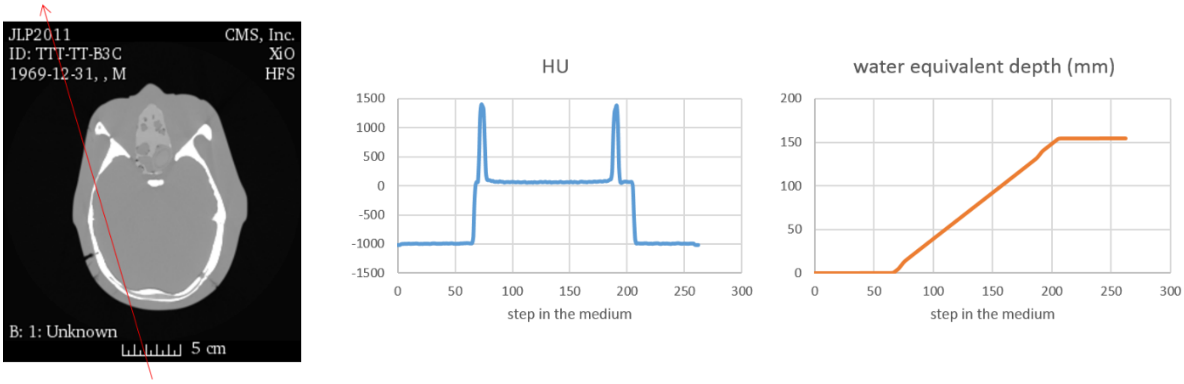

Left: example of the ray tracer tool on real CT-images. The sampling step is 1 mm. Middle: the HU values along the ray tracer (red arrow on the left image). Right: proton WED, a non-local, accumulated property of the medium.

4.A.1.2 The automatic collimator shaper

In this paragraph, an example of the automatic creation of a collimator is presented. The method, described in the section 3.3.A.4, considers the geometric information of a target volume for the creation of a 2D collimator associated to the beam incidence and field size. Figure 4-2 shows an automatic collimator created by our algorithm on pelvis CT-images, for a prostate target volume, the collimator being enlarged by 5 mm lateral margins (smearing) around it to guarantee the lateral dose equilibrium even for the most external parts of the target volume.

Figure 4-2

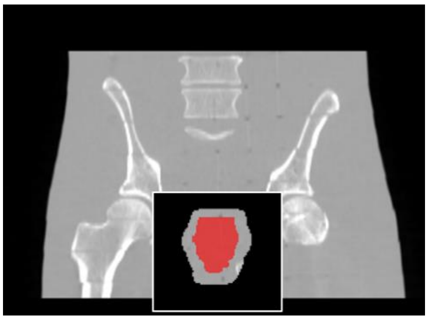

Overlap of the target volume and the collimator created from this projection of this target volume (prostate) including 5 mm margins. The collimator shape corresponds the projection of the entire volume and not only of the slice showed in the example.

4.A.1.3 The automatic creation of a range compensator

As the collimator, the range compensator device introduced in the beam line reduces substantially the dose released to healthy tissues, but this time downward the target volume. Section 3.3.A.5 explains the process of the range compensator creation by computed the maximum proton WED crossed by the ray tracer tool in the target volume. The example of an automatic creation of a range compensator, associated to the previous beam configuration and collimator (section 4.A.1.2) is reported in Figure 4-3.

Figure 4-3

Left: a sagittal view of the patient highlighting the differences of WED to be crossed to reach the most distal parts of the target volume (red). The green lines represent the anterior beam geometry. Center: collimator (smearing 5 mm) automatically created as shown in Figure 4-2 and range compensator (smearing: 5 mm) automatically created associated to the beam on the left image and to the collimator on the central image. The PMMA thickness is shown on a grey scale, from 0 cm (black) to the maximal thickness – 13.8 cm (white). Right: sagittal view of the range compensator effect on the dose distribution (RT) surrounding the target volume (white).

4.A.1.4 The spread out Bragg peak automatic designer

The method to build a SOBP depth dose from weighted Bragg peaks was described in section 3.3.A.8. The output depth dose distributions computed by the algorithm implemented in Plastimatch for two different input conditions is shown in Figure 4-4. On these figures are also reported the weighted mono-energetic beams used to create this particular homogeneous shape. In Figure 4-4, the maximal dose discrepancy from the dose prescription in the target volume region was 2.1%.

Figure 4-4

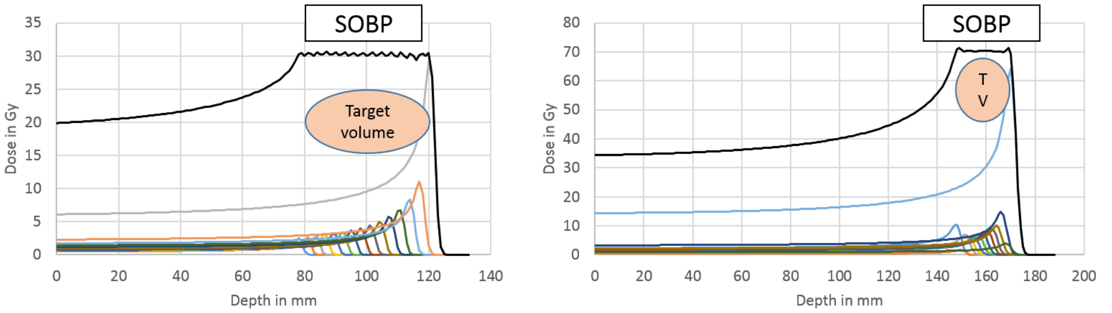

SOBPs (plain black lines) computed by the Plastimatch SOBP designer and their associated weighted Bragg peaks (plain colored lines). Left: SOBP built on a 80-120 mm depth target volume (dose prescription: 30 Gy), based on Bragg peaks with a 2 MeV energy resolution. Right: SOBP built on a 150-170 mm depth Target Volume (TV, dose prescription 70 Gy)), based on Bragg peaks with a 1 MeV energy resolution.

4.A.1.5 Beam spread due to the range compensator

In this paragraph, the accuracy of the Hong beamlet spread (SDPBP) in air after passing through a range compensator is compared to the SDPBP measured by MC simulations (Fluka, see section 3.3.B.1) in the same conditions. The implemented Hong model (see model A in Table 3-1 in Plastimatch includes also the correction for the effective scattering origin in the range compensator. In this study, a single infinitesimal pencil beamlet goes through different PMMA range compensator thicknesses, from 0 cm to the range of the particles (Figure 4-5). The dose spot size was assessed in air slabs located within a vacuum at 3 different depths (50, 100 and 150 cm) from the downward face of the range compensator, for 100 MeV and 225 MeV proton beamlets. Table 1 shows the SDPBP response of both the Hong's algorithm and MC simulations.

Figure 4-5

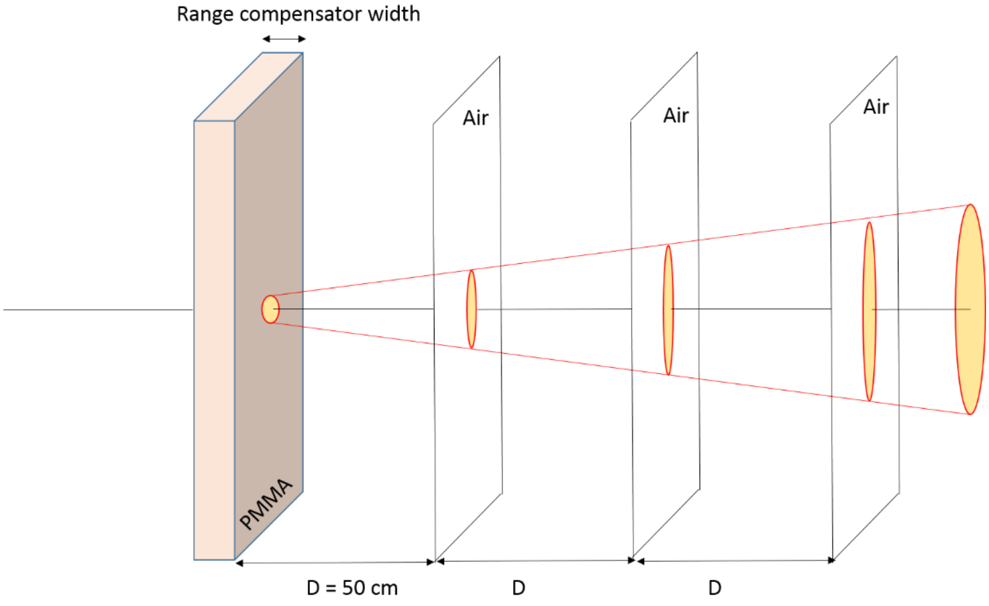

Estimation of the SDPBP due to the range compensator at 3 different depth in air for 100 MeV and 225 MeV proton beamlets.

Table 4-1

	RC thickness (mm)	RC + 50 cm			RC+ 100 cm			RC +150 cm		
		MC	Hong	Discrepancy	MC	Hong	Discrepancy	MC	Hong	Discrepancy
100 MeV	0	0 ± 0	0	-	0 ± 0	0	-	0 ± 0	0	-
	10	5.4 ± 0.1	5.3	-1.8%	11.0 ± 0.1	10.7	-2.7%	16.3 ± 0.4	16.1	-1.2%
	20	8.2 ± 0.1	7.4	-9.7%	16.5 ± 0.1	15.0	-9.1%	24.6 ± 0.2	22.5	-8.5%
	30	10.6 ± 0.1	9.7	-8.5%	21.9 ± 0.1	19.7	-10.0%	31.9 ± 0.2	29.8	-6.6%
	40	13.4 ± 0.1	12.3	-8.2%	27.0 ± 0.2	25.2	-6.6%	40.8 ± 0.2	38.2	-6.4%
	50	16.6 ± 0.1	15.0	-9.6%	34.1 ± 0.2	30.9	-9.4%	51.5 ± 0.3	46.9	-8.9%
	60	20.5 ± 0.2	19.8	-3.4%	44.3 ± 0.2	41.5	-6.3%	66.9 ± 0.3	63.1	-5.6%

	RC thickness (mm)	Range compensator + 50 cm			Range compensator + 100 cm			Range compensator +150 cm		
		MC	Hong	Discrepancy	MC	Hong	Discrepancy	MC	Hong	Discrepancy
225 MeV	0	0 ± 0	0	-	0 ± 0	0	-	0 ± 0	0	-
	40	5.4 ± 0.1	5.1	-5.5%	10.4 ± 0.1	10.5	+0.9%	15.7 ± 0.1	15.8	+0.6%
	80	7.4 ± 0.1	6.8	-8.1%	15.6 ± 0.1	14.3	-8.3%	23.0 ± 0.1	21.8	-5.2%
	120	9.3 ± 0.1	8.5	-8.6%	19.6 ± 0.1	18.3	-6.6%	29.8 ± 0.1	28.1	-5.7%
	160	11.1 ± 0.1	10.3	-7.2%	23.9 ± 0.2	22.8	-4.6%	36.7 ± 0.2	35.4	-3.5%
	200	12.9 ± 0.1	11.8	-8.5%	28.9 ± 0.2	27.2	-5.9%	44.9 ± 0.2	42.6	-5.1%
	240	14.3 ± 0.1	13.4	-6.2%	34.5 ± 0.2	33.0	-4.3%	52.4 ± 0.3	52.7	+0.5%

Comparison of the SDPBP estimated by the Hong algorithm and measured by MC simulations.

4.A.1.6 Hong's approximation – Material independency

In semi-infinite materials, Hong stated that as a first approximation the relative amplitude γ of the SDPBP shape doesn't depend on either particle energy or material composition, only the amplitude $\sigma_{0,mat}$ is material dependent. In other words, in Equation 3-5, γ depends on l/R only and the maximal SDPBP $\sigma_{0,mat}$ is both material and energy dependent. Figure 4-6 shows the two functions $\sigma_{0,mat}$ and γ computed along the depth, by using Equation 3-5. The radiation lengths of the materials were extracted from the Groom's look-up tables [140], and the stopping powers from the NIST data [32]. These results confirm the reasonable decomposition of the SDPBP in the absolute $\sigma_{0,mat}(E)$ and relative $\gamma(t/R)$ functions in homogeneous media.

Figure 4-6

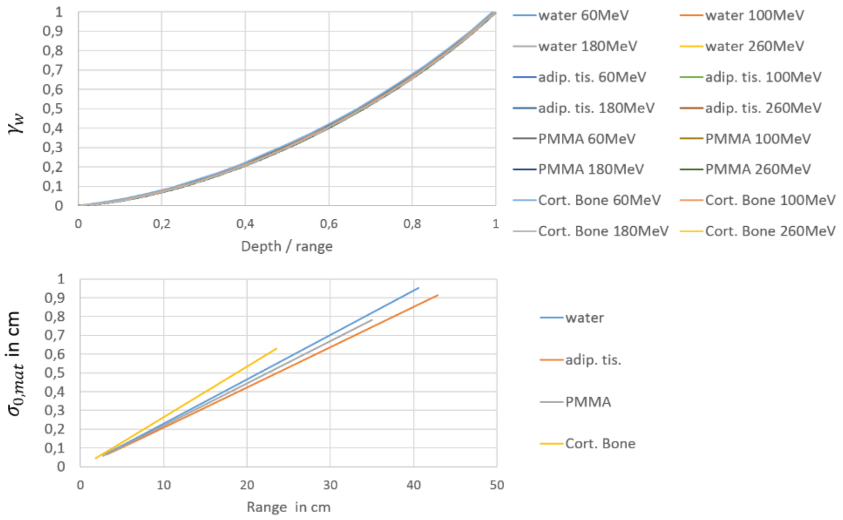

Computation of the γ and $\sigma_{0,mat}$ functions from the Highland approximation in semi-infinite homogeneous phantoms.

4.A.1.7 *Hong's SDPBP model due to scattering in water and bone homogenous phantoms*

Lateral dose profiles were assessed at different depths in semi-infinite water phantoms and in semi-infinite cortical bones phantoms by MC simulations and compared to the SDPBP computed in the same conditions by the Hong's homogeneous approximation implemented in Plastimatch. The SDPBP was estimated along the pencil beamlet axis in water at different depths from lateral dose profiles (see Figure 4-7). Figure 4-8 reports the SDPBP computed by Plastimatch in a water phantom and the SDPBP computed in a cortical bone phantom. In this experiment, the phantoms were created synthetically according to:

- Water phantom: $HU = 0, \rho = 1 g.cm^{-3}$.
- Cortical bones phantom (ICRU): $HU = 1300, \rho = 1.85 g.cm^{-3}$ [32].

The Fluka default material cards library for water and cortical bones were chosen for the MC simulations.

Figure 4-7

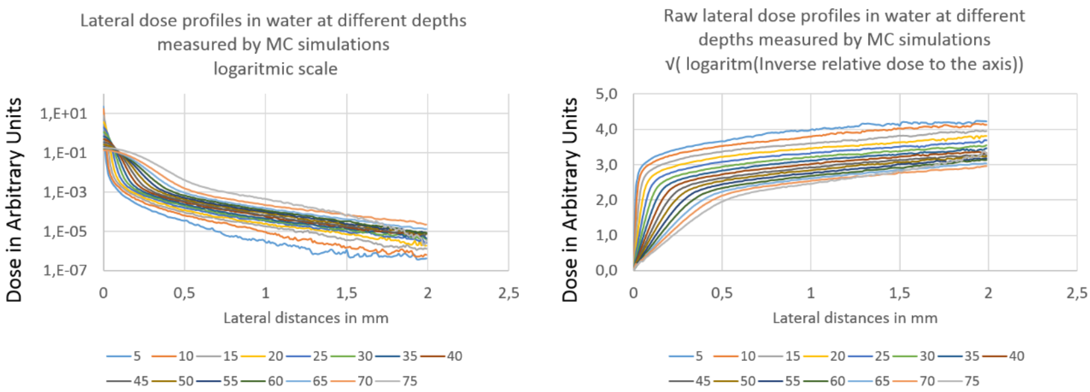

Left: lateral dose profiles at different depths in water for a 100 MeV proton beamlet (logarithmic scale). Right: square root of the logarithm of the inverse relative dose in order to highlight the two sigma values of the double Gaussian model. The first linear coefficient is proportional to the inverse of the SDPBP of the single Gaussian model, the second linear coefficient is proportional to the inverse of the SDPBP describing the nuclear halo (not considered in this study).

Figure 4-8

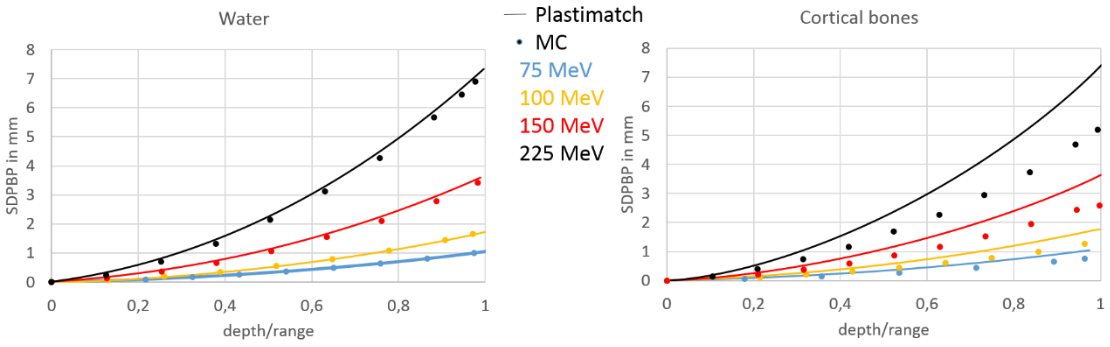

SDPBP due to scattering in homogeneous media (left: water and right: cortical bones) computed by the Hong algorithm and measured by MC simulations. In bones, the pencil beamlet is based on the water pencil beam model scaled according to the WED in bones.

4.A.1.8 Dose summation algorithms

Qualitative analysis (mono-energetic beams):

Section 4.A.1.7 reported that the Hong's model for SDPBP computations is satisfying in water. Figure 4-9 and Figure 4-11 report the different ODV computed by Plastimatch by calling the 4 different algorithms described in section 3.3.A.9 (Ray Tracer (RT), Cartesian Geometry dose Summation (CGS), Divergent Geometry dose Summation (DGS) and Hong Geometry dose Summation (HGS)) in a water cubic phantom. The dose computation was performed with the following conditions: the source and the beam aperture are respectively located (in air) at 2000 mm and 500 mm from the phantom surface. The beam is built to be an exact 50 mm × 50 mm square field at the surface phantom (pencil beam spacing at the aperture 0.37 mm × 0.37 mm). The initial particles energy is set to 100 MeV ($R = 77$ mm in water). The cubic water phantom dimensions are 100 mm × 100 mm × 100 mm and its resolution is 1 mm × 1 mm × 1 mm. The computation times were 3 seconds for RT, 15 seconds for CGS, 40 seconds for DGS and 92 seconds for HGS (performed on a laptop dual core, 2.20 GHz).

Figure 4-9

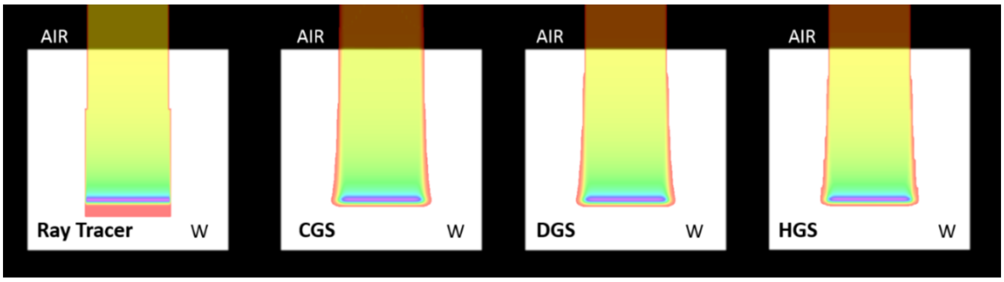

3D dose distributions computed in large beam configurations by the four dose summation algorithms described in section 3.3.A.9.

The same beam configuration was applied to a cylindrical lung phantom (see Figure 4-10 for the geometric definition). This phantom was aligned in the same conditions as the previous paragraph. The computed dose by RT, CGS, DGS and HGS are shown in Figure 4-11. For information purposes, the computation time were 1.5 seconds for RT, 62 seconds for CGS, 59 seconds for DGS and 26 seconds for HGS (performed on a laptop dual core, 2.20 GHz).

Qualitative analysis (SOBP beams):

Figure 4-12 represents the ODV for the computation of SOBP beams in a cubic water phantom (100 mm × 100 mm × 100 mm, resolution 1 mm × 1 mm × 1 mm). The input parameters are identical to the previous examples, except for the field size (40 mm × 40 mm, pencil beam spacing at the phantom surface: 1 mm × 1 mm). The minimal and maximal depth limits for the SOBP definition were respectively set to 50 mm and 70 mm (corresponding to 19 weighted Bragg peaks from 78 MeV to 96 MeV).

The computation times were 3 seconds for RT, 32 seconds for CGS, 53 seconds for DGS and 137 seconds for HGS (performed on a laptop dual core, 2.20 GHz).

Figure 4-10

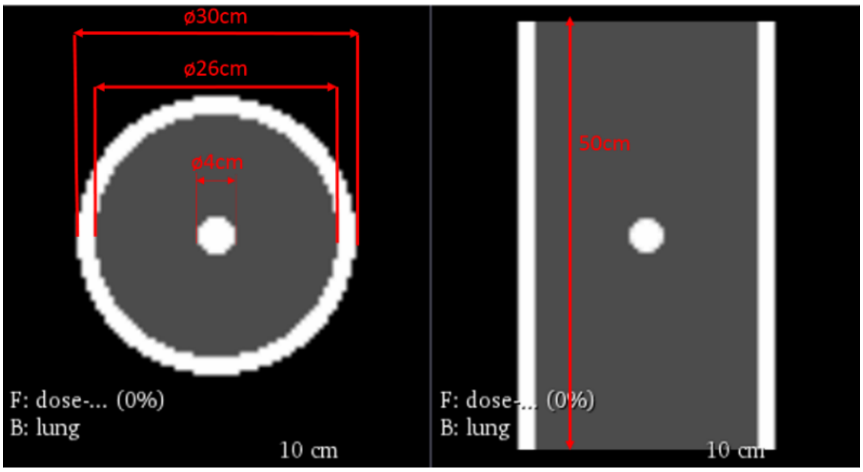

Lung phantom geometry definition. The global shape is a cylinder of dimensions 500 mm × 300 mm × 300 mm and resolution 2.5 mm × 2.5 mm × 5 mm. The different media are: air (black, $HU = -1000, \rho = 1.2 \times 10^{-3} g.cm^{-3}$*), lung (grey,* $HU = -700, \rho = 0.3 g.cm^{-3}$*) and water (white,* $HU = 0, \rho = 1 g.cm^{-3}$*).*

Figure 4-11

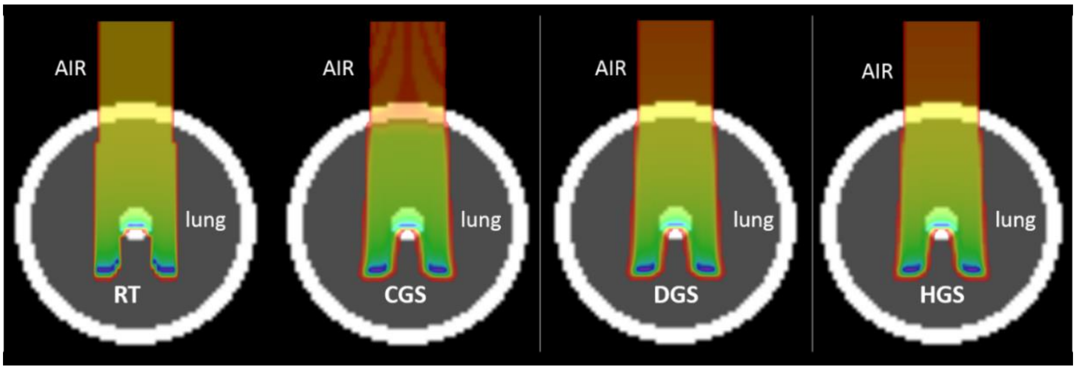

Dose computations in heterogeneous media (lung phantom, see Figure 4-10 for a descriptive geometry). The ODV are reported for the four algorithms RT, CGS, DGS and HGS for a 100 MeV proton beam.

Figure 4-12

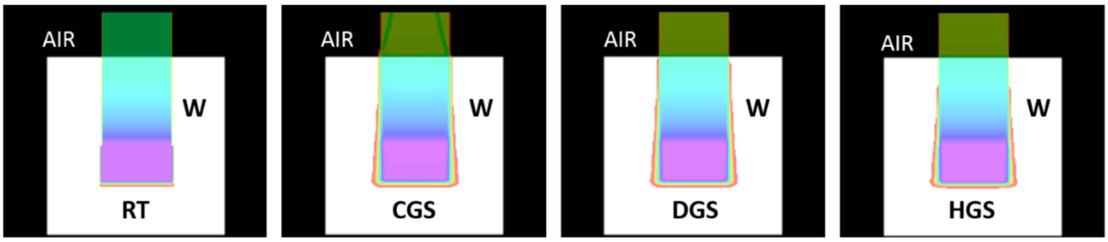

SOBP ODV for the four different algorithms implemented in Plastimatch. In this configuration, the SOBP minimal and maximal depth limits were respectively 50 mm and 70 mm.

Quantitative analysis (mono-energetic beams):

The previous paragraph was dedicated to the qualitative analysis of the different algorithms in broad beam conditions. In this paragraph, we compare the ODV computed by the four algorithms to MC simulations in the same conditions on different profiles. The geometric configurations are identical to the experiment in Figure 4-9, except for the field size: 60 mm × 60 mm at the phantom entrance (pencil beam spacing at the surface phantom: 0.5 mm × 0.5 mm). The Monte Carlo simulations were performed with 20 runs of 10^6 histories for each run. Figure 4-13 and Figure 4-14 shows respectively the depth dose curves along the beam axis $(x = y = 0)$ and the lateral dose profiles at 75 mm depth in water (the initial energy of protons is 100 MeV, corresponding to a range of 77 mm).

Figure 4-13

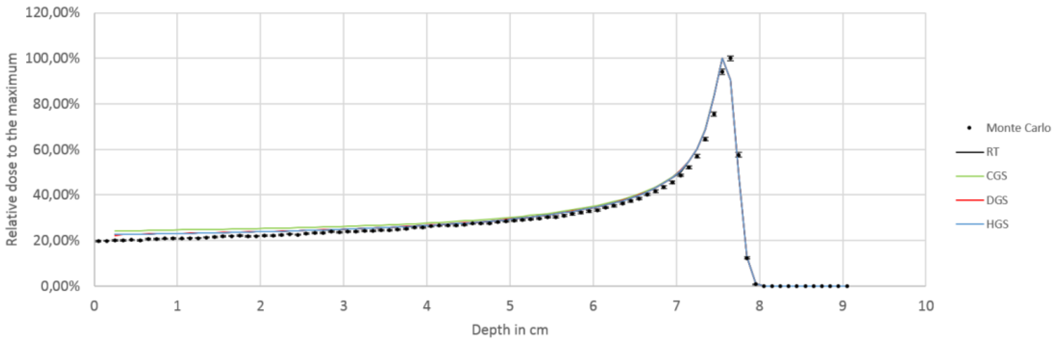

Depth dose profiles along the beam axis. Comparison between MC simulations (dots) and the four algorithms implemented in Plastimatch (RT, CGS, DGS, HGS).

Figure 4-14

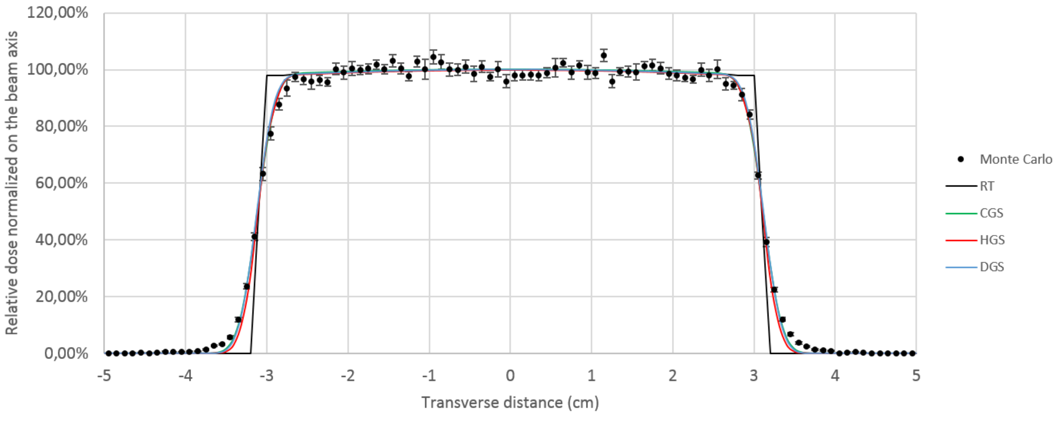

Lateral dose profile at 75 mm depth in a water phantom, normalized on the beam axis for Monte Carlo simulations and the four algorithms implemented in Plastimatch (RT, CGS, DGS and HGS).

Quantitative analysis (SOBP beams):

For SOBP the lateral profiles are similar to Figure 4-14, and the depth dose curves are equivalent to Figure 4-4. In order to show the accuracy of the dose reconstruction method, the maximal and minimal dose in the SOBP 3D regions of Figure 4-12 are reported in Table 4-2. The prescription dose in Figure 4-12 was 70 Gy.

Table 4-2

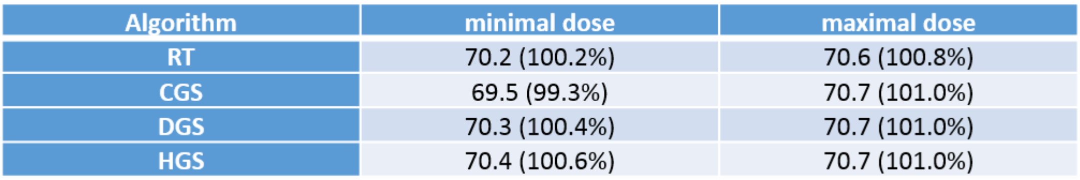

Algorithm	minimal dose	maximal dose
RT	70.2 (100.2%)	70.6 (100.8%)
CGS	69.5 (99.3%)	70.7 (101.0%)
DGS	70.3 (100.4%)	70.7 (101.0%)
HGS	70.4 (100.6%)	70.7 (101.0%)

Minimal and maximal doses determined in the SOBP area (50 mm-70 mm) in Figure 4-12.

4.A.1.9 The projected source size determination – example of the MGH beam line

The projected source size is determined from a comparison between experimental and computed lateral dose profiles. Ideally, the matching of the penumbras on lateral dose profiles should be done in air, in order to avoid the degradation of the method accuracy due to the model of the pencil beam in water. Unfortunately, in this study, only lateral dose profiles in a water phantom were provided from the Massachusetts General Hospital's (MGH) TPS XiO, calibrated on the MGH proton passively scattered beam line.

The penumbra width at a depth of 10 cm in water was computed for different projected source sizes. The effective position of the source was set at 2270 mm (source - aperture distance = 1870 mm), corresponding to the MGH beam line configuration. The geometric field size was set to be 9.8 cm × 9.8 cm at 10 cm depth in a water phantom. The penumbra width was defined on the lateral dose profiles by the distance between the 10% (left) - 10% (right) relative doses normalized to the central dose.

Using the XiO TPS simulating the MGH beamline, the penumbra width was experimentally extracted from lateral profiles as being 100.7 mm wide for 175 MeV protons. According to Figure 4-15-A, providing the penumbra widths based on Plastimatch computations of 175 MeV proton beams in the same conditions for different projected source sizes, the MGH's projected source size was estimated at 0.38 mm. Figure 4-15 shows the XiO and Plastimatch lateral dose profiles for a 0.38 mm source size at 3 different depths: 10 cm, 15 cm and 19.5 cm in water in the previous geometric conditions. As said above, in this approach, the accuracy of the projected source size determination is reduced by inaccuracies induced by the scattering in water. The same method on lateral dose profiles in air would be much more accurate. This method is only proposed as a description of the method.

Figure 4-15

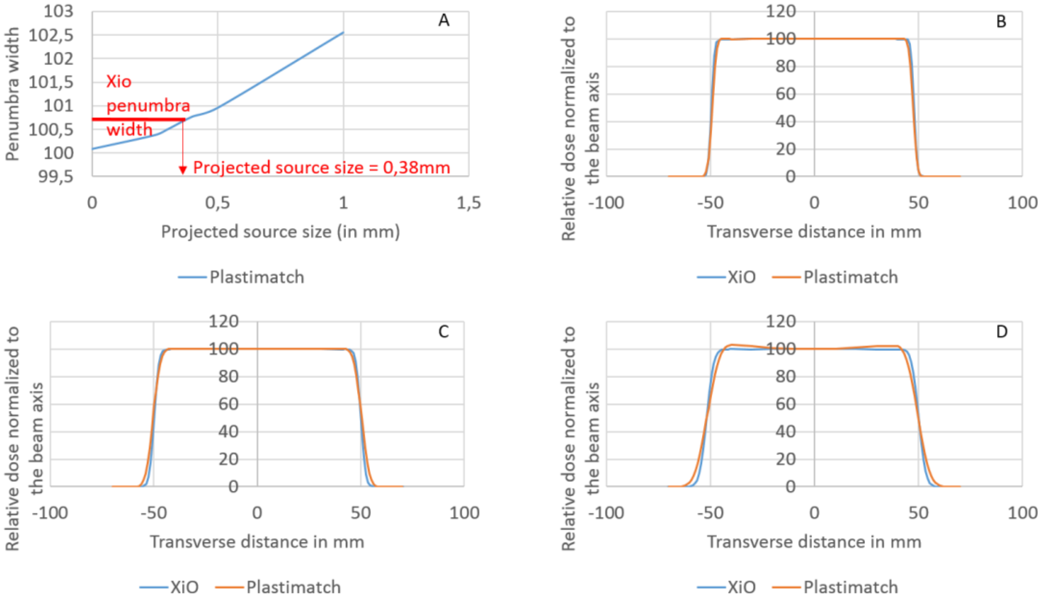

A - Projected source determination (0.38 mm) from Plastimatch dose computation. B, C and D – relative dose profiles measured (XiO, red) and computed (Plastimatch, blue) at different depths: B: 10 cm, C: 15 cm and D: 19.5 cm.

4.A.2 Discussion – *The beam line*

4.A.2.1 Automatic dose shaper tools (collimator, range compensator and SOBP creator)

Figure 4-2 and Figure 4-3 showed real examples confirming that collimators and range compensators are correctly designed in a beam frame: the collimator matches the 2D projection of a 3D volume in the beam frame, the range compensator compensates the lack of medium upward the distal surface of the target volume in the same beam frame. In section 4.A.1.4, dose computations in easy geometries involving the SOBP creator provided a good and homogeneous coverage of the target volume whatsoever its position and width: the maximum dose discrepancy in the target volume was evaluated to 2.1%. The effect on the dose conformation induced by these three combined tools is evaluated in Part C on real treatment planning situations.

4.A.2.2 The beamlet spread models

Source size beamlet spread:

The source size effect on the beam spread needs to be calibrated on experimental data and is not discussed here, as this model was validated in the literature. Moreover, this report is based on dose computation considering pointed sources ($source\ size = 0$), except for section 4.A.1.9. The user must determine the source size of the beam line he/she wants to simulate (also depending on the energy) and implement the right value in the input file. As seen in section 4.A.1.9, the model of the source size projection, based on penumbra width measurements, is more accurate on lateral dose profiles in air. From now on, the source size in this report is considered as being null for Plastimatch dose computations and MC simulations.

Range compensator beamlet spread:

The beam spread in the range compensator is a crucial piece of the development of a proton dose computation algorithm as most clinical treatments based on a passively scattered beam line require it. An accurate description of its broadening effect on the beamlet spread is thus very important for correct computations of 3D dose distributions. The response of Hong's model describing the beamlet spread broadening in the range compensator was assessed in section 4.A.1.5. As seen in Table 4-1, the Hong model systematically underestimates the SDPBP in PMMA by on average 5.8% at 100 MeV and 4.3% at 225 MeV when compared to MC simulations (Fluka). The Highland approach used by Hong for her model is reported in the literature as computing SDPBP estimations with a 10% accuracy (up to 20% in some critical cases [45]), the discrepancies estimated by MC measurements are also in the same order of magnitude.

The Highland approach is in average correct for general materials, but not dedicated to PMMA. For these reason, an alternative model dedicated to PMMA range compensators only and based on MC simulation is developed in Part B. Nevertheless, a 5% discrepancy on the SDPBP estimation is acceptable as a first approximation for dose computations.

As expected, the longitudinal effects of the range compensator created from the prostate clinical case (Figure 4-3) matches very well the distal surface of the target volume.

The beamlet spread due to scattering in homogeneous media:

Figure 4-8 showed that the estimation of the SDPBP in water computed by the Highland approximation is satisfying for any energy in the particle therapy energy range and is sufficient for an implementation in a DCE. On the contrary, when the model of the beam spread is scaled on WED in another material (like bones in Figure 4-8), the SDPBP computed by Plastimatch are not confirmed by the MC simulations. Indeed, as any model scaled on the WED of the material, the maximal SDPBP always equals the one in water, but this conclusion is refuted by MC measurements as seen on the different values of $\sigma_{0,mat}$ (Figure 4-6 - right). The conclusion of this section is that for water equivalent media, the Highland/Hong approach of WED scaled pencil beams is acceptable as a first approximation. However, the user must be very careful about dose computations in heterogeneous media or in a homogeneous materials that are not water equivalent (like bones or air). The Hong approach is then valid as a first approximation for easy geometries and water equivalent materials, but in order to compute ODV with a higher accuracy, algorithms dealing with any media (homogeneous and heterogeneous) must be developed. Part B proposes an alternative model to the Highland/Hong approach, based on the scattering power of media along the pencil beam axis and accounting for media heterogeneities, as explained in section 3.3.B.4.

4.A.2.3 Dose summation algorithms

A simple RT dose algorithm and three different pencil beam dose summation algorithm methods were described in section 3.3.A.9 and their ODV in broad beam conditions were reported in Figure 4-9. Figure 4-13 and Figure 4-14 show that if the description of the SDPBP in a medium is accurate, the three dose summation algorithms build an ODV that matches the MC simulations. On Figure 4-14, the field sizes (defined as the 50% - [10% - 90%] of the relative dose normalized to the central dose) at 7.5 cm depth in water) are reported in Table 4-3. As announced in section 3.3.A.9, the RT algorithm doesn’t consider any lateral scattering from the source size, range compensator and patient and doesn’t show any penumbra region on the reconstructed ODV.

A gamma analysis applied to the following results on the lateral profiles (2.5% - 2.5 mm) provided the scores reported in Table 4-3. The rejected voxels (gamma index > 1) are essentially located in the lowest part of the lateral penumbras of the beam (see Figure 4-14), where the dose is less than 5% and is partially explained by the fact that non-elastic nuclear interactions are not considered in the single Gaussian approach for all models implemented in Plastimatch. These results validate the dose reconstruction approach for the CGS, DGS and HGS, as long as the SDPBP is correctly computed in the medium, which is true for homogeneous water equivalent media as shown in the previous section. The case of non-water equivalent media and heterogeneous media will be solved in Part B. By downloading the open-source Plastimatch software [119] [120] and using the computation configuration mentioned in section 4.A.1.8, the reader can easily reproduce the ODV reported in this study.

Table 4-3

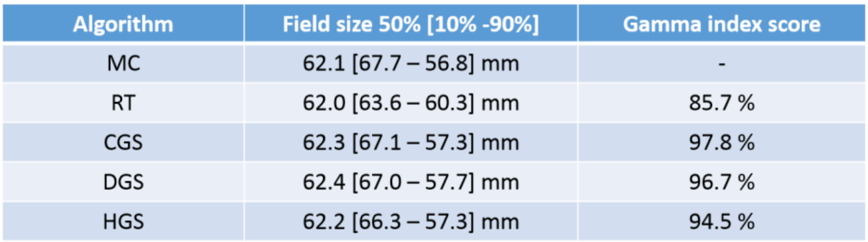

Algorithm	Field size 50% [10% -90%]	Gamma index score
MC	62.1 [67.7 – 56.8] mm	-
RT	62.0 [63.6 – 60.3] mm	85.7 %
CGS	62.3 [67.1 – 57.3] mm	97.8 %
DGS	62.4 [67.0 – 57.7] mm	96.7 %
HGS	62.2 [66.3 – 57.3] mm	94.5 %

Fields sizes and gamma index scores measured on Figure 4-14

4.B Results – Part B – The beam spread corrections

4.B.1 Results – *The beam spread correction*

4.B.1.1 Improvement of the model for the estimation of the SDPBP induced by the scattering in a PMMA range compensator

In section 4.A.2.2, Hong’s range compensator model used in PMMA was estimated to provide SDPBP with discrepancies of 5-10% when compared to MC simulations. In order to create a new model based on MC only, a study of the accuracy of 4 new models, dedicated to PMMA range compensators only, was performed. The four models (B, C, D, E) were described in Table 3-1, model A being the Hong’s algorithm tested in Part A. The free parameters of the four models are established in the next paragraphs on a dataset of SDPBP measured in air slabs within a vacuum on MC dose distributions with different input parameters: the distance z from the range compensator downward face, l the thickness of the range compensator and E the initial energy of the incident particles.

Scattering origin:

The z' function in model E is an alternative function to describe the scattering origin depth in the range compensator like z'_{RC} in model A and D. This function is still undefined and will be described with the help of the SDPBP dataset of this study measured on MC simulations. Each input parameter configuration provided the SDPBP measurements in air at 5 distances from the downstream face of the range compensator. For each of these simulations, the scattering origin depth z' was extracted from the origin shift of the linear model as following:

$$\sigma_{RC}(E, l, z) = A.z + B$$

A and B being numerically extracted from ROOT's fits thanks to the measurements at 5 different depths from the downward face of the range compensator. So:

$$\sigma_{RC}(E, l, z) = A.\left(z + \frac{B}{A}\right)$$

By a parametric identification, B/A corresponds to the expression of z' in the semi-empirical definition of model E and A to $f_1(E) \times f_2(l/R)$. The dataset for the distance dependency is based on 46 simulations, each one providing 5 measurements in air slices (distances: 25, 50, 75, 100 and 150 cm, $E = [80 - 220]$ MeV and $l/R = [0 - 1]$). The SDPBPs measured in these conditions are reported in Appendix C1. The dataset with energy less than 80 MeV was not considered for this study as the range of the particles is too small (nearly 1 cm), as are the range compensator thicknesses involved (2-20 mm). The position of the origin of scattering is subjected to statistical noise, greater than the associated range compensator thicknesses. This inaccurate data subset is then unusable and was discarded. Figure 4-16 shows the different z'/l values with respect to l/R for all the simulations that were exploited in this study.

The data extracted from MC simulation (Figure 4-16) don't allow an accurate definition of the scattering origin. Nevertheless, in the energy range of the particle therapy, a first order fit on the MC dataset provides a relation between the scattering origin depth and the range compensator thickness, for any incident particle of range R, as following:

$$z'/l = 0.322 + 0.023 \times l/R$$

Equation 4-1

Equation 4-1 is used as the definition of the z' function in model E (see Table 3-1).

Depth dependency:

This paragraph studies the linearity of the models B, C, D and E at alternative depth parameters, in order to determine the depth parameter that provides the most linear response. In Table 4-4 are reported the residual values and their standard deviation from linear fits based on 56 MC simulations (see Appendix C1, E = [40-220] MeV) of the function $\sigma(z_a) = k.z_a$, the z_a parameters tested for linearity being respectively z, $z + l$, $z + z'_{RC}$ and $z + z'$ for models B, C, D and E. The z' is empirically extracted from Figure 4-16 and z'_{RC} is defined in Figure 3-10.

Figure 4-16

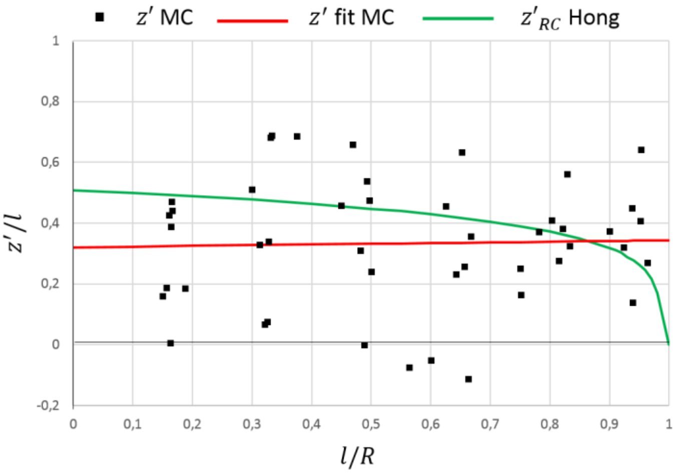

z'/l values extracted from 46 MC simulations (Appendix C1). The red line reports the fit realized on the MC data and is empirically defined as the function $z'/l = 0.322 + 0.023 \times l/R$. The reported green line represents the experimental scattering origin depth z'_{RC} defined by Hong in model A.

Table 4-4

Model	B	C	D	E
Linearity parameter z_a	z_0	$z_0 + l$	$z_0 + z'_{RC}$	$z_0 + z'$
$\frac{var(SDRE)}{< SDRE >}$	1.52 ± 2.18 %	2.91 ± 4.31 %	0.52 ± 0.71 %	0.46 ± 0.57 %

Relative residuals over the SDPBP value for the linear fits of the 4 models B, C, D and E based on the 56 MC simulations of Appendix C1.

The small relative residuals of the four models in Table 4-4 confirms the linearity of the models with distance for the four models B, C D and E:

$$\sigma_{rc}(E, l, z) = \theta(E, l). z_a$$

Equation 4-2

with θ the characteristic scattering angle of the range compensator for energy E and range compensator thickness l. The best linearity was found for model E, associated to the depth parameter $z_0 + z'$. The θ function is determined in the next paragraph for the four models.

Energy and range compensator thickness dependency - f_1 and f_2 determination:

In section 3.3.A.5, the sensitive parameters to the output SDPBP computation were determined as being the depth z (previous paragraph), the incident energy E and the relative thickness of the range compensator l/R. The $\theta(E, l)$ function in Equation 4-2 corresponds to the product $f_1(E) \times f_2(l/R)$ as defined in Table 3-1. The values of $\theta(E, l)$ were extracted from the entire dataset reported in Appendix C1, for a large range of energies (40 MeV – 220 MeV) and range compensators thicknesses from 0 to R. These results are reported in Figure 4-17 for the four models B, C, D and E.

Figure 4-17

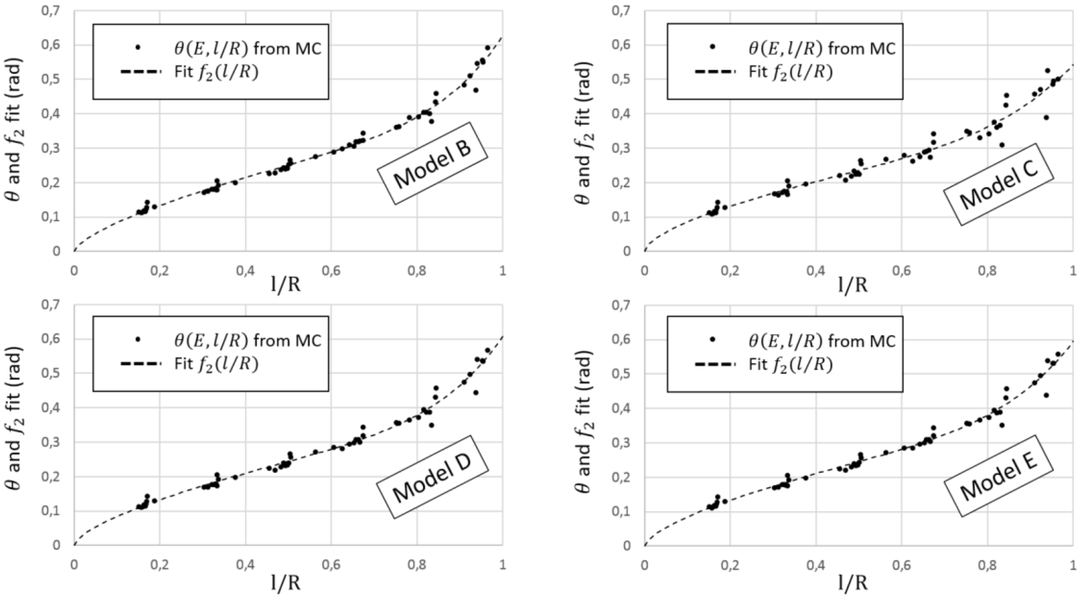

$\theta(E, l)$ values extracted from MC simulations (Appendix C1) and reported for different energies from 40 MeV to 220 MeV and different range compensator thicknesses for the four models B, C, D and E. The different fits for the $f_2(l/R)$ function is also showed as a dotted line for each model.

As the experimental data reported in Figure 4-17 for $\theta(E, l)$ are well aligned and show the same tendency for all energies, it confirms that the SDPBP energy dependency is very weak and that the empirical separation of $\theta(E, l)$ into the product of two functions $f_1(E)$ and $f_2(l/R)$ as a suitable approximation. The $f_2(l/R)$ fit, numerically determined in the next paragraph for all energies, is also reported on Figure 4-17.

On the different analytic models tested to fit the whole dataset of $\theta(E, l)$ presented in Figure 4-17, the one providing the lowest residual values is:

$$\begin{aligned}\theta(E, l) &= f_1(E) \times f_2\left(\frac{l}{R}\right) \\ &= (f_{1a}.E^2 + f_{1b}.E + f_{1c}) \times \left(f_{2a}.\left(\frac{l}{R}\right)^{f_{2b}} + f_{2c}\left(\frac{l}{R}\right)^{f_{2d}}\right)\end{aligned}$$

Equation 4-3

the numerical constants for f_{1a}, f_{1b}, f_{1c}, f_{2a}, f_{2b}, f_{2c} and f_{2d} were determined by a Generalized Reduced Gradient (GRG) non-linear and multi-parameters solving method, provided by the Excel data analysis add-in tool. Table 4-5 reports these numerical constants fitted on the whole dataset of Appendix C1, including the associated Chi-2 value, for the four models B, C, D and E. The $f_1(E)$ and $f_2(l/R)$ functions are respectively plotted in Figure 4-18 and Figure 4-17.

As seen on Figure 4-18, for energies in the range of 80-220 MeV the energy dependency of f_1 is weak (<4%) for the four models, confirming that f_2 can be considered as the characteristic angle θ as a first approximation. Nevertheless, the four models built in this study consider both function f_1 and f_2 in the statistical validation of this model realized in the next paragraph.

Table 4-5

Model	f_{1a}	f_{1b}	f_{1c}	f_{2a}	f_{2b}	f_{2c}	f_{2d}	Chi-2
B	$5.336\ 10^{-6}$	$-1.838\ 10^{-3}$	1.135	$3.996\ 10^{-1}$	$6.807\ 10^{-1}$	$2.276\ 10^{-1}$	7.037	$7.75\ 10^{-3}$
C	$3.796\ 10^{-6}$	$-2.097\ 10^{-3}$	1.199	$3.555\ 10^{-1}$	$6.164\ 10^{-1}$	$1.875\ 10^{-1}$	5.753	$8.07\ 10^{-3}$
D	$4.797\ 10^{-6}$	$-1.979\ 10^{-3}$	1.165	$3.828\ 10^{-1}$	$6.594\ 10^{-1}$	$2.245\ 10^{-1}$	6.883	$7.53\ 10^{-3}$
E	$4.742\ 10^{-6}$	$-1.918\ 10^{-3}$	1.158	$3.833\ 10^{-1}$	$6.570\ 10^{-1}$	$2.118\ 10^{-1}$	6.528	$7.57\ 10^{-3}$

Optimized numerical constants f_{1a}, f_{1b}, f_{1c}, f_{2a}, f_{2b}, f_{2c} and f_{2d} fitted on the entire dataset of Appendix C1 for the four models B, C, D and E, associated to their Chi-2 value representing the model discrepancies.

Figure 4-18

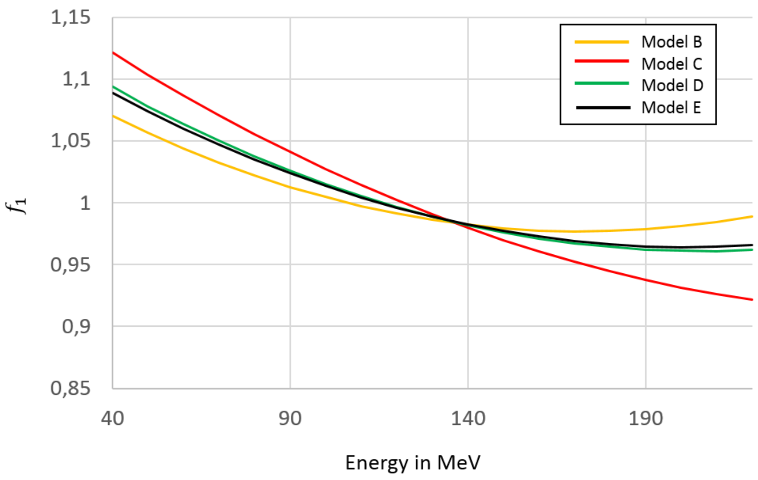

$f_1(E)$ optimized functions for the four models B, C, D and E, based on the whole MC simulation dataset reported in Appendix C1.

Sigma prediction assessment:

The models B, C, D and E were semi-empirically built in the previous paragraph. Table 4-6 reports the statistic errors of the models when compared to the 280 MC measurements of the dataset. Figure 4-19 shows the histograms of the relative discrepancy of the SDPBP induced by a PMMA range compensator, for the Hong model [70] (model A) and the best model of this study (model E). Instead, Table 4-7 show the global responses of the five different models (from A to E) based, this time, on 20 MC independent SDPBP measurements realized with random input parameters ($E \in [40; 220]\ MeV$, $t/R \in [0; 1]$ and $z \in [0; 150]\ cm$, see Appendix C2 for details).

Table 4-6

Model	A	B	C	D	E
Relative discrepancies $<\Delta\sigma/\sigma> \pm \mathrm{stdev}(\Delta\sigma/\sigma)$	-8.08 ± 5.62 %	-1.59 ± 4.90 %	2.81 ± 6.55	0.35 ± 3.43 %	0.11 ± 3.42 %

Relative systematic errors and relative random errors of the five models (from A to E) based on 280 SDPBP measurements in air realized by Monte Carlo (table from Appendix C1).

Figure 4-19

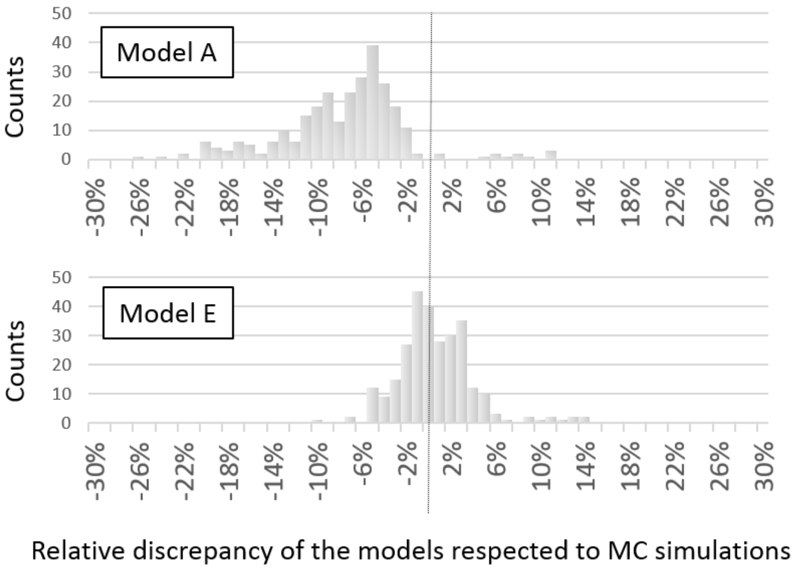

Histogram of the relative discrepancies of the SDPBP assessments based on the 280 measurements reported in Appendix C1, for the Hong model (model A) and the best model of this study (model E).

Table 4-7

Model	A	B	C	D	E
Relative discrepancies <Δσ/σ> ± stdev(Δσ/σ)	-6.69 ± 7.68 %	-1.61 ± 3.32 %	1.05 ± 3.36%	-0.30 ± 1.77 %	-0.56 ± 1.96 %

Assessment of the models responses based on independent measurements for 20 new configurations generated with random input parameters. The reference SDPBPs are calculated by MC simulations.

Proton dose distributions in water with half range compensator:

This paragraph deals with the dose reconstruction in broad beam conditions with the presence of a range compensator. The dose in a homogeneous water phantom was computed in a 10 cm × 10 cm field, the left half of the beam being attenuated by 3 cm of PMMA, the right part being range compensator-free. The other initial conditions of the particles (direction, energy, histories…) are identical to the dose computations realized in section 4.A.2.3. Figure 4-20 shows the 2D colorwash ODV computed by the CGS algorithm (associated to the model E) compared against MC simulations. On Figure 4-21 are reported the MC and Plastimatch lateral dose profiles at different depths (20 mm, 40 mm and 50 mm) extracted from Figure 4-20.

Figure 4-20

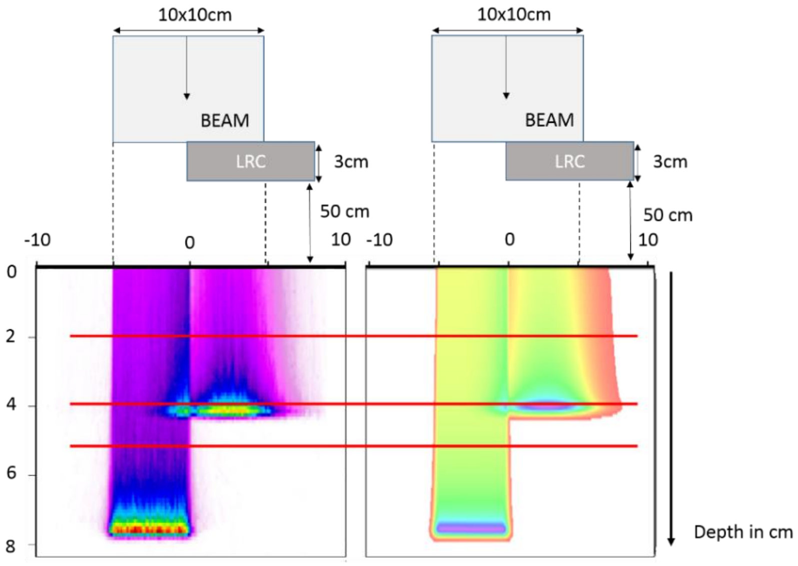

ODV computed by Plastimatch and MC simulations in a semi-infinite water phantom. The right half of the beam was attenuated by a 3 cm PMMA range compensator, the left part being open. The source distance to the phantom surface was 200 cm the range compensator was at 50 cm from the phantom surface. The incident proton energy was set to 100 MeV.

Figure 4-21

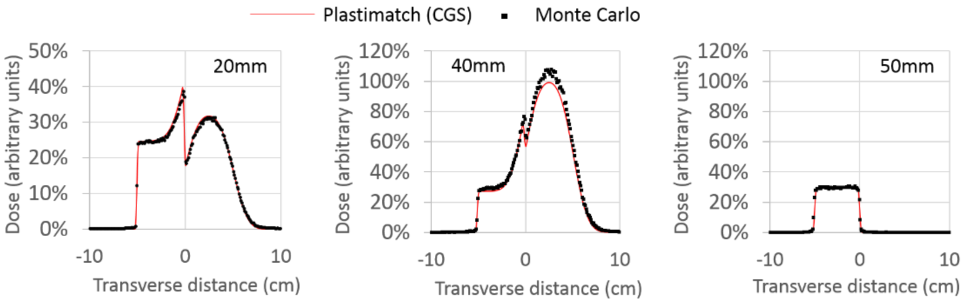

Lateral dose profiles extracted from the 2D ODV representation in Figure 4-20 at different depths (20 mm, 40 mm and 50 mm) for MC simulations (black squares) and the Plastimatch-CGS-Model E algorithm (red plain line).

4.B.1.2 *Improvement of the model for the estimation of the SDPBP induced by scattering in homogeneous and heterogeneous media*

The new differential model based on the Kanematsu expression of the scattering power along the beamlet axis was defined in section 3.3.B.4. In the following paragraphs, a study of the accuracy of this model is reported in particular cases where the Highland/Hong water pencil beam model scaled to WED failed: homogenous non water equivalent media and general heterogeneous materials.

Beam spread in homogeneous non water equivalent media:

Figure 4-22 showed that in non-water equivalent media like cortical bones, the Hong's method failed to compute correct SDPBPs due to the scattering in the media. The Kanematsu's differential definition of the scattering power in each voxel crossed by the beamlet axis was integrated in the beam spread computation algorithm, according to the method explained in section 3.3.B.4. The SDPBP computation in water and cortical bones are reported in Figure 4-22, which is to be compared to the same results computed by the Highland/Hong Approach (HHA) in Figure 4-8.

Figure 4-22

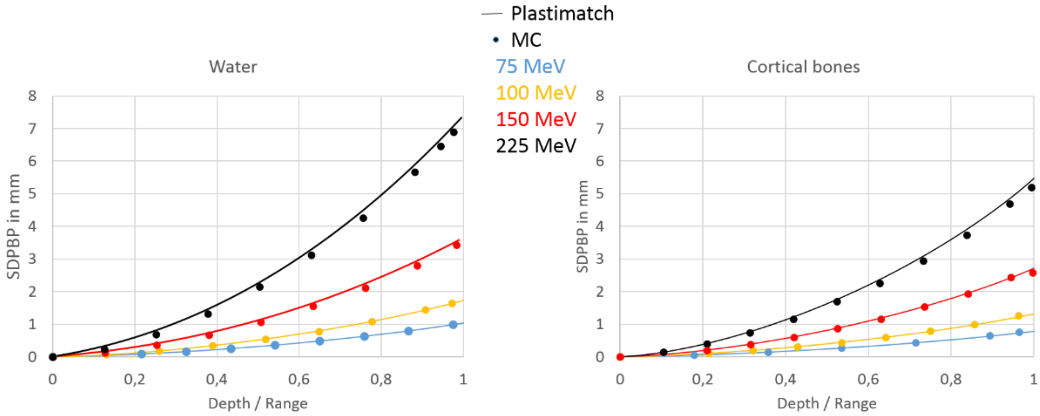

Evolution of the SDPBP in homogeneous media: in water (left) and in cortical bones (right) for SDPBP model based on the Kanematsu's differential definition of the scattering power of materials, for protons of 75, 100, 175 and 225 MeV.

Beamlet spread in heterogeneous media – Air gaps in water phantom:

One of the aims of Part B was the development of a pencil beam algorithm accounting for any type of medium, including heterogeneities, with a better accuracy than the HHA based on WED scaling. In order to investigate the performance of the differential approach in heterogeneous media, water phantoms were created as shown in Figure 4-23. In this experiment, the water phantom is divided in two parts: a 5 cm slab of water is placed on the top of an air gap of different widths (from 0 cm (configuration A) to 10 cm (configuration F)). The lateral dose measurements are realized at depth of 2.5 cm in the second, lower part of the water phantom. In all these configurations, the distance source – measurement depth is constant.

Figure 4-23

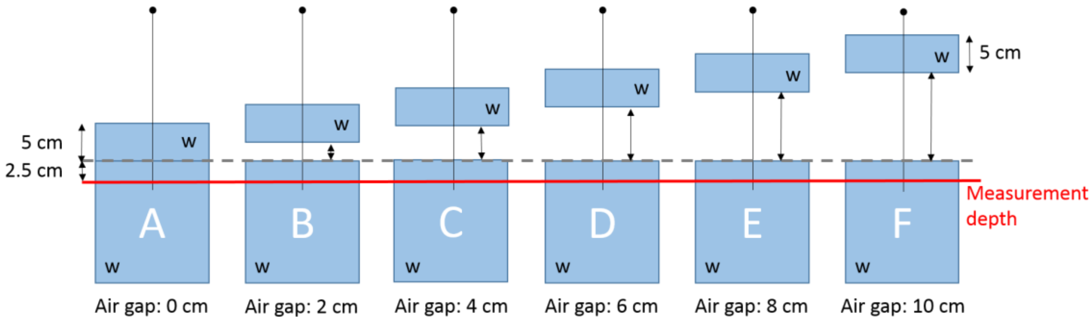

100 MeV beamlet spread assessment in water in five different air gaps configurations. From left to right the air gap width increases from 0 cm to 10 cm. The beamlet spread is evaluated from lateral dose profiles in the lower water block at a depth of 2.5 cm beyond the air gap.

Figure 4-24 (left) reports the SDPBP computation by Plastimatch algorithms (HHA and Differential Scattering Power Approach (DSPA)) and the SDPBP measurements on MC simulations in the same conditions, when the different air gap widths are crossed. Figure 4-24 (right) shows the consequences of the lateral off-axis descriptions (HHA or DSPA) on the global dose distributions in broad beam configurations when an important air gap is introduced in the medium.

Figure 4-24

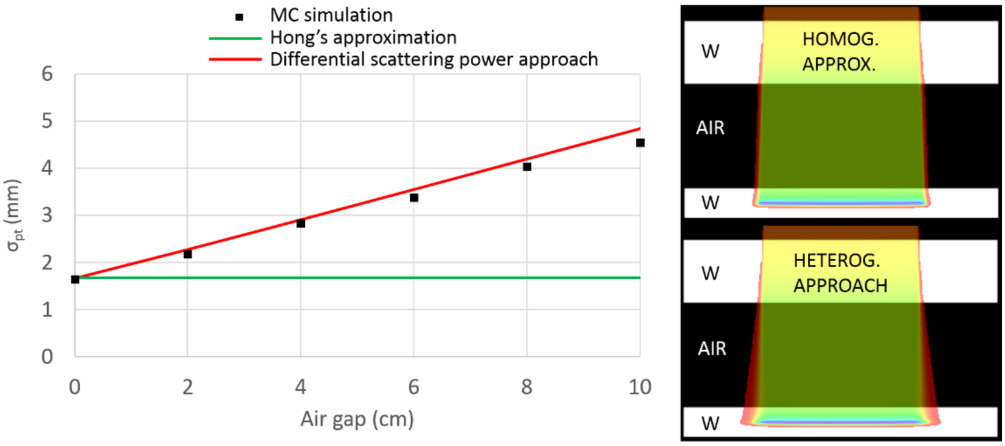

Left: SDPBP computed for a single 100 MeV proton pencil beam by Plastimatch for the HHA and the DSPA for different air gaps as shown on Figure 4-23. Right: Consequences on the final ODV between the two beamlet spread computations in the configuration D of Figure 4-23.

Beamlet spread in heterogeneous media – Cortical bone slab in a water phantom:

To demonstrate the fact that the particle history can have a significant effect on the beamlet spread broadening, a slab of 8 cm of cortical bones is inserted in a water phantom at different depths as shown on Figure 4-25. The SDPBPs for a single 200 MeV proton beamlet are extracted from lateral dose distributions at a physical depth of 19.5 cm (WED = 26.3 cm) from MC simulations and ODV computed by the Plastimatch algorithms HHA and DSPA.

Figure 4-25

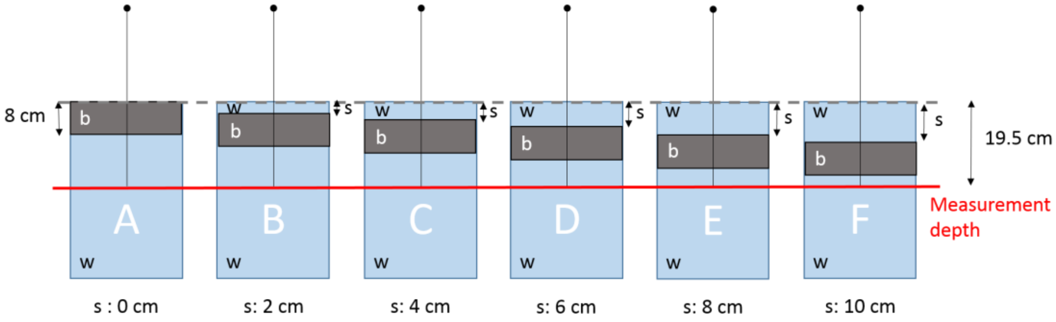

Six different configurations for the evaluation of the SDPBP at a physical depth of 19.5 cm (red line). In all these configurations, the WED crossed are equal. The layer of cortical bones ($\rho = 1.85\ g.cm^{-3}$) is 8 cm wide, the rest of the phantom being filled with water.

Figure 4-26

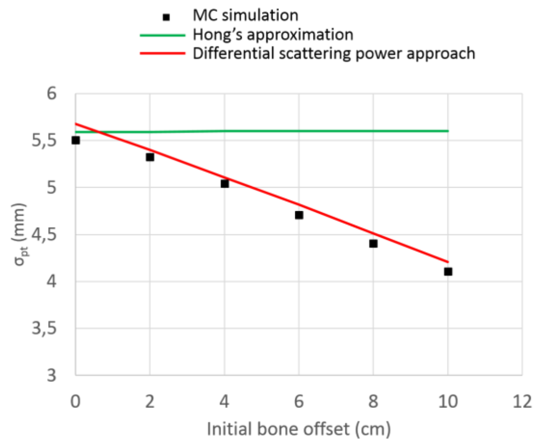

SDPBP computed by Plastimatch (HHA – green and DSPA –red) and measured by MC simulations at 19.5 cm depth in the different configurations of Figure 4-25, for a 200 MeV proton beamlet.

Global proton dose distributions in heterogeneous phantoms in broad beam conditions:

The last dosimetric validation of the study is the confrontation with MC simulations of a global ODV computed in a heterogeneous phantom by the DSPA implemented in Plastimatch. In this study, the heterogeneous phantom was built as explained in Figure 4-27, by introducing air gaps and cortical bone blocks in a water phantom. The field is squared: 6 cm × 6 cm at the phantom entrance. The source distance to the entrance phantom was set at 200 cm, and the initial energy of the proton beam was 110 MeV.

Figure 4-27

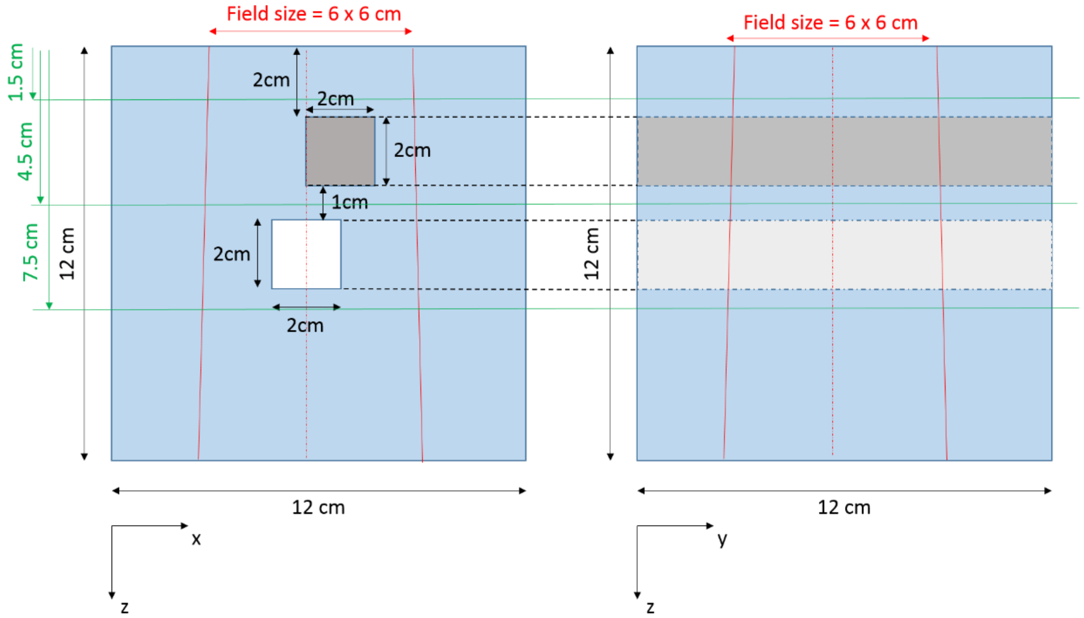

Heterogeneous phantom geometry. The white parallelepiped is made of air, the grey one is made of cortical bone. The phantom resolution is 1 mm × 1 mm × 1 mm.

The 2D ODV maps measured by MC simulations and computed by the CGS calling the DSPA are reported in Figure 4-28. Moreover, three lateral dose profiles are plotted in

Figure 4-29, at three different depths, as indicated on Figure 4-27 and their associated gamma-index scores (2.5%-2.5 mm) are reported in Table 4-8. The lateral dose distributions were computed by the RT, CGS, DGS and HGS (calling the DSPA), and also measured by MC simulations. The computation time for RT, CGS, DGS and HGS were respectively 7 seconds, 180 seconds, 1008 seconds and 159 seconds.

Figure 4-28

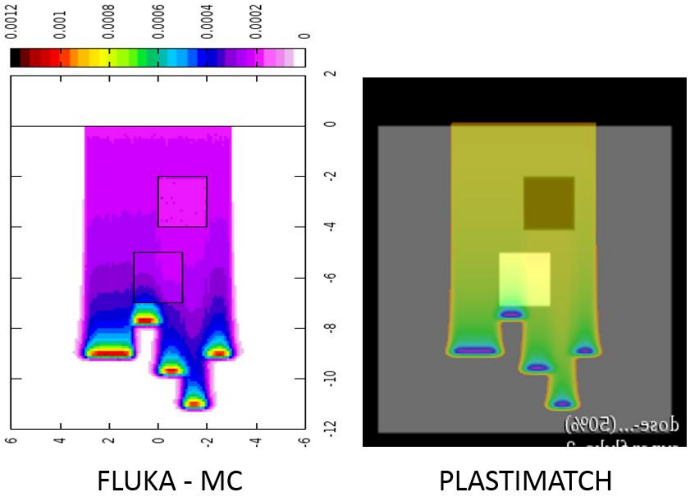

FLUKA - MC

PLASTIMATCH

2D map on the (xOz) *plan for a 110 MeV proton broad beam. On the left, an ODV created by MC simulations, on the right the ODV computed by Plastimatch with the CGS algorithm calling the DSPA (pencil beam spacing: 0.25 mm × 0.25 mm).*

Figure 4-29

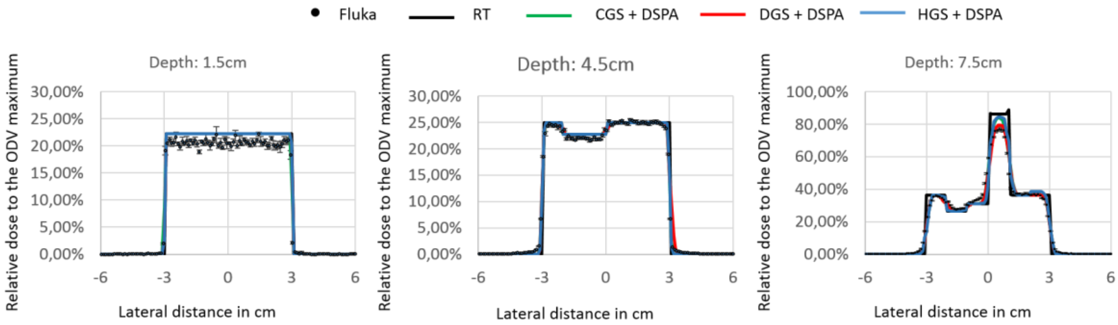

Depth dose profiles at 1.5 cm, 4.5 cm and 7.5 cm depth (from left to right) in the ODV 2D map shown in Figure 4-28 for the four Plastimatch algorithms: RT, CGS, DGS and HGS, calling the DSPA.

Table 4-8

Gamma index scores	Depth = 1.5cm	Depth = 4.5cm	Depth = 7.5cm	Depth = 7.5cm (3%-3mm)
RT	100.0%	99.2%	80.2%	85.1%
CGS + DSPA	99.2%	100.0%	92.6%	95.9%
DGS + DSPA	100.0%	99.2%	95.9%	99.2%
HGS + DSPA	100.0%	98.3%	87.6%	92.6%

1D gamma-index scores (2.5%-2.5 mm) at 1.5 cm, 4.5 cm and 7.5 cm for the four dose reconstruction algorithms when compared to MC simulations lateral profiles.

4.B.2 Discussion – *The beam spread correction*

4.B.2.1 Improvement of the model for the estimation of the SDPBP induced by the scattering in a PMMA range compensator

Beam spread dependency on distance from the range compensator:

The measurement of the infinitesimal beamlet spread after passing through a range compensator showed that the SDPBP is not directly proportional to the distance from the downstream face of the range compensator, but linear with an effective origin of the scattering located in the second part of the range compensator ($z'/l < 0.5$). This result confirmed the model proposed by Hong [70] about the position of the effective origin (z'_{RC}) even if the accuracy of the MC simulations were not sufficient to elaborate a precise model (Figure 4-16). Model E (based on the origin of the scattering model built on the SDPBP MC measurements) corresponds to a slightly better linearity with depth than the Hong's model approach, but the difference on the response of the two models is not sufficient to displace Hong's definition of the origin of the scattering. This difference is likely due to the difference in the SDPBP estimation accuracy from our dataset and the measurements realized by Hong for the definition of z'_{RC}. Nevertheless, the main conclusion of this paragraph is that Table 4-4 showed that the beamlet spread due to a range compensator can be considered as linear with both z' and z'_{RC}.

Beam spread dependency on the particle energy and range compensator thickness:

On the total dataset, the lowest discrepancies between the SDPBP measured by MC simulations and the SDPBPs computed by the five models (A-E) were found for models D and E with respectively 0.35 ± 3.43% and 0.11 ± 3.42% of average error. Table 4-6 shows that the Hong's model (model A) is not as accurate as the four models developed in this study in the case of the computation by MC simulations of the SDPBP induced by a PMMA range compensator, due to a different description of the f_1 and f_2 (respectively θ_0 and γ in the Hong's study) functions. Table 4-7 showed that when independent data (i.e. data not used for the creation of the models) of SDPBPs measured on MC simulations (Appendix C2) are compared to the 5 models, models D and E are again the most accurate in this study, the average error being in the order of 0.5% ± 1.9%. This confirms that these 2 models can be easily used for any energy, range compensator thickness and distance in the parameter range explored in this study.

Model D and E are the most complex models to implement, but the simpler models proposed in this study (like model B) are also good approximations, if the user considers the average error to be expected by the models, shown in Table 4-7. These results established that model E, numerically defined above (Equation 4-4), represents to date the better MC-based model describing the pencil beamlet spread induced by a PMMA range compensator.

$$\sigma_{rc}(E, l, z(cm)) = f_1(E) \times f_2(l/R) \times \left(z_0 + z'(l, E)\right) \; in\, mm$$

with,

$$\frac{z'}{l} = 0.023 \times \frac{l}{R} + 0.332,$$

$$f_1(E) = (4.742 \times 10^{-6}.E^2 - 1.918 \times 10^{-3}.f_{1B}.E + 1.158)$$

$$and$$

$$f_2(l/R) = \left(3.833 \times 10^{-1}.\left(\frac{l}{R}\right)^{0.6570} + 2.118 \times 10^{-1}\left(\frac{l}{R}\right)^{6.528}\right)$$

Equation 4-4

Validation of the range compensator computation in broad beam conditions:

In the case of dose distributions reconstructed in the presence of a range compensator, the results reported in Figure 4-20 and Figure 4-21 were satisfying. This example reaches a gamma index score (1D gamma-index, 2.5%/2.5 mm) for the CGS algorithm of 97.0% at 20 mm depth, 89.1% at 40 mm depth and 99.0% at 50 mm depth. This result validates the dose computation algorithm when a range compensator is introduced in the beam line. On Figure 4-21, it is clear than the lateral dose profiles extracted from ODV computed by Plastimatch match very well with the MC simulations ODV, for both blocked and free part of the beam, except at the Bragg peak depth which is the most critical area of the beam from a dosimetric point of view. Indeed, the 2.5%-2.5 mm 89.1% score at this depth might be considered as a failing score, but the dose varies with a high gradient on the depth axis and the score for 3%-3 mm gamma index analysis is much better: 95.5%.

4.B.2.2 Improvement of the model for the estimation of the SDPBP induced by scattering in homogeneous and heterogeneous media

The differential scattering power approach validation in homogeneous media:

In this study, the differential approach of the scattering power proposed by Kanematsu (see section 3.3.B.4) was applied to the off-axis term of the pencil beamlet model implemented in Plastimatch. Figure 4-22 confirmed that this approach provides good results in homogeneous media (water and bones) for energies in the particle therapy range. If the accuracy of the DSPA is similar in water to the HHA mentioned in Part A, section 4.A.1.7, in non-water equivalent materials, like cortical bones, the DSPA is much more accurate. The maximal characteristic scattering angle is correctly computed and confirmed by MC simulations, which was not the case for the WED scaled HHA in Figure 4-8.

The differential scattering power approach validation in heterogeneous media:

Figure 4-24 and Figure 4-26 clearly showed that in the presence of medium heterogeneities (like air gaps or water-cortical bones heterogeneities) the DSPA is much more accurate than the homogeneous HHA when compared to MC simulations. These two examples clearly showed that when the position and the composition of each voxel along the pencil beamlet axis (see Equation 3-7) is considered, the beamlet spread is much better computed than a WED-scaled water pencil beam approach, and shows a very good agreement with MC simulations.

Figure 4-24 and Figure 4-26 were chosen to highlight that the new DSPA for computing the pencil beamlet spread implemented in Plastimatch is very efficient and accurately accounts for the material variations along its axis in a much better way than the reference HHA.

The differential scattering power approach validation in broad beam conditions:

The 2D ODV maps measured by MC simulations and computed by the CGS calling the DSPA are reported in Figure 4-28. Moreover, three lateral dose profiles are plotted in Figure 4-29, at three different depths, as indicated on Figure 4-27 and their associated gamma-index scores (2.5%-2.5 mm) are reported in Table 4-8. The lateral dose distributions were computed by the RT, CGS, DGS and HGS (calling the DSPA), and also measured by MC simulations. The computation time for RT, CGS, DGS and HGS were respectively 7 seconds, 180 seconds, 1008 seconds and 159 seconds.

Figure 4-28 is the last validation of this study. This example takes the example of a heterogeneous phantom made of water, air and cortical bones, and assesses the accuracy of the dose reconstruction of the four models proposed in this study when the DSPA is called. This phantom is expected to reproduce situations occurring in a real patient. The dose overestimation of the ODV from Plastimatch when compared to MC simulations at 1.5 cm (see Figure 4-29, left) is clearly due to an overestimation of the Bortfeld analytic model at low depths (see Figure 4-13). This systematic error would be eliminated by the implementation of experimental depth dose profiles (or coming from MC simulations in our case).

The 1D gamma-index scores (2.5%-2.5 mm) based on the profiles of Figure 4-29 and reported in Table 4-8 for the three different depths explored in this study are very satisfying at 1.5 cm and 4.5 cm (gamma-index scores > 98.3%) but might seem unsatisfying at 7.5 cm depth (gamma-index <95% for CGS and HGS). As these 1D gamma-index scores don’t consider any longitudinal gradients in the Bragg peak area, a 2D gamma index analysis would provide higher scores. Moreover, when a 3%-3 mm gamma-index analysis is realized to the 7.5 cm depth profiles, the gamma-index scores rise to acceptable values (gamma-index > 95% for CGS and DGS, see Table 4-8). These quantitative results confirm that the CGS and DGS methods associated with the DSPA algorithm provide satisfying ODVs in agreement with the aims of Part A and Part B of this report even in complex configurations like heterogeneous phantoms.

4.C Results – Part C

4.C.1 Results – Part C – *The software interface*

4.C.1.1 The interface

The next paragraphs give a short overview of the treatment planning modalities implemented in the SlicerRt add-in toolkit. The next figures (from Figure 4-30 to Figure 4-32) report the screenshots of the sub-module interfaces available helping the user in the treatment planning process. The TPS interface is accessible in the “Radiotherapy” module, under the name “External Beam Planning”.

The Treatment plan module:

In this module are defined the different general parameters associated to the whole plan like the plan name, the input CT-images (DICOM) name, the dose volume contours (also called *skin contours*) or the DCE called for the dose computation (for this project: Plastimatch) – see Figure 4-30 (top).

The prescription module:

This module contains the input parameters defining the dose prescription, like the definition of the target volume, the dose prescription, the reference dose point or the type of beam selected for therapy (for this project: protons) – see Figure 4-30 (bottom).

Figure 4-30

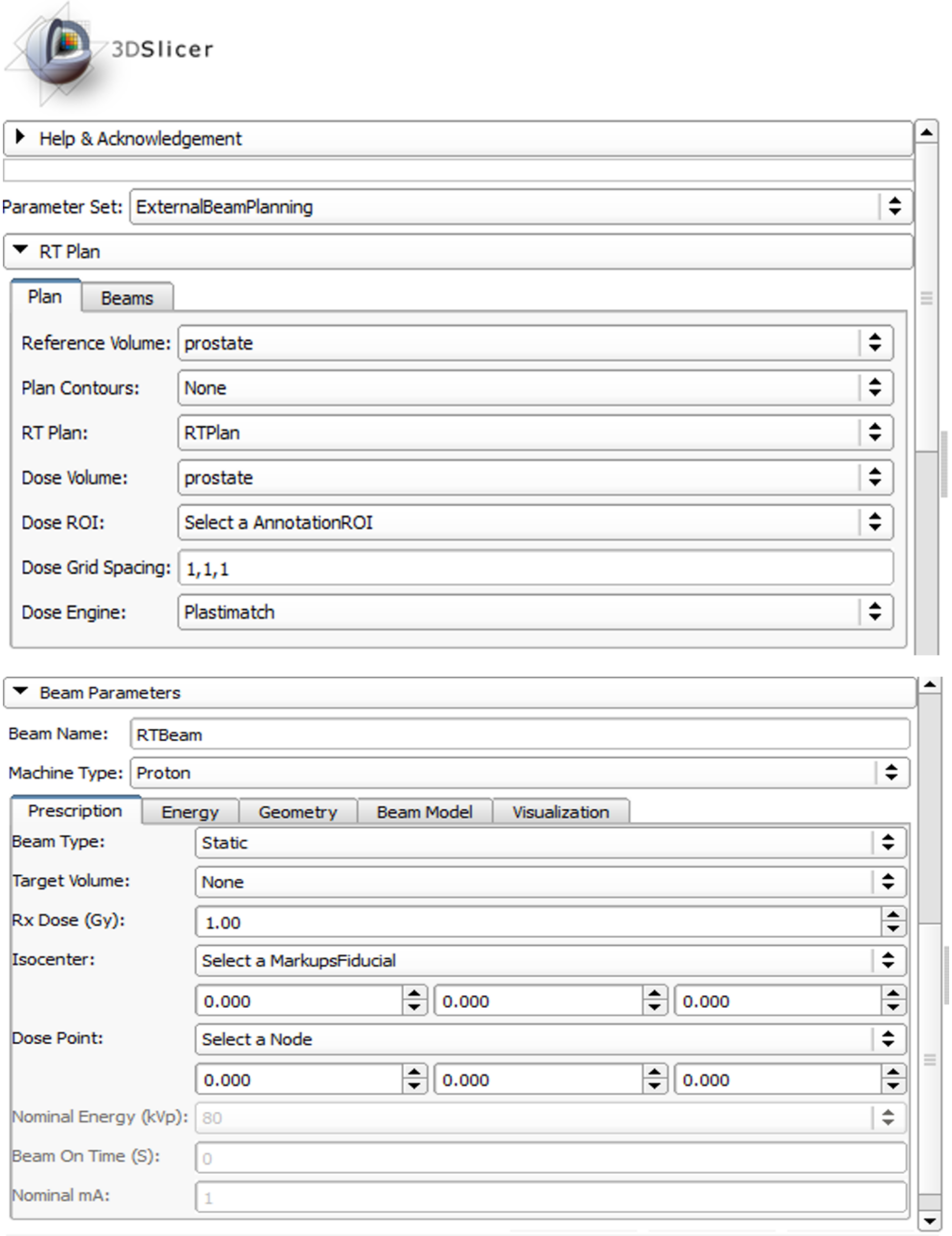

Parameter Set: ExternalBeamPlanning

Reference Volume: prostate
Plan Contours: None
RT Plan: RTPlan
Dose Volume: prostate
Dose ROI: Select a AnnotationROI
Dose Grid Spacing: 1,1,1
Dose Engine: Plastimatch

Beam Name: RTBeam
Machine Type: Proton

Beam Type: Static
Target Volume: None
Rx Dose (Gy): 1.00
Isocenter: Select a MarkupsFiducial
0.000 0.000 0.000
Dose Point: Select a Node
0.000 0.000 0.000
Nominal Energy (kVp): 80
Beam On Time (S): 0
Nominal mA: 1

Top: the treatment plan module. Bottom: the prescription module

The beam geometry module:

For each beam, an associated beam geometry module is accessible in the beam parameters window. This module contains the geometric parameters for the definition of a single beam like the beam angle, the field size, or the beam weight. When one of these parameters is changed, the beam visualization overlapped on the CT-images is automatically updated with the new parameters (Figure 4-31). For multiple-beams treatment planning, the user must select the specific beam in the plan tree diagram to access this module.

The energy module:

This module specifies the margins to be applied around the target volume in the longitudinal direction (proximal and distal margins, linked to the SOBP creator tool) and in the lateral direction (smearing, linked to the collimator and range compensator creator tools) – see Figure 4-32 (top).

The beam model module:

The beam model module encloses the beam line and algorithm settings, required as input parameters by the DCE like the source position and size, the aperture distance or the algorithm called for dose computation (for example RT, CGS, DGS or HGS) – see Figure 4-32 (bottom).

Figure 4-31

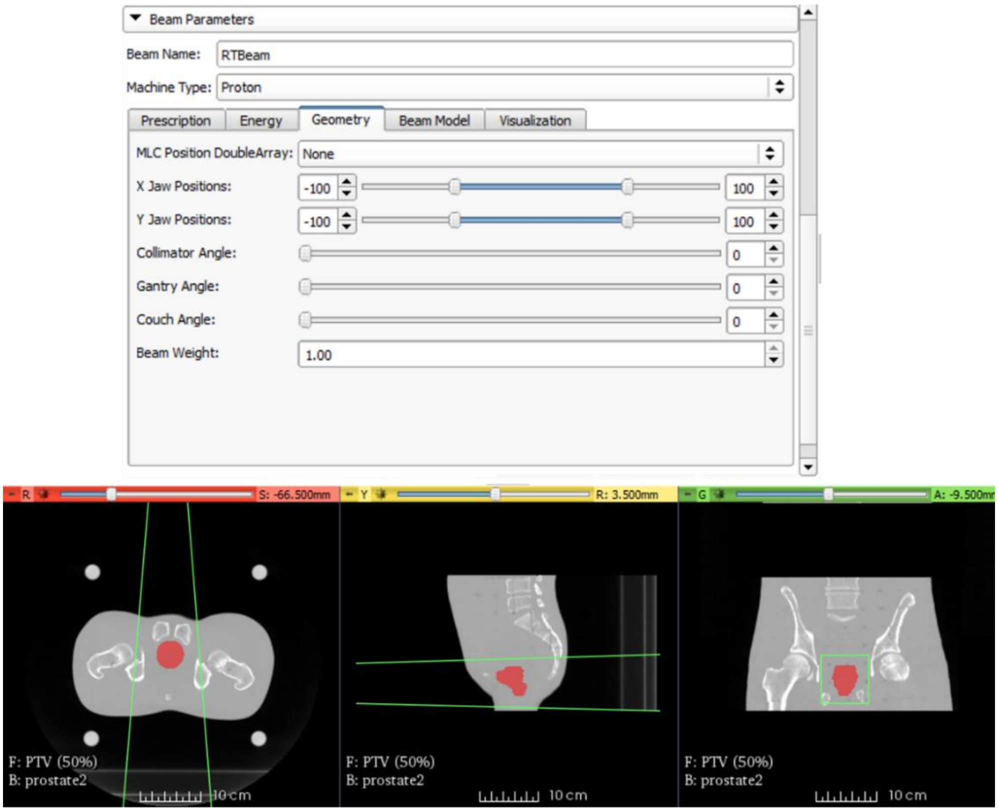

Beam Name: RTBeam
Machine Type: Proton
MLC Position DoubleArray: None
X Jaw Positions: -100 100
Y Jaw Positions: -100 100
Collimator Angle: 0
Gantry Angle: 0
Couch Angle: 0
Beam Weight: 1.00

Top: the beam geometry module. Bottom: the 3D geometry of the beam defined in the "beam geometry module" is observable on the 3D Slicer image visualization interface.

Figure 4-32

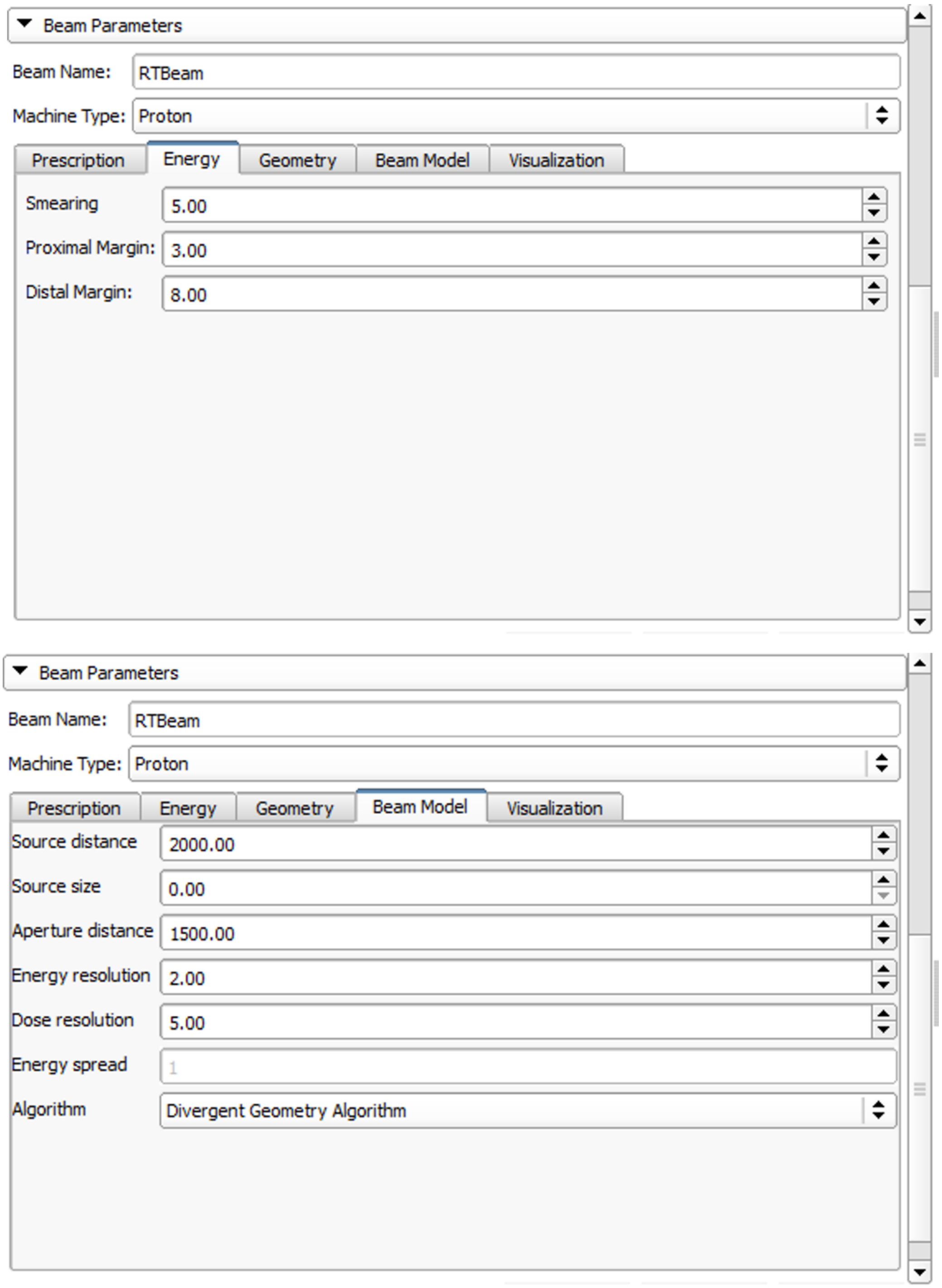

Beam Name: RTBeam
Machine Type: Proton
Smearing 5.00
Proximal Margin: 3.00
Distal Margin: 8.00

Beam Name: RTBeam
Machine Type: Proton
Source distance 2000.00
Source size 0.00
Aperture distance 1500.00
Energy resolution 2.00
Dose resolution 5.00
Energy spread 1
Algorithm Divergent Geometry Algorithm

Top: the energy module, bottom: the beam model module

In order to highlight the capacities of the SlicerRt toolkit dedicated to treatment planning, two treatment planning examples are presented in the following paragraphs: a prostate treatment plan with two lateral, opposite beams, and a brain treatment plan with two tilted beams.

4.C.1.2 *Example 1: a prostate treatment plan*

Figure 4-33 represents the final visualization of a prostate treatment plan process. The plan was built with two contralateral, equally weighted proton beams (50%-50%), and automatically shaped from the definition of the target volume and its associated 3D margins (5 mm of longitudinal and lateral margins). As expected, the entire target volume is covered by the at least 95% of the dose prescription and the surrounding tissues are spared, confirming that the automatic tools computing collimators, range compensators and SOBPs are correctly implemented, as announced in section 4.A.1.4.

Figure 4-33

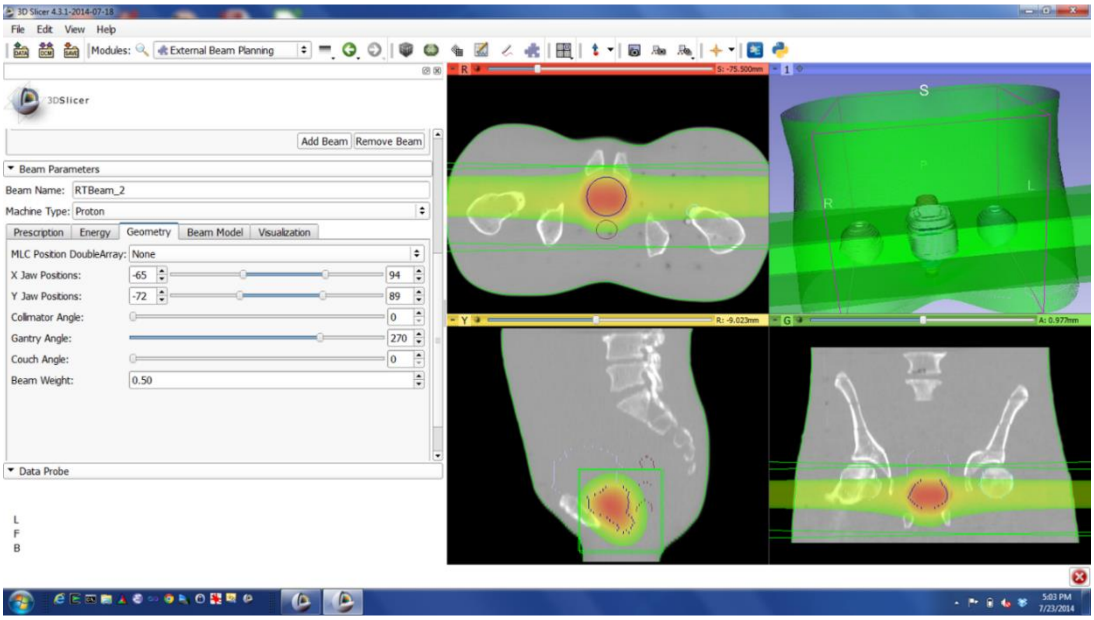

Beam Name: RTBeam_2
Machine Type: Proton
MLC Position DoubleArray: None
X Jaw Positions: -65 94
Y Jaw Positions: -72 89
Collimator Angle: 0
Gantry Angle: 270
Couch Angle: 0
Beam Weight: 0.50

Software interface overview showing the overlapping of the ODV computed by Plastimatch on the associated input CT-images for a prostate treatment plan. The target volume is represented in blue. The SOBPs, collimators and range compensators associated to each beam of the plan were automatically created by Plastimatch.

4.C.1.3 *Example 2: a brain treatment plan*

As in the previous paragraph, the TPS implemented in the SlicerRt toolkit can also be used for any localization, like the brain region. Figure 4-34 shows the visualization of the ODV computed by Plastimatch overlapped on the input CT-images. The dosimetry was performed with two orthogonal beams, the posterior beam being slightly tilted. 5 mm margins were applied around the target volume and the SOBPs, collimators and range compensators associated to each beam were automatically computed.

Figure 4-34

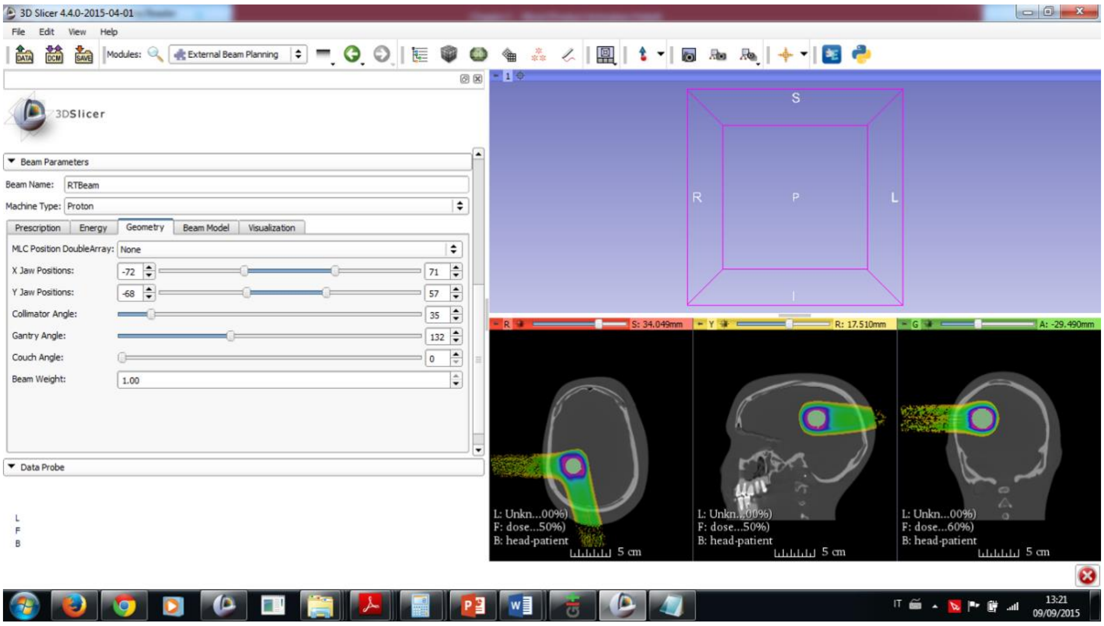

Beam Name: RTBeam
Machine Type: Proton
MLC Position DoubleArray: None
X Jaw Positions: -72 71
Y Jaw Positions: -68 57
Collimator Angle: 35
Gantry Angle: 132
Couch Angle: 0
Beam Weight: 1.00

Software interface overview for the example of a brain treatment plan. The ODV is shown on a colorwash scale and overlapped on the input CT-images. The target volume is represented in white.

4.C.2 Discussion – Part C – *The software interface*

In Part C, we don't consider any dosimetric validation, as this part was already developed in Part A and B during the validation of the Plastimatch algorithms for the entire beam line. The SlicerRt toolkit calls the DCE for creating the ODV associated with the parameters set for the different modules introduced in section 4.C.1.1. Two examples of treatment plans were realized with the TPS implemented in SlicerRt for two common tumor sites requiring protontherapy treatments (prostate and brain). These examples, associated to the beam line model validated in Part A and dose validation in Part B, demonstrate that the open-source TPS developed during this project can be used to create basic proton treatment plans.

The interface helps the user in the definition of the input parameters required for the dose computation process at two levels: for the passively scattered beam line model and the definition of specific settings describing the treatment plan configuration. The implemented tools for the automatic creation of the beam-limiting and beam-modifier devices and SOBP conformed to a target volume were successfully developed and provide a homogeneous and well conformed coverage of any target volume in any heterogeneous phantom. Finally, the representation of the colorwash ODV overlapped on the input CT-images helps the users in the optimization of the treatment plan settings, and allows a 3D dosimetric validation of the associated treatment plan. This TPS doesn't need any particular prerequisites on the input CT-images volume and can be used at any tumor location, including pelvis, chest, head & neck, or extremity.

Finally, the user must not forget that this proton TPS software was not validated for clinical treatments, but was developed with the aim of helping research groups in the particle therapy field.

4.D Future of the project and applications

This thesis has explained in detail how a basic proton beam line was modeled in the 3D Slicer software. Nevertheless, a full TPS is more complex than the results obtained during this PhD project. The next paragraphs give a short overview of improvements that could be developed in the future to make this software more comprehensive.

- Implementation of an active scanning beam line: all the dosimetric tools required for the implementation of an active scanning beam line were already developed for the dose calculation involved in a passively scattered beam line. A particle number spot map for each monoenergetic beam frame may be added to describe accurately each beam, as shown in Figure 1-26. The four algorithms could be adapted to this beam line setup.[1]
- The SOBP optimizers are based on depth dose curves in water, but not adapted to the target volume heterogeneities. This algorithms could be adapted to even the dose inside any 3D target volume. This would particularly interesting for the case of an active scanning beam line.[2]
- The nuclear interactions were not described in the algorithms presented in this report. These interactions should be taken into account in the future, in particular thanks to the Knutson's work on the topic [40], especially for modeling active scanning beam lines. Nevertheless, the computation time will be longer as another pencil beam (nuclear halo) needs to be computed for each primary pencil beam describing the MCS occuring in the media.
- The PB model implemented in Plastimatch could be easily upgraded to ion beam lines by implementing:
    - the depth dose curves of the ions in the central axis term
    - an accurate description of the beamlet spreads considering the MCS of ions in materials and the associated nuclear interactions as described in section 2.5.6. This is the method used by the Siemens Syngo TPS dedicated to particle therapy.
- As the energy of the particle is tracked along the PB axis for the DSPA, this data could be used to create not only a physical dose distribution but also a radiobiological dose distribution in the ODV, by using the direct relation between energy and LET, associated to the relation between LET and RBE. The radiobiologic effect is very important for ions and a TPS dedicated to ion beam line must implement this option.

[1] -This improvement was not implemented at the time of the review of this report, but was implemented in Plastimatch at the time of the PhD manuscript submission and will be shown during the PhD defense.

[2] - This improvement is in progress at the time of the PhD manuscript submission.

The applications of the TPS we developed during the PhD project are numerous. This TPS could be helpful for dosimetry research in protontherapy, from treatment optimization processes to dose calculation verifications from an independent software. This TPS could also be used by conventional radiotherapy centers to compare photon dose distributions to proton dose distributions.

More generally, the Slicer TPS can be used for any kind of education and research in the particle therapy field or for teaching to medical physicists, dosimetrists, and radiation technicians.

5. GENERAL CONCLUSION

During this project, a basic passively scattered proton beam line has been modeled in order to compute accurate proton dose distributions in patients or phantoms. The consequences of beam-modifier devices introduced in the beam line was accurately assessed and mathematically described in the pencil beam theory from the source size to the scattering in the patient heterogeneities.

In part A, basic tools for automatic 3D dose shaping were successfully implemented by the combination of three different algorithms: the collimator automatic shaper, the range compensator creator and the SOBP optimizer. When combined, these three algorithms provide a homogeneous coverage of the target volume, including the margins set by the user. Moreover, well-known algorithms used in the commercial XiO TPS (Elekta) were implemented in Plastimatch for the model of the pencil beam spread due to the devices introduced in the beam line and due to the patient.

Three different dose summation methods were also developed in addition to the XiO Hong's method. These algorithms were evaluated in homogeneous phantoms and three of them (CGS, DGS and HGS) gave similar results when compared to MC simulations, the CGS method often being the faster algorithm.

The work developed in Part A contributed to implement a complete dose calculation engine in Plastimatch similar to the commercial TPS XiO's DCE, with low computation times thanks to the CGS algorithm. This finalized algorithm allowed us to reproduce the results published in the literature by its creator, still considered today as the reference dose computation algorithm.

In part B, an important effort was dedicated to the improvement of the lateral beamlet spread computation in different media to take particular account of the material compositions and eventual heterogeneities. In a study dedicated to the beamlet spread occurring in the PMMA range compensator, we showed that an analytical model can satisfyingly describe the off-axis term of the pencil beam model with an accuracy of 0.5% ± 1.9% (mean ± standard deviation) when the Hong's method, implemented in many pencil beam algorithms reached an accuracy of -6.69% ± 7.68% (mean ± standard deviation), when both are compared to measurements involving MC simulations. The results reported in this study showed that our PMMA-specific model for the computation of the beamlet spread due to a range compensator is easy and straightforward to be implemented in pencil beam algorithms, as a unique, analytic function considering only the three following parameters: the incident particle energy, the range compensator thickness and the distance of the point of interest from the scattering origin of the range compensator.

Moreover, we also developed a better description of the pencil beam lateral spread in patients based on a differential approach that considers the scattering power of the materials along the pencil beam axis. This differential model was found to be more accurate than the reference Hong’s homogeneous approximation, in particular when air gaps and heterogeneities are present in the patient. Finally this model accurately computes 3D dose distributions in any type of medium, whatsoever its geometrical configuration or composition and for any incident proton energy (in the particle therapy range: 40 MeV – 225 MeV).

In Part C an interface simulating a commercial TPS was built. This open-source software is implemented in the 3D Slicer software and connects the different setting modules to the Plastimatch DCE developed in part A and B. Moreover, this TPS allows the specific definition of a complete proton treatment plan, and the visualization of its associated dose volume on the input CT-image volume. An overview of the proton TPS capabilities was presented with two treatment plan examples (pelvis and brain).

All the data used for this report were computed by the algorithms implemented in Plastimatch and measured by MC simulations. The reader can easily reproduce any of the experimental data or the treatment plans built in this report. All the software requisites are downloadable online, open-source, free and multiplatform.

The association of the beam line model and the dose summation algorithms developed in Part A, the upgrade of the reference algorithms for the beam spread model elaborated in Part B, and finally the user-friendly interface implemented in the SlicerRt toolkit in Part C, make of this software a general tool covering a large range of potential applications suitable for research in the particle therapy field.

ACKNOWLEDGMENTS

This work was supported by the Federal Share of program income earned under NIH C06-CA059267.

I want to thank the Centro Nazionale di Adroterapia Oncologica (CNAO) of Pavia - Italy - for their general help and the useful access to the Monte Carlo calculation cluster in order to provide the accurate dose distributions used as golden standards in this PhD thesis.

6. REFERENCES

[1] B. Stewart and C. Wild, World Cancer Report, International Agency for Research on Cancer, 2014.

[2] Physician Characteristics and Distribution in the US Division, SROA Benchmarking Survey, 2004.

[3] G. Kraft, “Radiobiological effect of highly charged ions (Ch. 10)” in Physics of Highly and multiple charged ions, F.J Currel Kluwer Academic Publisher, 2002.

[4] C. Tobias et al., “Pituitary irradiation with high energy proton beams: a preliminary report” Cancer Res., vol. 18, pp. 121-134, 1958.

[5] D. Kramer, “Carbon-ion cancer therapy shows promise” Physics Today, vol. 68, no. 6, pp. 24-25, 2015.

[6] J. Sisterson, “Worldwide charged particle patient totals” Particles, vol. 23, p. 14, 1999.

[7] M. Jermann, “Particle therapy statistics in 2014” Int. J. of Particle Ther., vol. 2, no. 1, pp. 50-54, 2015.

[8] A. Koehler and W. Preston, “Protons in radiation therapy. Comparative dose distributions for protons, photons and electrons” Radiology, vol. 104, pp. 191-195, 1972.

[9] T. Terasawa et al., “Systematic review: charged-particle radiation therapy for cancer” Ann. Intern. Med., vol. 151, no. 8, pp. 556-565, 2009.

[10] M. Scholz, “Open questions in heavy ion clinical radiobiology” 2nd Workshop on Hadron Beam Therapy of Cancer May 20-27, 2011.

[11] A. M. Koelher, R. J. Schneider and J. M. Sisteron, “Range modulators for protons and heavy ions” Nucl. Instrum. Methods 131, pp. 437-440, 1975.

[12] C. Bert and M. Durante, “Particle radiosurgery: a new frontier of physics in medicine” Phys. Med. 30:5, pp. 535-538, 2 Jun 2014.

[13] F. Dilmanian, J. Eley and S. Krishnan, “Minibeam therapy with protons and light ions: physical feasibility and potential to reduce radiation side effects and to facilitate hypofractionation” Int J Radiat Oncol Biol Phys 92:2, pp. 469-474, 1 Jun 2015.

[14] B. Jones, “The case for particle therapy” vol. 79, 2006.

[15] G. Gademann, “Socio-economics aspects of hadrontherapy” in Hadrontherapy in Oncology. Proceedings of the First International Symposium on Hadrontherapy, Como, Italy, Elsevier Excepta Medica, 1994, pp. 59-66.

[16] M. Lodge et al., “A systematic literature review of the clinical and cost-effectiveness of hadron therapy in cancer” Radiotherapy and Oncology, vol. 83, pp. 110-122, 2007.

[17] E. Borloni, S. Rossi and R. Orecchia, “Il centro nazionale di adroterapia oncologica” Roma, 2012.

[18] E. Emanuel and S. Pearson, “It costs more, but is it worth more?” New York Times, p. The opinion pages, 03 01 2012.

[19] R. Langreth, “The $150 Million Zapper:Does every cancer patient really need proton-beam therapy?” Forbes Magazine, 03 09 2009.

[20] R. Orecchia, A. Zurlo, A. Loasses, M. Krengli, G. Tosi, S. Zurrida, P. Zucali and U. Veronesi, “Particle beam therapy (hadrontherapy): basis for interest and clinical experience” vol. 34, no. 4, 1998.

[21] G. Kraft and S. Kraft, “Research needed for improving heavy-ion therapy” N. J. Phys., vol. 11, no. 025001, 2009.

[22] A. Pella et al., “Commissioning and quality assurance of an integrated system for patient positioning and setup verification in particle therapy” Technol. Cancer Res. Treat., vol. 13, no. 4, pp. 303-314, 2014.

[23] M. Desplanques et al., “A comparative study between the imaging system and the optical tracking system in proton therapy at CNAO” J. Radiat. Res., vol. 54 , no. suppl. 1, pp. 129-135, 2013.

[24] M. Kramer and M. Scholtz, “Treatment planning for heavy-ion radiotherapy: calculation and optimization of biologically effective dose” Phys. Med. Biol., vol. 45, pp. 3313-3330, 2000.

[25] U. Amaldi, Hadrontherapy in the world proceedings of NUPECC, 1-18, 2001.

[26] D. Schultz-Ertner and T. Tsuji, “Particle radiation therapy using proton and heavier ion beams” J. Clin. Oncol., vol. 25, pp. 956-964, 2007.

[27] H. Tsuji et al., “Clinical results of carbon ion radiotherapy at NIRS” J. Rad. Res., vol. 48, pp. A1-A13, 2007.

[28] D. Schultz-Ertner et al., “Effectiveness of carbon ion radiotherapy in the treatment of skull-base chordomas” Int. J. Radiat. Oncol. Biol. Phys., vol. 68, pp. 449-457, 2007.

[29] M. Durante and J. Loeffler, “Charged particles in radiation oncology” Nat. Rev. Clin. Oncol., vol. 7, pp. 37-43, 2010.

[30] A. Staab et al., “Spot-scanning-based proton therapy for extracranial chordoma” Int. J. Rad. Oncol. Biol. Phys., vol. 81, pp. 489-496, 2011.

[31] M. Krengli and R. Orecchia, “Medical aspects of the National Centre for Oncological Hadrontherapy (CNAO) in Italy” Radiotherapy and Oncology, vol. 73, pp. S21-S23, 2004.

[32] M. J. Berger, J. S. Coursey, M. A. Zucker and J. Chang, “NIST Standard Reference Database 124 - Stopping-Power and Range Tables for Electrons, Protons, and Helium Ions” August 2005. [Online]. Available: http://www.nist.gov/pml/data/star/.

[33] R. Zirckle et al., “Exponential and sigmoid survival curves resulting from alpha and X irradiation of aspergillus spores” Journal of Cellular Physiology, vol. Supp. 39, pp. 78-85, 1952.

[34] E. Hall, Radiobiology for the Radiologist (fifth edition), Philadelphia: Lippincott Williams & Wilkins, 2000.

[35] M. Mori, “Study of the lateral dose profile for the treatment plans in hadrontherapy,” Università degli studi di Pavia, Pavia, 2014.

[36] P. Sigmund, Particle Penetration and Radiation Effects, Berlin Heidelberg: Springer Series in Solid State Science - Springer-Verlag, 2006.

[37] J. Turner, “Interaction of ionizing radiation with matter” Health Physics, vol. 86, no. 3, pp. 228-252, 2004.

[38] C. Maiorino, Studio degli effetti subletali indotti da radiazioni ad alto LET e diverso Z nell'ambito del progetto MiMo-BRAGG, Napoli: Università degli Studi di Napoli, 2012.

[39] D. Schardt et al., “Heavy-ion tumor therapy: Physical and radiobiological benefits” Reviews of Modern Physics, vol. 82, pp. 383-426, 2010.

[40] N. C. Knutson, “Evaluation of a proton pencil beam algorithm for dose calculation in heterogeneous media” Montana, 2012.

[41] G. Z. Molière, “Theorie der Streuung schneller geladener Teilchen II: Mehfach- und Vielfachstreuung” Z. Naturf. 3, pp. 78-97, 1948.

[42] G. Z. Molière, “Theorie der Streuung schneller geladener Teilchen. III. Die Vielfachstreuung” Z. Naturforsch. A 10, pp. 177-211, 1955.

[43] V. L. Highland, “Some practical remarks on multiple scattering” Nucl. Instrum. Methods 129, pp. 497-499, 1975.

[44] V. L. Highland, “Some practical remarks on multiple scattering - erratum” Nucl. Instrum. Methods 161, p. 171, 1979.

[45] B. Gottschalk, A. M. Koelher, C. S. Mayo and M. S. Wagner, “Multiple Coulomb scattering of 160 MeV protons” Nucl. Instrum. Method B 74, pp. 467-490, 1993.

[46] B. Gottschalk, “On the scattering power of radiotherapy protons” Med. Phys., vol. 37, no. 1, pp. 352-367, 2010.

[47] T. Puck and P. Marcus, “Action of the x-rays on mammalian cells” J. Exp. Med., vol. 103, no. 5, pp. 653-666, 1956.

[48] P. Mayles, A. Nahum and J. Rosenwald, Handbook of radiotherapy physics, Boca Raton: CRC Press, 2007.

[49] D. Goodhead, “Spatial and Temporal Distribution of Energy” Health Physics, vol. 55, pp. 231-240, 1988.

[50] M. Joiner, Basic Clinical Radiobiology, London: Arnold Publ., 2002.

[51] M. Raju, Heavy Particle Radiotherapy, New York: Academic Press, 1980.

[52] L. Skarsgard, Pion and Heavy Ion Radiotherapy, New York: Elsevier, 1983.

[53] J. Chavaudra, “Radiobiology” in Master of Medical Physics, Paris XI - France, 2006.

[54] M. Kadhim et al., “Transmission of chromosomal instability after plutonium alpha-particle irradiation” Nature, vol. 355, pp. 738-740, 1992.

[55] M. Mendonca, R. Antoniono and J. Redpath, “Delayed heritable damage and epigenetics in radiation-induced neoplastic transformation of human hybrid cells” Radiation Research, vol. 134, no. 2, pp. 209-216, 1993.

[56] T. Lindahl, “Quality control by DNA repair” Science, vol. 286, pp. 1897-1905, 1999.

[57] P. Peltomaki, “Deficient DNA mismatch repair: a common etiologic factor for colon cancer” Hum. Mol. Genet., vol. 10, pp. 735-740, 2001.

[58] T. Walsh et al., “Spectrum of mutations in BRCA2, BRCA2, CHEK2 and TP53 in families at high risk of breast cancer” Journal of the American Medical Association, vol. 295, no. 12, pp. 1379-1388, 2006.

[59] G. Steel, “Cellular sensitivity to low dose-rate irradiation focuses the problem of tumour radioresistance” Radiotherapy Oncology, vol. 20, pp. 71-83, 1991.

[60] A. Berington, S. Darby, H. Weiss and R. Doll, “100 years of observation on British radiologists: mortality from cancer and other causes 1897-1997” Br. J. Radiol., vol. 74, pp. 507-519, 2001.

[61] J. Cameron and J. Moulder, “Proposition: radiation hormesis should be elevated to a position of scientific respectability” Med. Phys., vol. 25, pp. 1407-1410, 1998.

[62] M. Belli et al., “RBE-LET relationship for the survival of V79 cells irradiated with low energy protons,” Int. J. Radiat. Biol., vol. 55, pp. 93-104, 1989.

[63] P. Todd, “Biological effects of heavy ions” in Symposium on Protection against radiation in space, NASA SP-71, US-gov printing office, A. Reetz, Editor, Washington, DC, 1965.

[64] G. Barendsen, “Current topics in radiation research” North Holland Pub., vol. 4, pp. 293-356, 1968.

[65] H. Paganetti et al., “Relative biological effectiveness (RBE) values for proton beam therapy” Int. J. Radiation Oncology Biol. Phys., vol. 53, pp. 407-421, 2002.

[66] W. Weyrather, “RBE for Track-segment irradiation in cell lines of differing repair capacity” Int. J. Radiat. Biol., vol. 75, pp. 1357-1364, 1999.

[67] M. Scholtz, “Oral presentation” in ESTRO Teaching Course, Heidelberg, 2008.

[68] R. Orecchia, P. Fossati and S. Rossi, “The national centre for oncological hadrontherapy: status of the project and future clinical use of the facility” Tumori, vol. 95, pp. 169-176, 2009.

[69] F. Kahn, The Physics of Radiation Therapy Fourth Edition, Philadelphia: Lippincott Williams & Wilkins, 2010.

[70] L. Hong, M. Goitein, M. Bucciolini, R. Comiskey, B. Gottschalk, S. Rosenthal, C. Serago and M. Urie, “A pencil beam algorithm for proton dose calculations” Phys. Med. Biol. 41, pp. 1305-1330, 1996.

[71] E. Pedroni, S. Scheib, T. Bohringer, A. Coray, M. Grossmann, S. Lin and A. Lomax, “Experimental characterization and physical modelling of the dose distribution of scanned proton pencil beams” Phys. Med. Biol. 50, pp. 541-561, 2005.

[72] D. Jones and A. Schreuder, “Magnetically scanned proton therapy beams: rationales and principles” Radiation Physics and Chemistry, vol. 61, pp. 615-618, 2001.

[73] A. Lomax, “Intensity modulation methods for proton radiotherapy” Phys. Med. Biol., vol. 44, pp. 185-205, 1999.

[74] A. Gemmel et al., “Biological dose optimization with multiple ion fields” Phys. Med. Biol., vol. 53, pp. 6991-7012, 2008.

[75] F. Bourhaleb et al., “A treatment planning code for inverse planning and 3D optimization in hadrontherapy” Computers in Biology and Medicine, vol. 38, pp. 990-999, 2008.

[76] D. Bonnett, “Current developments in proton therapy - review” Phys. Med. Biol., vol. 38, pp. 1371-1392, 1993.

[77] U. Linz, Ion Beams In Tumor Therapy, New York: Chapman & Hall, 1995.

[78] A. Lomax, “Intensity modulated proton therapy and its sensitivity to treatment incertainties 1: the potential effects of calculational uncertainties” Phys. Med. Biol., vol. 53, pp. 1027-1042, 2008.

[79] A. Chvetsov et al., “The influence of CT image noise on proton range calculation in radiotherapy planning” Phys. Med. Biol., vol. 55, pp. 141-149, 2010.

[80] J. Meyer et al., “Spot scanning proton beam therapy for prostate cancer: treatment planning technique and analysis of consequences of rotational and translational alignment errors” Int. J. Radiation Oncology Biol. Phys., vol. 78, pp. 428-434, 2010.

[81] S. Agostinelli et al., “Geant4 - a simulation toolkit” Nuclear Instruments and Methods in Physics Research A, vol. 506, pp. 250-303, 2003.

[82] A. Fasso et al., “FLUKA: status and perspective for hadronic applications” in Monte Carlo 2000 Conference, Lisbon, 2000.

[83] M. Berger, “Monte Carlo calculation for the penetration and diffusion of fast charged particles” Meth. Comp. Phys., vol. 1, pp. 135-215, 1963.

[84] W. Newhauser et al., “Monte Carlo simulations of the dosimetric impact of radiopaque fiducial markers for proton radiotherapy of the prostate” Phys. Med. Biol., vol. 52, pp. 2937-2952, 2007.

[85] P. Yepes, D. Mirkovic and P. J. Taddei, “A GPU implementation of a track-repeating algorithm for proton radiotherapy dose calculations” Phys. Med. Biol. 55, pp. 7107-7120, 2010.

[86] P. Yepes, S. Randeniya, P. J. Taddei and W. D. Newhauser, “A track repeating algorithm for fast Monte Carlo dose calculations of proton radiotherapy” Nucl. Technol. 168, pp. 334-337, 2009.

[87] P. Yepes, S. Randeniya, P. J. Taddei and W. D. Newhauser, “Monte Carlo fast dose calculator for proton radiotherapy: application to a voxelized geometry representing a patient wth prostate cancer” Phys. Med. Biol. 54, pp. N21-N28, 2009.

[88] T. Bortfeld and W. Schlegel, “An analytical approximation of depth-dose distributions for therapeutic proton beams” vol. 41, no. 8, 1996.

[89] M. Urie, M. Goitein, W. R. Holley and G. T. Y. Chen, “Degradation of the Bragg Peak due to inhomogeneities” Phys. Med. Biol. 31, pp. 1-15, 1986.

[90] K. R. Russel, A. Montelius and E. Grusel, “Dose calculations in proton beams: Range straggling corrections and energy scaling” Phys. Med. Biol. 40, pp. 1031-1043, 1995.

[91] P. L. Petti, “Differential pencil beam dose calculation for charged particles” Phys. Med. Biol. 19, pp. 137-149, 1992.

[92] M. Hollmark, J. Uhrdin, D. Belkié, I. Gudowska and A. Brahme, “Influence of multiple scattering and energy loss straggling on the absorbed dose distributions of therapeutic light ion beams: I. Analytical pencil beam model” Phys. Med. Biol. 49, pp. 3247-3265, 2004.

[93] J. O. Deasy, “A proton dose calculation algorithm for conformal therapy simulations based on Molière's theory of lateral deflections” Med. Phys. 25, pp. 476-483, 1998.

[94] H. Szymanowski et al., “Experimental determination and verification of the parameters used in a proton pencil beam algorithm” Med. Phys. 28, pp. 975-987, 2001.

[95] J. Chapman, “Proton beam dose calculations for homogeneous media” Lousiana, 2012.

[96] M. Lee, A. E. Nahum and S. Webb, “An empirical method to build up a model of proton dose distribution for a radiotherapy treatment-planning package” Phys. Med. Biol. 38, pp. 989-998, 1993.

[97] C. Lee, “A new proton dose calculation algorithm for radiotherapy” Indiana, 1994.

[98] K. R. Hogstrom, M. D. Mills and P. R. Almond, “Electron beam dose calculations” Phys. Med. Biol. 26, vol. 26, pp. 445-459, 1981.

[99] L. Eyges, “Multiple scattering with energy loss” Phys. Rev. 74, pp. 1534-1535, 1948.

[100] V. Bellinzona et al., “On the parametrization of lateral dose profiles in proton radiation therapy” vol. 5, 2015.

[101] M. Soukup, M. Fippel and M. Alber, “A pencil beam algorithm for intensity modulated proton therapy derived from Monte Carlo simulations” Phys. Med. Biol. 50, pp. 5089-104, 2005.

[102] B. Schaffner, E. Pedroni and A. Lomax, “Dose calculation models for proton treatment planning using a dynamic beam delivery system: an attempt to include density heterogeneity effects in the analytical dose calculation” Phys. Med. Biol. 44, pp. 27-41, 1999.

[103] E. Hug and J. Debus, “Teaching course” in ESTRO, Heidelberg, 2008.

[104] W. Scott, “The theory of small-angle multiple scattering of fast charged particles” Rev. Mod. Phys., vol. 35, pp. 231-313, 1963.

[105] A. Hanson et al., “Measurement of multiple scattering of 15.7 MeV electrons” Phys. Rev., vol. 84, pp. 634-637, 1951.

[106] M. Gupta, “Calculation of radiation length in materials” July 2010. [Online]. Available: Cdsweb.cern.ch.

[107] G. Lynch and O. Dahl, “Approximations to multiple Coulomb scattering”, Nucl. Instr. and Meth. in Phys. Res. B, vol. 58(1), pp. 6-10, 1991.

[108] E. Paganetti, Proton Therapy Physics, New York: CRC PRESS Taylor & Francis Book, 2012.

[109] S. Safai, T. Bortfeld and M. Engelsman, “Comparison between the lateral penumbra of a collimated double-scattered beam and uncollimated scanning beam in proton radiotherapy”, Phys. Med. Biol., vol 53(6), pp. 1729-1750, 2008.

[110] B. Rossi, High-Energy Particles, New York: Prentice-Hall, 1952.

[111] ICRU-35, “Radiation Dosimetry: Electron Beams with Energies Between 1 and 50 MeV” International Commission on Radiation Units and Measurements Report 35, 1984.

[112] N. Kanematsu, “Semi-empirical formulation of multiple scattering for Gaussian beam model of heavy charged particles stopping in tissue-like matter” Phys. Med. Biol. (unpublished), pp. x-x, 2008.

[113] U. Schneider et al., “On small angle multiple Coulomb scattering of protons in the Gaussian approximation” Z. Med. Phys., vol. 11, pp. 110-118, 2001.

[114] N. Kanematsu, “Alternative scattering power for Gaussian beam model of heavy charged particles” Nucl. Instrum. Methods B 266, pp. 5056-5062, 2008.

[115] B. Gottschalk, Passive beam spreading in proton radiation therapy, Unpublished book, available on line, 2004.

[116] S. Seltzer, An assessment of the role of charged secondaries from nonelastic nuclear interactions by therapy proton beams in water, NISTIR 5221, 1993.

[117] B. Schaffner, “Proton dose calculation algorithms and configuration data” in PTCOG 46- Education workshop, Wanjie, 2007.

[118] N. Kanematsu, S. Yonai, A. Ishizaki and M. Torikoshi, “Computational modeling of beam-customization devices for heavy-charged-particle radiotherapy” Phys. Med. Biol. 53, pp. 3113-3127, 2008.

[119] Plastimatch developers, “Plastimatch,” Plastimatch development team, 2010. [Online]. Available: Plastimatch development team. [Accessed 2015].

[120] G. C. Sharp and R. e. a. Li, “Plastimatch: An open source software suite for radiotherapy image processing” in Proceedings of the XVIth International Conference on the Use of Computers in Radiotherapy (ICCR), Amsterdam, the Netherlands, 2010.

[121] U. Schneider, E. Pedroni and A. Lomax, “The calibration of CT Hounsfield units for radiotherapy treatment planning” Phys. Med. Biol. 41, pp. 111-124, 1996.

[122] T. Bortfeld, “An analytical approximation of the Bragg curve for therapeutic proton beams” Med. Phys. 24, pp. 2024-2033, 1997.

[123] T. Bohlen et al., “The FLUKA Code: Developments and Challenges for high Energy and Medical Applications” Nuclear Data sheets, vol. 120, pp. 211-214, 2014.

[124] A. Ferrari, P. R. Sala, A. Fasso and J. Ranft, “FLUKA: a multi-particle transport code” CERN-2005-10, INFN/TC_05/11, SLAC-R-773, 2005.

[125] K. Parodi et al., “Clinical CT-based calculations of dose and positron emitter distributions in proton therapy using the FLUKA Monte Carlo code” vol. 52, no. 12, 2007.

[126] T. Tessonnier et al., “Development and application of tools for Monte Carlo based simulations in a particle beam radiotherapy facility” vol. 83, 2014.

[127] S. Molinelli et al., “Dosimetric accuracy assessment of a treatment plan verification system for scanned proton beam radiotherapy: one year experimental results and Monte Carlo analysis of the involved uncertainties” vol. 58, no. 11, 2013.

[128] G. Battistoni et al., “The FLUKA code: Description and benchmarking” vol. 896, 2007.

[129] The ROOT team, “Root Data Analysis Framework,” CERN, 1995. [Online]. Available: https://root.cern.ch. [Accessed 2015].

[130] R. Rademakers and F. Brun, “ROOT - An object Oriented Data Analysis Framework - Proceedings AIHENP'96 Workshop” Nucl. Inst. & Meth. in Phys. Res., vol. A 389, pp. 81-86, 1997.

[131] G. Ciangaru, J. C. Polf, M. Bues and A. R. Smith, “Benchmarking analytical calculations of proton doses in heterogeneous matter” Med. Phys. 32, pp. 3511-3523, 2005.

[132] H. Szymanowski and U. Oelfke, “Two dimensional pencil beam scaling an improved proton dose algorithm for heterogeneous media” Phys. Med. Biol. 47, pp. 3313-3330, 2002.

[133] M. Goitein, “A technique for calculating the influence of thin inhomogeneities on charged particle beams” Med. Phys. 5, pp. 258-264, 1978.

[134] M. Urie, M. Goitein and M. Wagner, “Compensating for heterogeneities in proton radiation therapy” Phys. Med. Biol. 29, pp. 553-566, 1983.

[135] N. Kanematsu et al., “A proton dose calculation code for treatment planning based on the pencil beam algorithm” Japan J. Med. Phys, pp. 88-103, 1998.

[136] 3D Slicer contributors, “3D Slicer,” [Online]. Available: http://www.slicer.org. [Accessed 23 July 2015].

[137] Slicer Laboratory, “SlicerRt,” The SlicerRT Community and the Percutaneous Surgery Laboratory, 2013. [Online]. Available: http://slicerrt.org. [Accessed 23 July 2015].

[138] C. Pinter et al., “SlicerRT: Radiation therapy research toolkit for 3D Slicer” Med. Phys., vol. 39, no. 10, pp. 6332-6338, 2012.

[139] K. Alexander et al., “Implementation of an efficient workflow process for gel dosimetry using 3D Slicer” Phys. Conf. ser. 573 012042, vol. Conf. ser. 573 012042, 2015.

[140] D. Groom, “Atomic and Nuclear Properties of Materials for more than 300 materials” Particle Data Group, 12 August 2014. [Online]. Available: http://pdg.lbl.gov/2014/AtomicNuclearProperties/. [Accessed 5 February 2015].

7. *APPENDICES*

Appendix A: Radiation length and proton stopping power ratio determination from Hounsfield Units

In this appendix, a method is proposed for the computation of radiation lengths and proton stopping power values from the Hounsfield Units (HU) of input Computed Tomography (CT)-images. In order to assess these two quantities, the CT-images have to be extracted from a correctly calibrated CT as mentioned in the Schneider’s publication [121].

A1. Radiation length determination

In this study, a simple function is proposed for the computation of a material radiation length from HU values. This estimation is necessary for a correct assessment of the proton beamlet spreads in heterogeneous media as shown in section 3.3.B.4. The radiation length scale for common materials vary on a large scale: from 30390 cm for dry air to 14.82 cm for cortical bones [140].

This fit of experimental data is based on two scientific contributions:

- The Schneider’s publication [121] was used to fit the HU of materials to their respective physical density ρ for media commonly used during CT calibrations and in the density range commonly found in patients and phantoms (from air to cortical bones).
- The Particle Data Group Website database [140] provides the radiation lengths and physical densities of different pure materials and compounds used for medical applications.

Based on these two databases, the following direct correlation was found between HU and radiation lengths X_0 (Figure Ap-7-1):

- For $HU \leq -1000,\ X_0 = 30390$
- For $-1000 < HU < 0,\ X_0 = \exp(3.727 \times 10^{-6} \times HU^2 - 3.009 \times 10^{-3} \times HU + 3.586)$
- For $0 \leq HU < 55,\ X_0 = -2.840 \times 10^{-2} \times HU + 36.08$
- For $HU \geq 55,\ X_0 = 9.803 \times 10^{-6} \times HU^2 - 2.894 \times 10^{-2} \times HU + 36.08$

Figure Ap-7-1

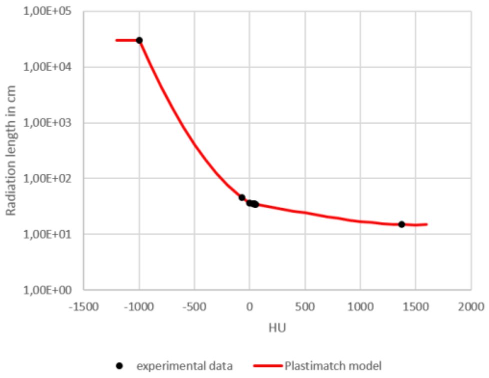

Radiation length model implemented in Plastimatch compared to experimental data [121] [140].

A2. Proton Stopping Power Ratio ($pSTPR_m$) determination

The determination of the $pSTPR_m$ values from HU number is more straightforward as Schneider provided a complete table [121] of these two quantities on a large scale of materials. Moreover, according to Figure 1-6, the $pSTPR_m$ values for a specific material are reasonably supposed to be constant in the particle therapy energy range (40-250 MeV).

Based on the Schneider's dataset, the following correlation was implemented in the Plastimatch algorithms for the computation of energy losses across heterogeneous materials. This model is invoked for both the determination of the water equivalent length in media and for the computation of proton pencil beamlet spreads. Figure Ap-7-2 shows the Plastimatch and XiO fits compared to the Schneider's publication.

- For $HU \leq -1000,\ pSTPR_m = 1.060 \times 10^{-3}$
- For $-1000 < HU < 0,\ pSTPR_m = HU \times \frac{1-1.060\times10^{-3}}{1000} + 1$
- For $0 \leq HU < 41.46,\ pSTPR_m = 1 + HU \times 1.174 \times 10^{-3}$
- For $HU \geq 41.46,\ pSTPR_m = 1.028 + HU \times 5.011 \times 10^{-4}$

Figure Ap-7-2

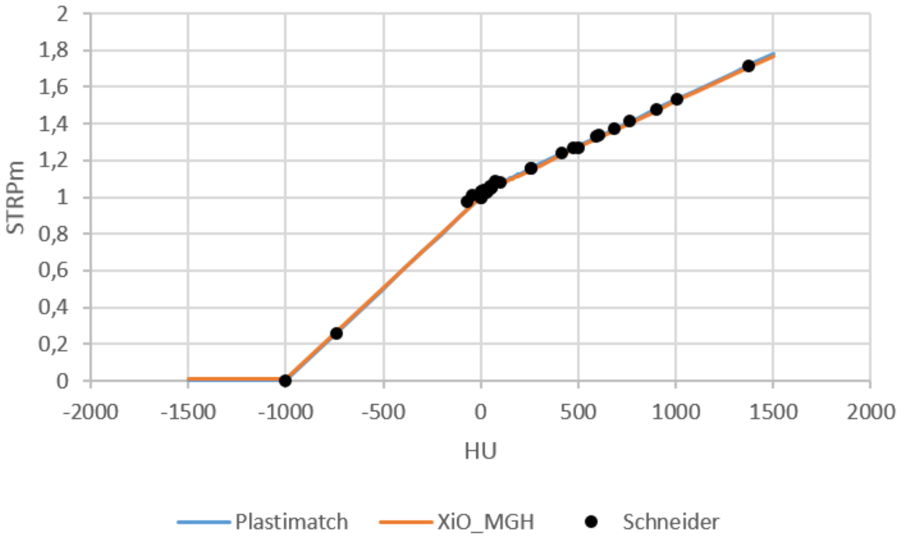

Plastimatch $pSTPR_m$ fits (blue line) based on experimental data from the Schneider database [121]. The $pSTPR_m$ model implemented in the XiO TPS (red line) is also represented for comparison.

APPENDIX B: THE CONFIGURATION FILE - INPUT PARAMETERS

This appendix reports the definition of the parameters to be declared in the input file, used to determine both the beam line model and the specific dose computation configuration. The input is decomposed into three different parts:

- the plan parameters, defined by the [PLAN] flag
- the beam parameters, defined by the [BEAM] flag
- the Bragg peaks parameters, defined by the [PEAK] flag

Figure Ap-7-3 shows the example of the input file format and the available flags for each of the 3 types of input parameters defined above.

Figure Ap-7-3

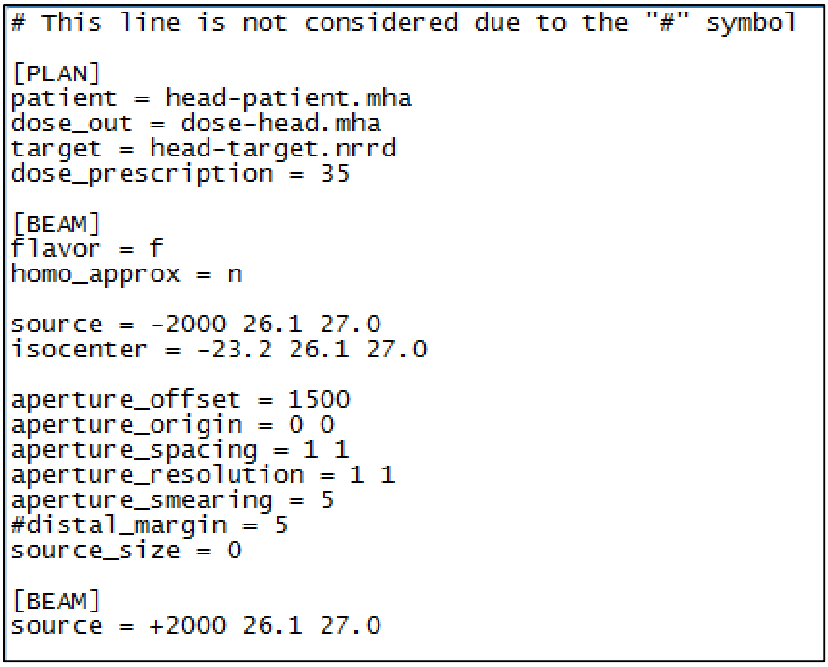

```
# This line is not considered due to the "#" symbol

[PLAN]
patient = head-patient.mha
dose_out = dose-head.mha
target = head-target.nrrd
dose_prescription = 35

[BEAM]
flavor = f
homo_approx = n

source = -2000 26.1 27.0
isocenter = -23.2 26.1 27.0

aperture_offset = 1500
aperture_origin = 0 0
aperture_spacing = 1 1
aperture_resolution = 1 1
aperture_smearing = 5
#distal_margin = 5
source_size = 0

[BEAM]
source = +2000 26.1 27.0
```

Input parameters file example for the definition of a specific dose calculation configuration (two opposite beams conformed on the head-target.nrrd target volume in the head-patient.mha input CT-images volume.

[PLAN] flags:

Flag	Example	Description
patient	volume.mha	File name of the input volume. CT-images, mha images…
target	PTV.nrrd	File name of the target volume
dose_out	dose.mha	File name for the output dose volume
dose_prescription	74	Prescription dose in Gy
dose_point	1 2 -2	3D position of the reference dose point for dose normalization (x, y, z) - in the room coordinates – in mm

[BEAM] flags:

The [BEAM] flag has a double function. It transfers to the Dose Computation Engine (DCE) the parameters associated to a definite beam but it also creates a new beam in the plan. Only parameters that are different from the previous beam can be defined: if one of the [BEAM] flags is not defined in the [BEAM] section, this flag is directly set to the previous beam value/string for the same flag. For the first beam definition, the unset input parameters are set to a default input value/string.

Flag	Example	Description
flavor	a f g h	Determines the type of algorithm used for the dose computation a = RT, f = CGS, g = DGS, h = HGS (see section x.x)
homo_approx	y n	y = Hong approximation for beam spread n = Differential scattering power approach for beam spread (see section x.x)
ray_step	1	Step length for the ray tracer tool – in mm
aperture_out	aperture.mha	File name for the output aperture image
rc_out	range_compensator.mha	File name for the output range compensator image
sigma_out	sigma.mha	File name for the output volume containing the lateral beam spread for each pencil beam
wed_out	wed.mha	File name for the output WED volume containing the WED value for each pencil beam
beam_weight	0.5	Weight of the beam in the plan
depth_dose_z_max	800	Maximal depth considered for the depth dose curve computation – in mm

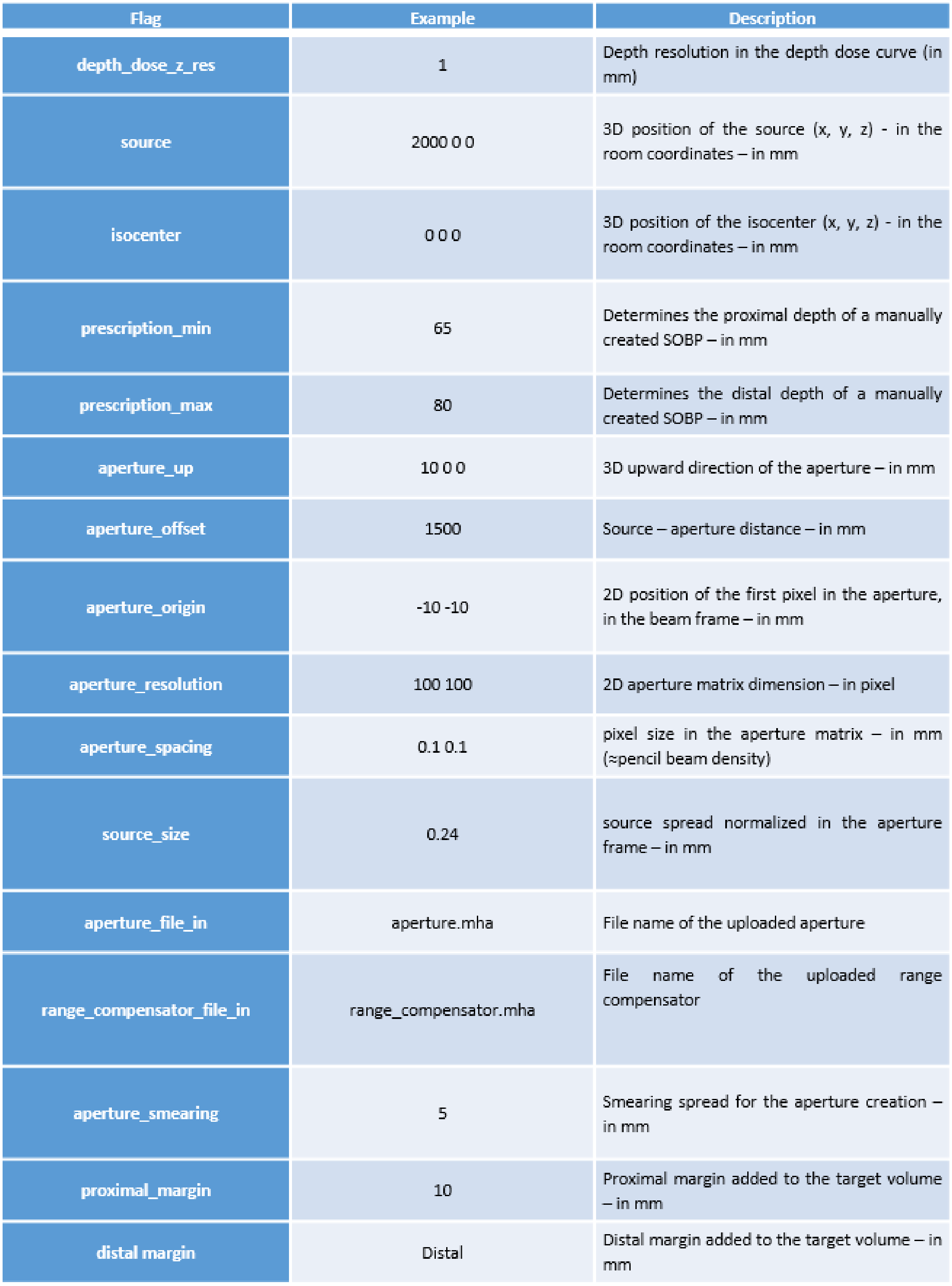

Flag	Example	Description
depth_dose_z_res	1	Depth resolution in the depth dose curve (in mm)
source	2000 0 0	3D position of the source (x, y, z) - in the room coordinates – in mm
isocenter	0 0 0	3D position of the isocenter (x, y, z) - in the room coordinates – in mm
prescription_min	65	Determines the proximal depth of a manually created SOBP – in mm
prescription_max	80	Determines the distal depth of a manually created SOBP – in mm
aperture_up	10 0 0	3D upward direction of the aperture – in mm
aperture_offset	1500	Source – aperture distance – in mm
aperture_origin	-10 -10	2D position of the first pixel in the aperture, in the beam frame – in mm
aperture_resolution	100 100	2D aperture matrix dimension – in pixel
aperture_spacing	0.1 0.1	pixel size in the aperture matrix – in mm (≈pencil beam density)
source_size	0.24	source spread normalized in the aperture frame – in mm
aperture_file_in	aperture.mha	File name of the uploaded aperture
range_compensator_file_in	range_compensator.mha	File name of the uploaded range compensator
aperture_smearing	5	Smearing spread for the aperture creation – in mm
proximal_margin	10	Proximal margin added to the target volume – in mm
distal margin	Distal	Distal margin added to the target volume – in mm

[PEAK] flag (Optional)

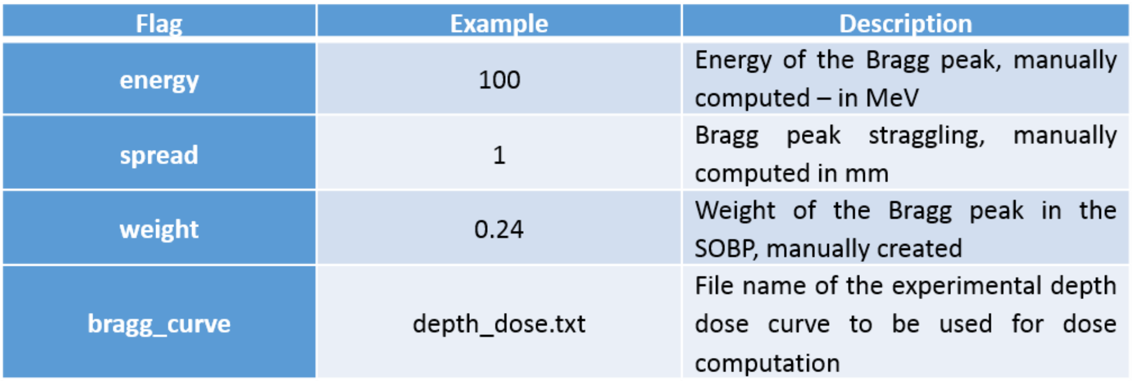

Flag	Example	Description
energy	100	Energy of the Bragg peak, manually computed – in MeV
spread	1	Bragg peak straggling, manually computed in mm
weight	0.24	Weight of the Bragg peak in the SOBP, manually created
bragg_curve	depth_dose.txt	File name of the experimental depth dose curve to be used for dose computation

APPENDIX C: STANDARD DEVIATION OF THE PENCIL BEAM PROFILE (SDPBP) CALCULATION BY MONTE CARLO METHODS

In this appendix are reported the SDPBP measured by Monte Carlo simulations, on which are based the new models for the determination and the validation of the SDPBP induced by scattering into a range compensator. The measurements were performed for different energies, range compensator thicknesses and distances from the range compensator.

C1. SDPBP estimation in air due to the scattering in different range compensators

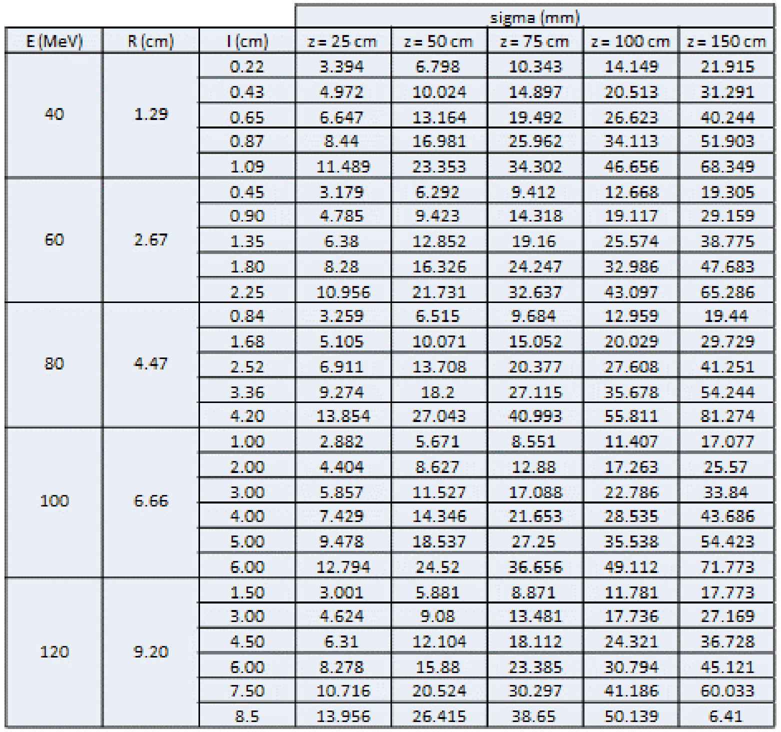

E (MeV)	R (cm)	l (cm)	sigma (mm)				
			z = 25 cm	z = 50 cm	z = 75 cm	z = 100 cm	z = 150 cm
40	1.29	0.22	3.394	6.798	10.343	14.149	21.915
		0.43	4.972	10.024	14.897	20.513	31.291
		0.65	6.647	13.164	19.492	26.623	40.244
		0.87	8.44	16.981	25.962	34.113	51.903
		1.09	11.489	23.353	34.302	46.656	68.349
60	2.67	0.45	3.179	6.292	9.412	12.668	19.305
		0.90	4.785	9.423	14.318	19.117	29.159
		1.35	6.38	12.852	19.16	25.574	38.775
		1.80	8.28	16.326	24.247	32.986	47.683
		2.25	10.956	21.731	32.637	43.097	65.286
80	4.47	0.84	3.259	6.515	9.684	12.959	19.44
		1.68	5.105	10.071	15.052	20.029	29.729
		2.52	6.911	13.708	20.377	27.608	41.251
		3.36	9.274	18.2	27.115	35.678	54.244
		4.20	13.854	27.043	40.993	55.811	81.274
100	6.66	1.00	2.882	5.671	8.551	11.407	17.077
		2.00	4.404	8.627	12.88	17.263	25.57
		3.00	5.857	11.527	17.088	22.786	33.84
		4.00	7.429	14.346	21.653	28.535	43.686
		5.00	9.478	18.537	27.25	35.538	54.423
		6.00	12.794	24.52	36.656	49.112	71.773
120	9.20	1.50	3.001	5.881	8.871	11.781	17.773
		3.00	4.624	9.08	13.481	17.736	27.169
		4.50	6.31	12.104	18.112	24.321	36.728
		6.00	8.278	15.88	23.385	30.794	45.121
		7.50	10.716	20.524	30.297	41.186	60.033
		8.5	13.956	26.415	38.65	50.139	6.41

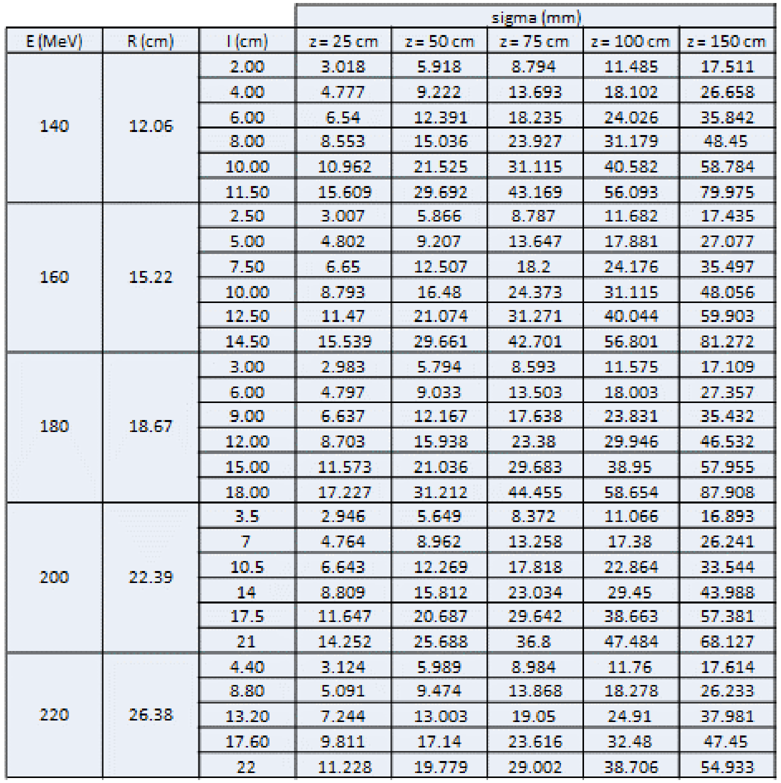

E (MeV)	R (cm)	l (cm)	sigma (mm)				
			z = 25 cm	z = 50 cm	z = 75 cm	z = 100 cm	z = 150 cm
140	12.06	2.00	3.018	5.918	8.794	11.485	17.511
		4.00	4.777	9.222	13.693	18.102	26.658
		6.00	6.54	12.391	18.235	24.026	35.842
		8.00	8.553	15.036	23.927	31.179	48.45
		10.00	10.962	21.525	31.115	40.582	58.784
		11.50	15.609	29.692	43.169	56.093	79.975
160	15.22	2.50	3.007	5.866	8.787	11.682	17.435
		5.00	4.802	9.207	13.647	17.881	27.077
		7.50	6.65	12.507	18.2	24.176	35.497
		10.00	8.793	16.48	24.373	31.115	48.056
		12.50	11.47	21.074	31.271	40.044	59.903
		14.50	15.539	29.661	42.701	56.801	81.272
180	18.67	3.00	2.983	5.794	8.593	11.575	17.109
		6.00	4.797	9.033	13.503	18.003	27.357
		9.00	6.637	12.167	17.638	23.831	35.432
		12.00	8.703	15.938	23.38	29.946	46.532
		15.00	11.573	21.036	29.683	38.95	57.955
		18.00	17.227	31.212	44.455	58.654	87.908
200	22.39	3.5	2.946	5.649	8.372	11.066	16.893
		7	4.764	8.962	13.258	17.38	26.241
		10.5	6.643	12.269	17.818	22.864	33.544
		14	8.809	15.812	23.034	29.45	43.988
		17.5	11.647	20.687	29.642	38.663	57.381
		21	14.252	25.688	36.8	47.484	68.127
220	26.38	4.40	3.124	5.989	8.984	11.76	17.614
		8.80	5.091	9.474	13.868	18.278	26.233
		13.20	7.244	13.003	19.05	24.91	37.981
		17.60	9.811	17.14	23.616	32.48	47.45
		22	11.228	19.779	29.002	38.706	54.933

C2. SDPBP calculation in air by Monte Carlo simulations (reference) and by models A, B, C, D and E with random input parameters

The input parameters were randomly generated in the following parameter ranges:

- $E \in [40; 220]\ MeV$
- $t/R \in [0; 1]$
- $z \in [0; 150]\ cm$

				Model (error % - estimation)				
E (MeV)	t/R (t, R - cm)	Z (cm)	SDRE (mm)	A	B	C	D	E
135.0	0.59 (6.68 / 11.32)	43.9	12.861	-7.85%	-4.39%	2.99%	-0.97%	-1.77%
101.9	0.60 (4.13 / 6.89)	66.0	19.257	-10.13%	-0.90%	0.46%	-0.24%	-0.39%
201.0	0.89 (20.12 / 22.6)	97.1	44.228	0.50%	1.16%	5.34%	2.55%	2.98%
113.6	0.76 (6.34 / 8.35)	63.4	23.408	-8.65%	-1.88%	1.82%	-0.50%	-0.47%
57.5	0.47 (1.16 / 2.47)	149.2	36.715	-15.28%	2.11%	0.77%	1.74%	1.73%
156.9	0.54 (7.95 / 14.73)	62.4	17.053	-8.58%	-4.96%	-1.24%	-2.98%	-3.63%
119.9	0.31 (2.85 / 9.18)	20.8	3.883	-10.29%	-4.26%	5.65%	0.71%	-0.82%
176.6	0.21 (3.80 / 18.08)	93.7	12.813	-6.95%	-1.27%	-2.03%	-1.49%	-1.41%
150.4	0.14 (1.92 / 13.47)	107.1	11.558	-5.07%	-3.72%	-2.16%	-3.35%	-2.97%
173.2	0.61 (10.66 / 17.49)	92.6	27.000	-6.01%	-2.10%	-0.90%	-1.42%	-1.64%
207	0.61 (14.45 / 23.77)	35.8	11.614	-5.26%	-11.61%	9.30%	-1.70%	-3.93%
213.4	0.31 (7.73 / 25.04)	147.9	25.364	22.23%	3.22%	-2.19%	1.32%	1.36%
77.6	0.70 (2.99 / 4.24)	124.7	42.333	-11.32%	0.91%	-0.45%	0.30%	0.52%
106.2	0.73 (5.44 / 7.41)	72.7	25.894	-9.73%	-1.77%	0.18%	-1.07%	-0.99%
99.5	0.22 (1.44 / 6.60)	103.2	14.622	-9.92%	0.57%	2.35%	1.25%	1.38%
97	0.81 (5.1 / 6.30)	48.3	19.689	-8.92%	-1.56%	3.11%	0.27%	0.22%
55	0.90 (2.05 / 2.28)	113.8	56.945	-14.14%	0.69%	-3.08%	0.13%	-0.54%
158.5	0.20 (3.03 / 14.97)	39.2	5.312	-6.58%	-2.83%	1.56%	-0.66%	-1.22%
87.9	0.54 (2.86 / 5.29)	52	13.730	-8.95%	2.23%	3.82%	3.11%	2.82%
218.2	0.14 (3.73 / 25.98)	104.7	11.230	-2.84%	-1.80%	-4.32%	-2.89%	-2.52
		Average ± standard deviation		-6.69% ± 7.68%	-1.61% ± 3.32%	1.05% ± 3.36%	-0.30% ± 1.77%	-0.56% ± 1.96%